

DTIC FILE COPY

2

GL-TR-90-0174

Super-Micro Computer Weather Prediction Model

Frank P. Colby, Jr. and Keith L. Seitter

University of Lowell
Department of Earth Sciences
One University Avenue
Lowell, MA 01854

DTIC
ELECTE
DEC 13 1990
S D CS D

June 1990

Scientific Report No. 2

Approved for public release; distribution unlimited

GEOPHYSICS LABORATORY
AIR FORCE SYSTEMS COMMAND
UNITED STATES AIR FORCE
HANSCOM AIR FORCE BASE, MASSACHUSETTS 01731-5000

AD-A230 063

This technical report has been reviewed and is approved for publication.

H. Stuart Muench

H. STUART MUENCH
Contract Manager

Donald A. Chisholm

DONALD A. CHISHOLM, Chief
Atmospheric Prediction Branch

FOR THE COMMANDER

Donald A. McClatchey for Rmm

ROBERT A. McCLATCHEY, Director
Atmospheric Sciences Division

This report has been reviewed by the ESD Public Affairs Office (PA) and is releasable to the National Technical Information Service (NTIS).

Qualified requestors may obtain additional copies from the Defense Technical Information Center. All others should apply to the National Technical Information Service.

If your address has changed, or if you wish to be removed from the mailing list, or if the addressee is no longer employed by your organization, please notify GL/IMA, Hanscom AFB, MA 01731. This will assist us in maintaining a current mailing list.

Do not return copies of this report unless contractual obligations or notices on a specific document require that it be returned.

Unclassified

SECURITY CLASSIFICATION OF THIS PAGE

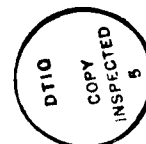
REPORT DOCUMENTATION PAGE

Form Approved
OMB No. 0704-0188

1a. REPORT SECURITY CLASSIFICATION Unclassified			1b. RESTRICTIVE MARKINGS		
2a. SECURITY CLASSIFICATION AUTHORITY			3. DISTRIBUTION / AVAILABILITY OF REPORT approved for public release; distribution unlimited		
2b. DECLASSIFICATION / DOWNGRADING SCHEDULE					
4. PERFORMING ORGANIZATION REPORT NUMBER(S)			5. MONITORING ORGANIZATION REPORT NUMBER(S) GL-TR-90-0174		
6a. NAME OF PERFORMING ORGANIZATION University of Lowell	6b. OFFICE SYMBOL (If applicable)	7a. NAME OF MONITORING ORGANIZATION Geophysics Laboratory			
6c. ADDRESS (City, State, and ZIP Code) Department of Earth Sciences One University Avenue Lowell, MA 01854		7b. ADDRESS (City, State, and ZIP Code) Hanscom AFB Massachusetts 01731-5000			
8a. NAME OF FUNDING / SPONSORING ORGANIZATION	8b. OFFICE SYMBOL (If applicable)	9. PROCUREMENT INSTRUMENT IDENTIFICATION NUMBER F1962-88-K-0016			
8c. ADDRESS (City, State, and ZIP Code)		10. SOURCE OF FUNDING NUMBERS			
		PROGRAM ELEMENT NO. 61101F	PROJECT NO. ILIR	TASK NO. 8K	WORK UNIT ACCESSION NO. AA
11. TITLE (Include Security Classification) Super-Micro Computer Weather Prediction Model					
12. PERSONAL AUTHOR(S) Frank P. Colby, Jr.; Keith L. Seitter					
13a. TYPE OF REPORT Scientific Report #2	13b. TIME COVERED FROM _____ TO _____	14. DATE OF REPORT (Year, Month, Day) 1990 June	15. PAGE COUNT 76		
16. SUPPLEMENTARY NOTATION					
17. COSATI CODES			18. SUBJECT TERMS (Continue on reverse if necessary and identify by block number)		
FIELD	GROUP	SUB-GROUP	Mesoscale Modeling Weather Forecasting		
			Computer Simulation Models		
			Boundary Layer Parameterizations		
19. ABSTRACT (Continue on reverse if necessary and identify by block number) A meso-beta scale model is being developed to provide forecast guidance in the 3 to 18 h time period. The model is intended for use at local base weather offices equipped with a super-micro class computer, allowing these offices to produce local forecast guidance for their region. The model consists of five layers, the lowest of which represents the evolving boundary layer. A specially developed vertical coordinate is used that allows the model to dynamically adjust to changes in boundary-layer height so that the thickness of the lowest layer increases and decreases as the boundary layer grows and shrinks. This allows a fairly simple boundary-layer parameterization to be used that realistically simulates boundary-layer processes. This report presents the model equations for the dynamic model, including their derivation and energy conserving finite difference representation. The physical parameterizations were presented in an earlier report, so only changes compared to that previous presentation are included here. This report also presents the results from a variety of test simulations of the model and physical parameterizations.					
20. DISTRIBUTION / AVAILABILITY OF ABSTRACT <input type="checkbox"/> UNCLASSIFIED/UNLIMITED <input type="checkbox"/> SAME AS RPT. <input type="checkbox"/> DTIC USERS			21. ABSTRACT SECURITY CLASSIFICATION Unclassified		
22a. NAME OF RESPONSIBLE INDIVIDUAL H. Stuart Muench			22b. TELEPHONE (Include Area Code)	22c. OFFICE SYMBOL GL/LYP	

Table of Contents

1. Introduction	1
2. Model Description	
a. Basic model equations	2
b. Grid domain and horizontal nesting	5
c. Time integration and outer lateral boundary condition	8
d. Coupling of the model with the boundary-layer parameterization	8
e. Boundary layer treatment of grid boxes with both land and water	10
f. Boundary layer transitions	12
3. Simulations with the ETA5 Model	
a. Mountain lee-wave experiments with a constant boundary-layer height	14
b. Experiments with a changing boundary-layer height	28
c. Eddy diffusion sensitivity tests	36
4. Domain for Prototype testing	39
5. Comparison of the Boundary-Layer Parameterizations With the O'Neill Dataset	49
6. Conclusions and Future Work	54
Appendix: Derivation and Energy Conservation of the Eta-Coordinate System	
a. Derivation of the equations in η -coordinates	56
b. Energy conservation in the η -system	58
c. The energy conserving finite difference equations	61
d. The complete finite difference equation set	67
References	70



Accession For	
NTIS CR181	✓
DTIC TAB	
Unannounced	
Justification	
By	
Distribution/	
Availability Codes	
Dist	Availability for Special
A-1	

1. Introduction

As discussed in Scientific Report #1 (Seitter and Colby 1989; hereafter SC), the goal of this research project is to create a meso- β scale prediction model which is capable of being run operationally on a relatively small computer. The approach being taken is centered on recasting the equations in a new form which allows the critical aspects of the atmospheric boundary layer to be included without a large number of vertical layers in the model. This allows significantly fewer grid points in the three-dimensional domain which leads to increased computational speed. This aspect, along with other consistent approximations in the equations and parameterizations provides a means of producing a model which is many times faster than other mesoscale models currently in use today [see Appendix B of Pielke (1984) for information on the computational aspects of many current mesoscale numerical models]. A high resolution model can only be implemented on a regional domain given the current limitations of computers. The influence of changes in the larger scale weather patterns are included by nesting the high resolution model in a model with coarser horizontal resolution (but the same vertical structure). This coarse grid model, in turn, can receive boundary information from the operational models of the National Weather Service.

The basic model formulation, as originally conceived and discussed extensively in SC, consisted of a two-layer "boundary layer coordinate" model which was formally nested in the lowest layer of a four-layer σ -coordinate model. While the initial testing reported in SC showed promising results, additional and more critical tests indicated the vertical nesting procedure could lead to accumulating errors that eventually destroyed the solution. Further work showed that the nesting procedure failed to conserve energy in the finite difference equations, and this lack of energy conservation appeared to contribute to some aspects of poor model performance. The model structure described in SC was therefore abandoned in favor of that described in this report. While direct comparisons with the previous model formulation will not be discussed here, it should be noted that the current model formulation has outperformed the previous formulation in *every* aspect of testing and is only slightly more costly in terms of computation time.

The current model formulation will be discussed in section 2, along with changes and additions to the boundary-layer parameterizations discussed in depth in SC. Section 3 will present the results of model simulations testing the new formulation under a variety of circumstances, and some sensitivity studies involving the specification of the horizontal diffusion. Some aspects of the prototype operational formulation for the model are discussed in section 4. Comparisons of test simulations of the boundary layer parameterization, including radiation calculations, with other boundary layer work will be presented in section 5, and the report concludes with section 6.

2. Model Description

a. Basic model equations

Most mesoscale models rely on a large number of layers near the surface in order to resolve explicitly the growth and decay of the planetary boundary layer and to correctly simulate the fluxes of heat and moisture that couple the atmosphere to the surface. This leads to models with a large number of layers in the vertical, resulting in large numbers of computations per timestep and relatively long computation times even in supercomputer environments (Pielke 1984; Appendix B). On the other hand, some early models showed success in simulating nonboundary-layer-driven flows (such as mountain lee-waves) with relatively few layers (Anthes and Warner 1978), and other models looking specifically at boundary layer processes were able to successfully capture the important features by treating the boundary layer as a single layer which could dynamically grow and collapse (Lavoie 1972; Colby 1983).

The present formulation seeks to marry these two approaches into a single three-dimensional mesoscale model. The lowest layer of the model is the boundary layer — it is allowed to grow in depth or collapse at each grid point as the simulation proceeds in response to the surface fluxes produced in the boundary-layer and radiation parameterizations. The layers above the boundary layer adjust dynamically to the changing boundary-layer depth, while simulating the horizontal and vertical advections of momentum and thermodynamic variables and maintaining the proper balances that hold at the meso- β scale.

The vertical coordinate which allows for this changing boundary-layer depth is a modification of the common σ -coordinate [$\sigma = (p - p_t) / (p_s - p_t)$ where p_s is the surface pressure and p_t is a pressure level specified as the top of the model (we take $p_t = 100$ mb for this study)]. If we let σ_h represent the height of the top of the boundary layer (see Fig.1), we can define a new vertical coordinate, η , as

$$\eta = \frac{\sigma - \sigma_h}{H} \quad H = \begin{cases} \sigma_h & \sigma < \sigma_h \\ 1 - \sigma_h & \sigma > \sigma_h \end{cases} \quad (2.1)$$

We refer to η as "boundary layer coordinates." The vector momentum equation, hydrostatic relation, continuity equation, thermodynamic equation, and specific

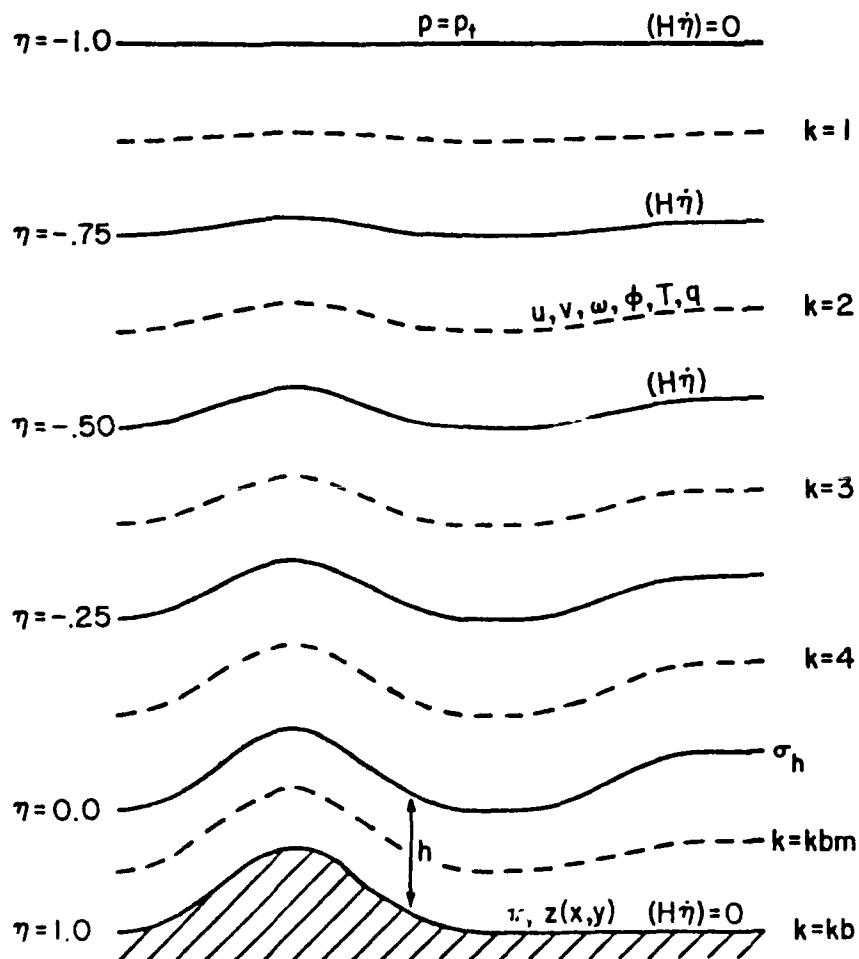


Fig. 1. Schematic structure of the five-layer η -coordinate model.

humidity conservation equation can be written in the η system as

$$\begin{aligned} \frac{\partial \pi H V}{\partial t} + \frac{\partial u \pi H V}{\partial x} + \frac{\partial v \pi H V}{\partial y} + \frac{\partial \pi V H \dot{\eta}}{\partial \eta} = \\ - \pi H \nabla \phi - \pi H \alpha \nabla \sigma \pi - f \mathbf{k} \times \pi H V + \pi H F_{uv} \end{aligned} \quad (2.2)$$

$$\frac{\partial \phi}{\partial \eta} = -\pi H \alpha \quad (2.3)$$

$$\frac{\partial \pi H}{\partial t} + \nabla \cdot \pi H V + \pi \frac{\partial H \dot{\eta}}{\partial \eta} = 0 \quad (2.4)$$

$$\frac{\partial \pi H T}{\partial t} + \frac{\partial u \pi H T}{\partial x} + \frac{\partial v \pi H T}{\partial y} + \frac{\partial \pi T H \dot{\eta}}{\partial \eta} = \frac{\pi H \alpha \omega}{c_p} + \frac{\pi H Q}{c_p} + \pi H F_T \quad (2.5)$$

$$\frac{\partial \pi H q}{\partial t} + \frac{\partial u \pi H q}{\partial x} + \frac{\partial v \pi H q}{\partial y} + \frac{\partial \pi q H \dot{\eta}}{\partial \eta} = \pi H F_q \quad (2.6)$$

where $\pi = p_s - p_t$, q is the specific humidity, and the other terms have their normal meteorological definitions (see the Appendix for information on the derivation of these equations and a list of terms). It should be noted that the σ which appears on the right-hand side of (2.2) is a dependent variable which will not be constant on a constant η surface, in general. Expansion of this gradient of a product results in an additional pressure-gradient-force type term not present in traditional σ -coordinate models. It should also be noted that the humidity is treated here as a passive scalar, so (2.6) simply represents conservation of q (that is, $dq/dt = 0$, except for the eddy diffusion term added to the rhs) in the η system. When condensation and evaporation are included, appropriate source and sink terms will need to be added to (2.6) and another conservation equation governing the condensate will be required.

Equation (2.4) is not used directly in the model, but it does provide the means of calculating vertical velocities and the rate of change of surface pressure. Integration of (2.4) from the model top to the surface yields

$$\begin{aligned} \frac{\partial \pi}{\partial t} = - \int_{-1}^0 \left[\frac{\partial}{\partial x} (H_1 \pi u) + \frac{\partial}{\partial y} (H_1 \pi v) \right] d\eta \\ - \int_0^1 \left[\frac{\partial}{\partial x} (H_2 \pi u) + \frac{\partial}{\partial y} (H_2 \pi v) \right] d\eta \end{aligned} \quad (2.7)$$

where H_1 and H_2 represent the values of H above and below the boundary layer top, respectively, as given by (2.1). Integration of (2.4) from the top of the model down to a specific interface level, along with the use of $\partial\pi/\partial t$ found with (2.7) allows the determination of $(H\dot{\eta})$ at each interface as

$$(H\dot{\eta}) = -(\eta+1) \left[\pi \frac{\partial \sigma_h}{\partial t} + \frac{H_1}{\pi} \frac{\partial \pi}{\partial t} \right] - \int_{-1}^{\eta} \left[\frac{\partial}{\partial x} (H_1 \pi u) + \frac{\partial}{\partial y} (H_1 \pi v) \right] d\eta \quad (2.8)$$

The Appendix verifies that the continuous equations transformed into η -coordinates satisfy the classical energy conservation constraints of the atmosphere. It is desirable to have the finite difference forms of the equations satisfy these energy conservation constraints as well, and the Appendix outlines how the vertical differencing must be carried out to preserve these properties. It also shows how the energy constraints lead to specific forms for the solution of the thermodynamic equation, (2.5), and the integration of the hydrostatic equation, (2.3), to find the geopotentials of midlevels of the η -layers. The resulting finite difference forms are considerably different in structure from equations (2.2)–(2.6), and also different from the forms introduced in SC.

The last terms on the rhs of (2.2), (2.5), and (2.6) include a “friction” term, F , which, above the boundary layer, is given by a horizontal eddy diffusion. This term is modeled by a simple Fickian diffusion, $K\nabla^2\phi$, where K is a constant eddy viscosity and ϕ is the variable of interest (u , v , T , or q). In most simulations, we let $K = 2 \times 10^5 \text{ m}^2 \text{ s}^{-1}$ for the momentum components and $K = 0$ for temperature and moisture (see section 3 for a more complete discussion of diffusion in the model and the results of some sensitivity tests).

b. Grid domain and horizontal nesting

A staggered grid is used in both the vertical and horizontal directions. In the vertical, all variables are layer quantities except vertical velocities, which are defined at interface levels (see Fig. 1). Horizontally, velocities are defined on staggered points which surround the points on which all other variables are defined.

In order to increase the overall model domain size and move the lateral boundaries away from the area of primary interest, a horizontal nesting of the model is employed as developed by Zhang et al. (1986). A fine grid mesh (FGM) with 20 km resolution is nested in a coarse grid mesh (CGM) with 60 km resolution. A 3:1 ratio of FGM points to CGM points is necessary with a staggered grid so that both "velocity" and "thermodynamic" points can be coincident in the overlap region (Zhang et al. 1986). The CGM domain covers 1320 km x 1320 km while the FGM domain is 480 km x 480 km for "thermodynamic" points (all displays will be made on "thermodynamic" point arrays, with any displayed velocities being averaged to these points). As described in somewhat more detail in SC, the two-way interactive nesting procedure of Zhang et al. (1986) is used with a few minor modifications. In the calculation of tendencies for the "thermodynamic" points in the FGM, for example, a simple linear interpolation is used between CGM points nearest the boundary FGM point rather than the "Lagrangian interpolation" used by Zhang et al. (1986).

Zhang et al. (1986) discuss a Newtonian damping scheme which is applied near the FGM/CGM interface to help control noise resulting from the overspecification of the pressure tendencies there. As will be shown in later sections, we discovered similar noise generation, especially on outflow boundaries where the overspecification is most severe. We therefore plan to include an additional smoothing mechanism near the boundaries, but not in the form described by Zhang et al. (1986). Zhang et al. (1986) describe their Newtonian damping scheme as being given by (for a σ -coordinate model)

$$\frac{\partial \pi V}{\partial t} = \dots -(\pi V - \overline{\pi V})/\tau_d(\sigma) \quad (2.9)$$

where the π -weighted velocities on the rhs are meant to be taken at the "latest time level," and the overbar represents a two-point average using values on either side of the point of interest (which is located one grid interval in from the FGM boundary). The quantity $\tau_d(\sigma)$ is a relaxation constant which is specified as a function of height [varying between $20\Delta t$ and $100\Delta t$ for Zhang et al. (1986)]. We will look at this noise control technique in some more detail.

Suppose we consider applying this Newtonian damper to a u -momentum variable U (where U might be $\pi H u$ in η -coordinates or πu in σ -coordinates) which is governed by an equation of the form

$$\frac{\partial U}{\partial t} = F \quad (2.10)$$

Then, without damping, a value of U at timestep $n+1$ at gridpoint (i,j) would be given by (using the leapfrog scheme)

$$U_{ij}^{n+1} = U_{ij}^{n-1} + 2\Delta t F_{ij}^n \quad (2.11)$$

If the damping scheme is applied to this point as implied by Zhang et al. (1986) and Kurihara and Bender (1980), we obtain (assuming an east or west boundary)

$$U_{ij}^{n+1} = U_{ij}^{n-1} + 2\Delta t F_{ij}^n - \frac{2\Delta t}{\tau_d} \left[U_{ij}^{n+1} - \frac{1}{2}(U_{i+1j}^{n+1} + U_{i-1j}^{n+1}) \right] \quad (2.12)$$

This equation is semi-implicit, but can be applied explicitly as long as it is not also applied at points $(i+1,j)$ or $(i-1,j)$, because new values of U_{i+1j}^{n+1} and U_{i-1j}^{n+1} can be found first, allowing (2.12) to be solved for U_{ij}^{n+1} .

If, instead, we use (2.11) to produce an "undamped" estimate of U_{ij}^{n+1} , denoted \hat{U}_{ij}^{n+1} , we can rewrite (2.12) as

$$U_{ij}^{n+1} = \hat{U}_{ij}^{n+1} - \frac{2\Delta t}{\tau_d} \left[\hat{U}_{ij}^{n+1} - \frac{1}{2}(U_{i+1j}^{n+1} + U_{i-1j}^{n+1}) \right] \quad (2.13)$$

It is easy to see that (2.13) represents a simple numerical filter applied at time level $n+1$ (Shapiro 1970), with the quantity $(2\Delta t/\tau_d)$ serving as the nondimensional filter factor. Since the same effect can be obtained through the use a Fickian diffusion term (Kurihara and Bender 1980), we have chosen to abandon the Newtonian damping term in favor of an increased diffusion coefficient, K , on those grid points near the boundary.

c. Time integration and outer lateral boundary condition

Time integration for the model is performed using the leapfrog scheme with an Asselin filter. The time step for FGM points is 20 s and for CGM points is 60 s. The flow relaxation condition of Davies (1976) is used on lateral boundaries following the work of Seitter (1987) who found that this condition was well-behaved, provided a simple means of allowing external information to be introduced into the model, and did not require the smoothing operator necessary in the Perkey and Kreitzberg (1976) sponge. The flow relaxation condition requires a 5 gridpoint wide region near the boundary for application, and solutions in this "relaxation region" should be considered modified. The flow relaxation condition is only applied at the lateral boundaries of the CGM domain, however, so FGM points are not significantly influenced by the relaxation region.

d. Coupling of the model with the boundary-layer parametrization

The basic equations which make up the boundary-layer parameterization are described in detail in SC and will not be reproduced here. The boundary-layer package provides the model with the fluxes of heat, moisture, and momentum from the surface, and calculates the rate of change of boundary-layer height which is fundamental to the η -coordinate formulation. A summary of these quantities is shown in Table 1.

It is important to note that the boundary-layer routine diagnoses the current boundary layer depth (hydrostatically) from the current σ_h when it is called, and returns a time rate of change of boundary-layer height, $\partial h / \partial t$, where h is in geometric height above the ground. The model requires both the rate of change of boundary-layer height and the new boundary-layer in terms of σ , so a conversion must be made. The hydrostatic relation may be written in σ -coordinates as

$$\frac{\partial \phi}{\partial \sigma} = -\pi \alpha \quad (2.14)$$

which can be integrated from the surface ($\sigma=1$) to the top of the boundary layer ($\sigma=\sigma_h$) to obtain

Table 1. Quantities provided to the model by the boundary-layer parameterization.

Variable returned	Description
$\frac{dh}{dt}$	Rate of change in height of boundary layer top
$\frac{dT_G}{dt}$	Rate of change of ground temperature
$\frac{dGW}{dt}$	Rate of change of ground wetness
T_{kb}	Diagnosed "surface" temperature
q_{kb}	Diagnosed "surface" mixing ratio
SH	Sensible heat flux
LH	Latent heat flux
GS	Surface soil heat flux
NR	Net radiation (incoming shortwave minus outgoing IR)
τ	Surface stress (friction)

$$\phi_h = -\pi \int_1^{\sigma_h} \alpha d\sigma \quad (2.15)$$

With the excellent approximation that $\phi = gh$, and making use of the mean value theorem, we can obtain

$$h = \frac{\pi \bar{\alpha}}{g} (1 - \sigma_h) \quad (2.16)$$

Taking the partial derivative with respect to time of this expression and rearranging yields

$$\frac{\partial \sigma_h}{\partial t} = -\frac{g}{\pi \bar{\alpha}} \frac{\partial h}{\partial t} + \frac{(1 - \sigma_h) \partial \pi}{\pi \partial t} + \frac{(1 - \sigma_h) \partial \bar{\alpha}}{\bar{\alpha} \partial t} \quad (2.17)$$

Equation (2.17) provides a means of computing the rate of change of σ_h from $\partial h / \partial t$ as long as we can estimate all the other terms on the rhs. Experimentation has shown that the last term is always at least two orders of magnitude smaller than

the first two terms on the rhs, so that term is dropped. The remaining information is readily available from the model since the boundary-layer temperature can be used to find $\bar{\alpha}$ and $\partial\pi/\partial t$ can be computed using (2.7). The tendency produced by (2.17) is used on the current timestep where required [for example in (2.8)], and it is also used to calculate the new value of σ_n in a leapfrog timestepping scheme (with Asselin filter) identical to that used for the other prognostic variables.

e. Boundary-layer treatment of grid boxes with both land and water

The presence of both land and water in a grid element requires special consideration in the boundary-layer parameterization. If grid boxes were treated as either all water or all land, the parameterization could be coded with a simple branch to handle each condition. We choose to allow fractional land-water coverage in grid boxes to more accurately represent the actual land form (see section 4).

We assume that the temperature of the water does not change with time during the integration of the model. Since the model is designed to run for only 24 hours after initialization, this assumption is reasonable. The temperature of the ground changes quite rapidly during a given integration, and this temperature is stored in the variable TG. We define an "effective ground temperature" (ETG) for each grid box for use in flux calculations. For "all land" grid boxes, the effective ground temperature is simply TG. For "all water" grid boxes, ETG is the water temperature, TWATER. For partial land boxes, the effective ground temperature for use in the rest of the parameterization is taken to be a weighted average of TG and TWATER based on the percent land coverage in the grid box. The quantity TG is allowed to change as usual, since land surfaces would be expected to heat normally despite the presence of water in the same grid box.

Both latent and sensible heat fluxes are affected directly by the presence of a water surface. The sensible heat flux is driven by a temperature difference between the ground or water surface and the air just above. If this difference is minimized by the presence of constant-temperature water, the sensible heat flux will be reduced. The presence of the water surface also ensures an endless supply of moisture which can be evaporated. Thus, the latent heat flux over a partial-land grid box will tend to stay higher, and this will prevent the land from heating up as fast as it otherwise would. In a clear-sky, daytime situation, the net effect of

having a grid box partially or wholly covered by water is to reduce the growth of the convective boundary layer and slow the heating of the effective ground surface. Figure 2 shows the height of the convective boundary layer for a range of land/water mixes. The solid curve represents the results for an all-land grid box in which the boundary layer grows rapidly after sunrise. Moderate water coverage in the grid box results in a significant reduction of the boundary-layer growth, and for the 0% land surface case, the boundary layer grows only slightly. For the

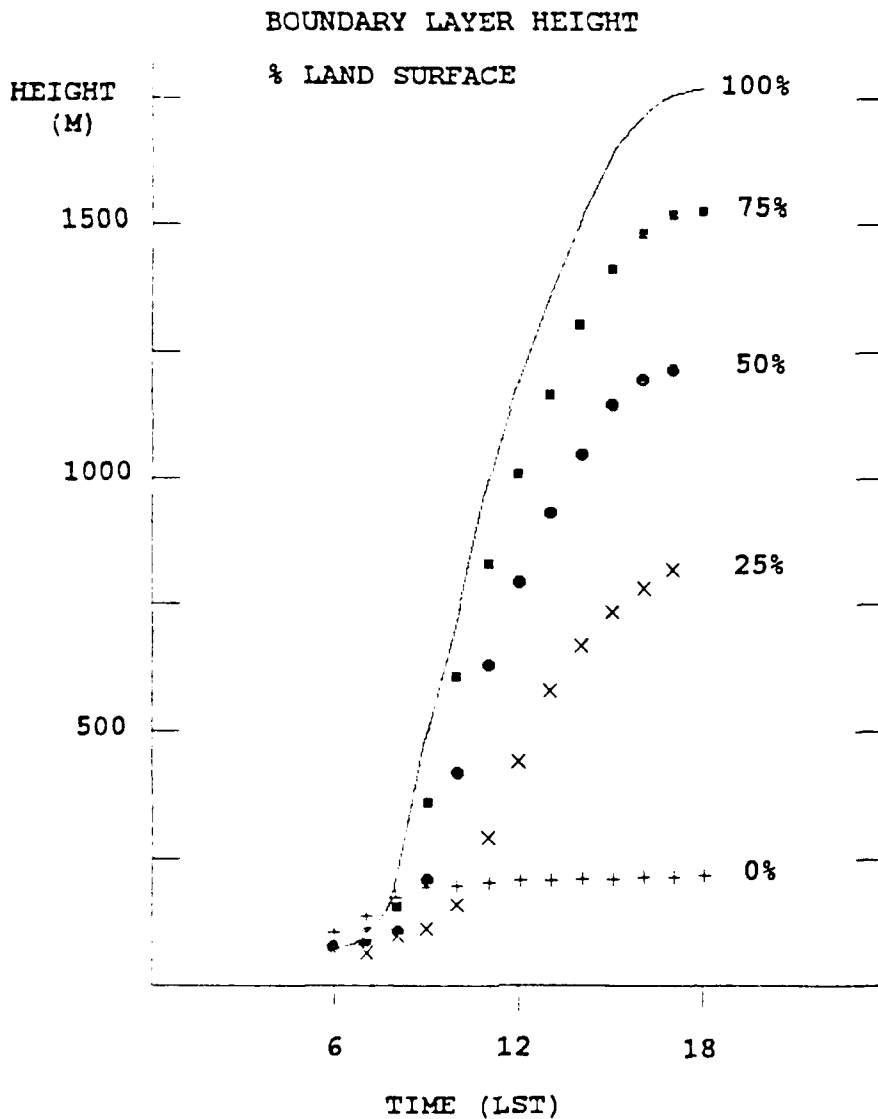


Fig. 2. Boundary layer height as a function of time for different percentages of land and water within a grid box.

partial land cases, the convective boundary layer actually collapses into a stable one between 1700 and 1800 local time (LST), which is why no data is shown at 18 LST for these runs.

f. Boundary layer transitions

Transitions between stable and unstable boundary layer regimes have been incorporated into the boundary-layer parameterization. In the real atmosphere, these transitions are almost certainly abrupt and characterized by poorly defined structures. Within the model, such a situation would lead to numerical problems. In addition, there is no known parameterization for a boundary layer in transition, so we have to provide a mechanism for an orderly transition.

The transition stage is determined by the sign of the sensible heat flux. When the direction of the sensible heat flux is incompatible with the nature of the boundary layer, the transition stage is set. The boundary layer height is constrained to fall from its current location to a height of 90 m (arbitrarily chosen) in 15 min. During this transition, the potential temperature structure in the boundary layer is changed as little as possible, thereby allowing the proper parameterization to begin with the current structure as though the transition had been instantaneous. The potential temperature at the top of the boundary layer is linearly interpolated between its current value and the potential temperature of the ground. Boundary layer moisture is conserved during this process of boundary layer height fall, again to preserve current conditions as much as possible. When the boundary layer height reaches 90 m the transition ends. The boundary layer then begins to grow again according to the stability at that time.

Transitions from unstable to stable and vice versa have been tested and found to be relatively smooth and reliable. Although most of these transitions will take place at dawn or dusk, it is conceivable that a major change in cloud cover or air mass might initiate such a change at any time during an integration. The only aspect of this which will not be handled well by the parameterization is a situation in which a well-mixed convective boundary layer grows to a substantial depth, then the radiation is interrupted by clouds, causing a transition to a stable boundary layer, followed by a breakup of the clouds and a return to unstable stratification. The new convective boundary layer will start over and the atmosphere above the

boundary layer, which in the real atmosphere would be almost dry adiabatic in structure, will be slightly stable in the model. This is, of course, a problem with the limited vertical resolution of the model, not the fault of the parameterization. Only extensive testing will be able to show if this is a serious problem. We suspect that most cloud cover will only reduce the sensible heat flux in magnitude rather than actually reversing the sign. Hence, the boundary layer will grow much more slowly but will not go through a transition.

An example of the results after two transitions is shown in Fig. 3. The ground temperature for a run using a one-dimensional version of the boundary layer parameterizations is shown after 30 hours. Clearly, the transitions are smooth for this variable. The boundary layer becomes stable near 1800 LST, remains stable until 0800 LST on the second day, and is unstable until the end of the simulation on

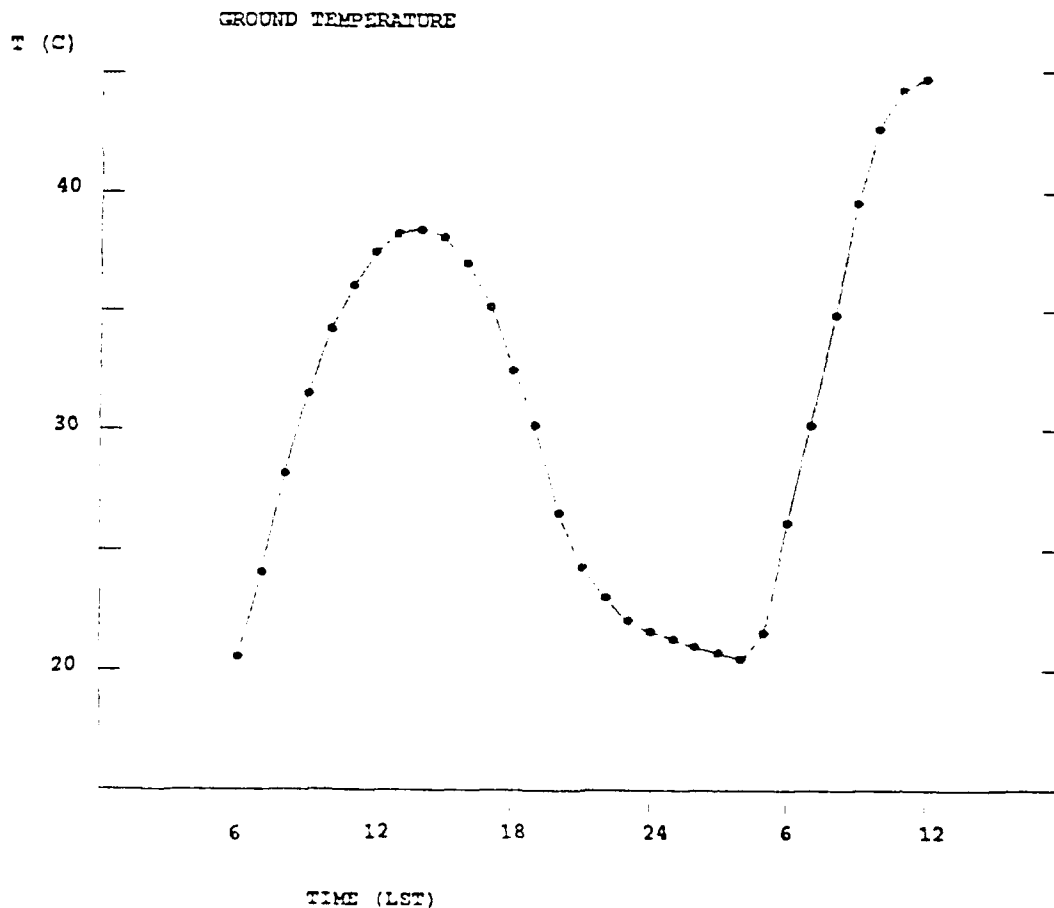


Fig. 3. Ground temperature for a 30 h simulation using the one-dimensional version of the boundary-layer parameterizations.

the second day (1200 LST). Dawn occurs just before 0500 LST, and the ground immediately begins to heat up at this point. The boundary layer remains stable until the ground heating is sufficient to bring the ground temperature above the surface air temperature. This happens around 0800 LST on the second day. One difference between the two morning patterns is that the ground temperature reaches a much higher value on the second day. This occurs because the ground surface dries out during the first day, allowing the available incoming energy on the second day to be used much more for heating the ground and less for evaporating soil moisture.

3. Simulations with the ETA5 Model

The five-layer η -coordinate model described above is referred to as the ETA5 model. This section will present a series of test simulations designed to examine the capabilities of the model formulation and verify the correctness of the coding. For all the simulations presented here, ETA5 is being run without the boundary layer parameterization package and with no moisture. This allows the hydrodynamic portion of the model to be tested without the complexities introduced by the physical parameterizations. The thermodynamic structure taken for all simulations shown here is the U.S. Standard Atmosphere profile.

For all simulations discussed in sections 3a and 3b, only the momentum equations contain an eddy diffusion term with the coefficient $K = 2 \times 10^5 \text{ m}^2\text{s}^{-1}$, while $K = 0$ for all thermodynamic variables. Further, no additional diffusion was set near the CGM and FGM interface region. Additional smoothing techniques are discussed in section 3c. The ability of the model to correctly allow a variable height boundary layer is tested in section 3b by forcing the boundary layer height change explicitly.

a. Mountain lee-wave experiments with a constant boundary-layer height

The simulation of mountain lee-waves is generally considered an important test of a mesoscale model (Anthes and Warner 1978; Nickerson et al. 1986). SC showed that the major features of lee-waves could be simulated even with the

coarse vertical resolution used in the present model. This section will present the results of several simulations to confirm this and to demonstrate the structure taken on in the ETA5 model for boundary layers of different depths. Following SC, we will conduct these tests with the full three-dimensional model rather than a two-dimensional analog. In all the simulations shown, a 1 km ridge with a Gaussian cross section is aligned north-south in the FGM domain. The ridge terminates smoothly within the FGM domain and does not extend into the CGM domain (see FGM horizontal plots showing height contours below). For all simulations shown, a 20 m s^{-1} u -component wind is initially specified at all levels and held constant on the outer CGM lateral boundaries. It should be noted that, although not presented below, simulations with a negative u velocity and simulations with the mountain oriented east-west have been carried out to isolate potential coding errors.

Figure 4 shows a vertical cross section through the center of the FGM domain for a lee-wave simulation in which the Coriolis parameter was set to zero. Figure 4a shows the potential temperature field at 12 h simulated time, while Fig. 4b shows the u -component velocities. The dots plotted in the figures show the locations of thermodynamic grid points on η surfaces in the model. In Fig. 4a, a thin dashed line shows the top of the boundary layer (that is, the σ_h surface). The isopleths in Fig. 4b are subjectively analyzed because of the limited number of layers.

The structure shown in Fig. 4 matches the qualitative structure of a mountain lee-wave, with the wave structure sloping into the wind with height and a reversal of the velocity perturbation directly above the mountain aloft compared to the layer near the surface. The boundary layer height for this simulation was set by specifying $\sigma_h = 0.90$. This results in a boundary layer that is approximately 91 mb (about 790 m) deep. The η -coordinate formulation then spaces the remaining four layers above the boundary layer evenly in σ . Figure 5 shows a horizontal plot for this same simulation and time showing the sea-level pressure (reduced using a constant lapse rate hydrostatic formula) and boundary layer winds. The weak upstream damming and lee trough are evident in the pressure contours representing values above and below the initially specified sea-level pressure of 1013.25 mb. The deflection of boundary layer flow around the mountain is also evident in the wind field. The time required by the model to reach a steady flow can be assessed by plotting the average of the absolute value of the rate of change of π ($|\partial\pi/\partial t|$)

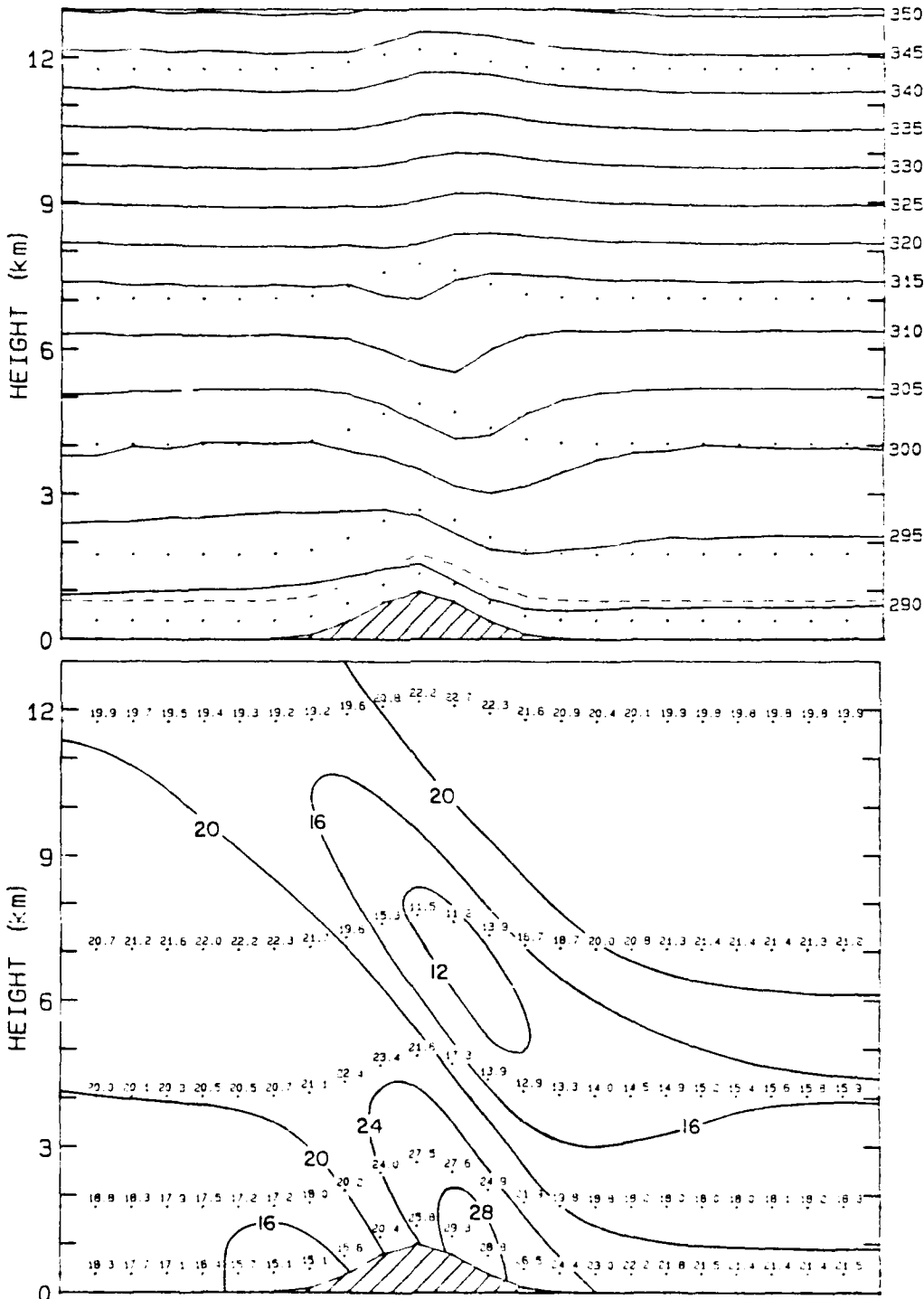


Fig. 4. Vertical cross section through the FGM domain at 12 h simulated time for lee wave test with no Coriolis effect showing (a) the potential temperature, and (b) the u -component velocity. Isentropes are labeled in K along the right in (a) and grid point values of the velocity are plotted in (b) in m s^{-1} . The top of the boundary layer is shown in (a) by a thin dashed line ($\sigma_h = 0.90$).

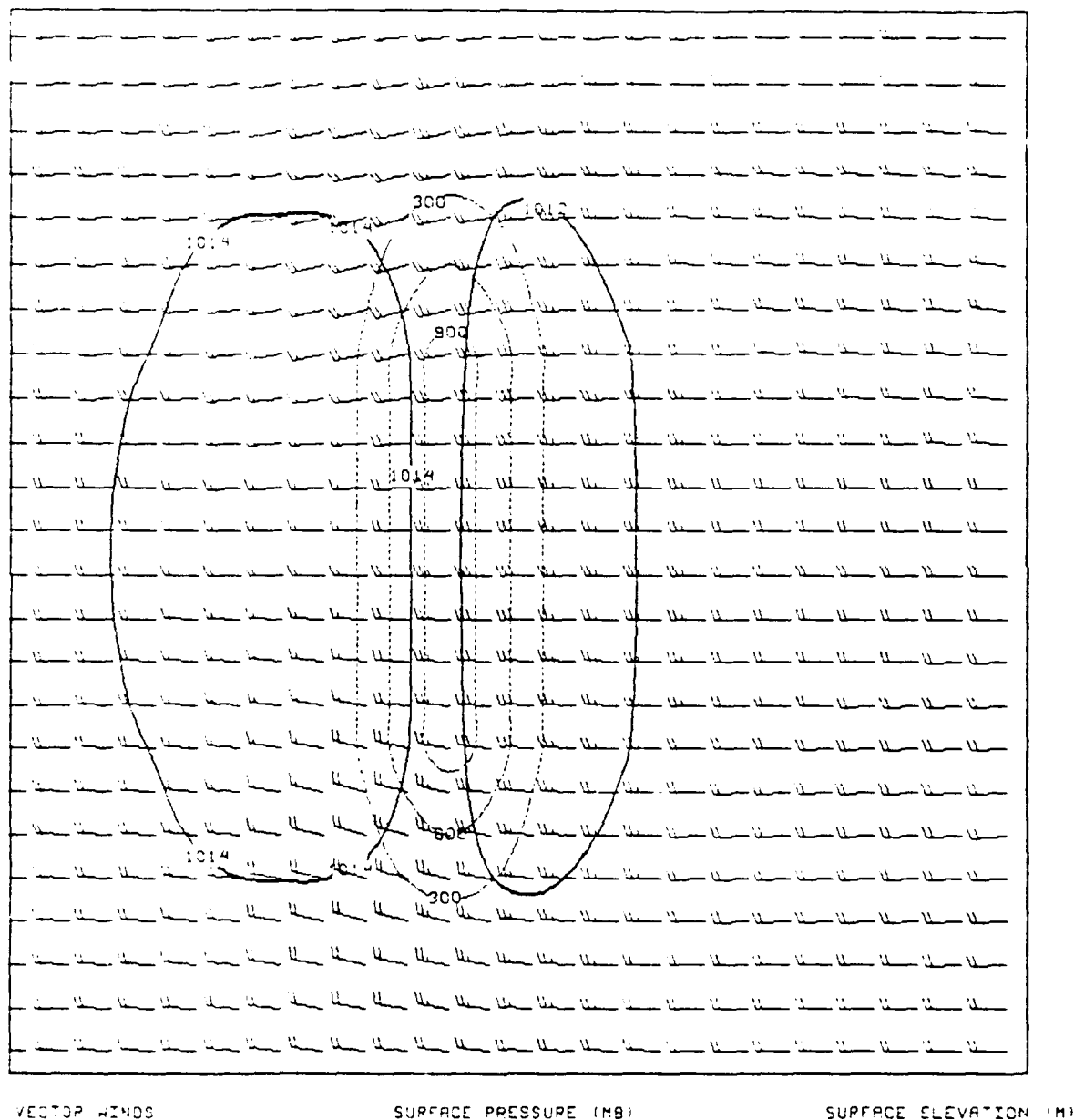


Fig. 5. Horizontal plot for simulation shown in Fig. 4. Solid contours give sea-level pressure (in mb), thin dashed contours are for surface topography (in m) of the mountain ridge, and boundary layer winds (one full barb represents 10 m s^{-1}) are plotted at each grid point.

in the FGM domain for the simulation. This is shown in Fig. 6. After a period of oscillations of rapidly decreasing amplitude for the first few hours, the model simulation becomes quite steady. Despite the steadiness of the solution, some small amplitude $2\Delta x$ noise develops in the temperature field during the last 6 h of the simulation. This is noticable in Fig. 4a near the western boundary (the left side of the plot). It is not surprising that some noise would develop given the complete lack of smoothing of temperatures in the model. In fact, it is more surprising that the model could be integrated for 12 h with a fairly large amplitude disturbance and generate so little noise.

We carried out an experiment similar to that described above except with the Coriolis effect included by setting $f = 10^{-4} \text{ s}^{-1}$ and specifying an initial pressure gradient in balance with a 20 m s^{-1} wind. Figures showing the same fields as

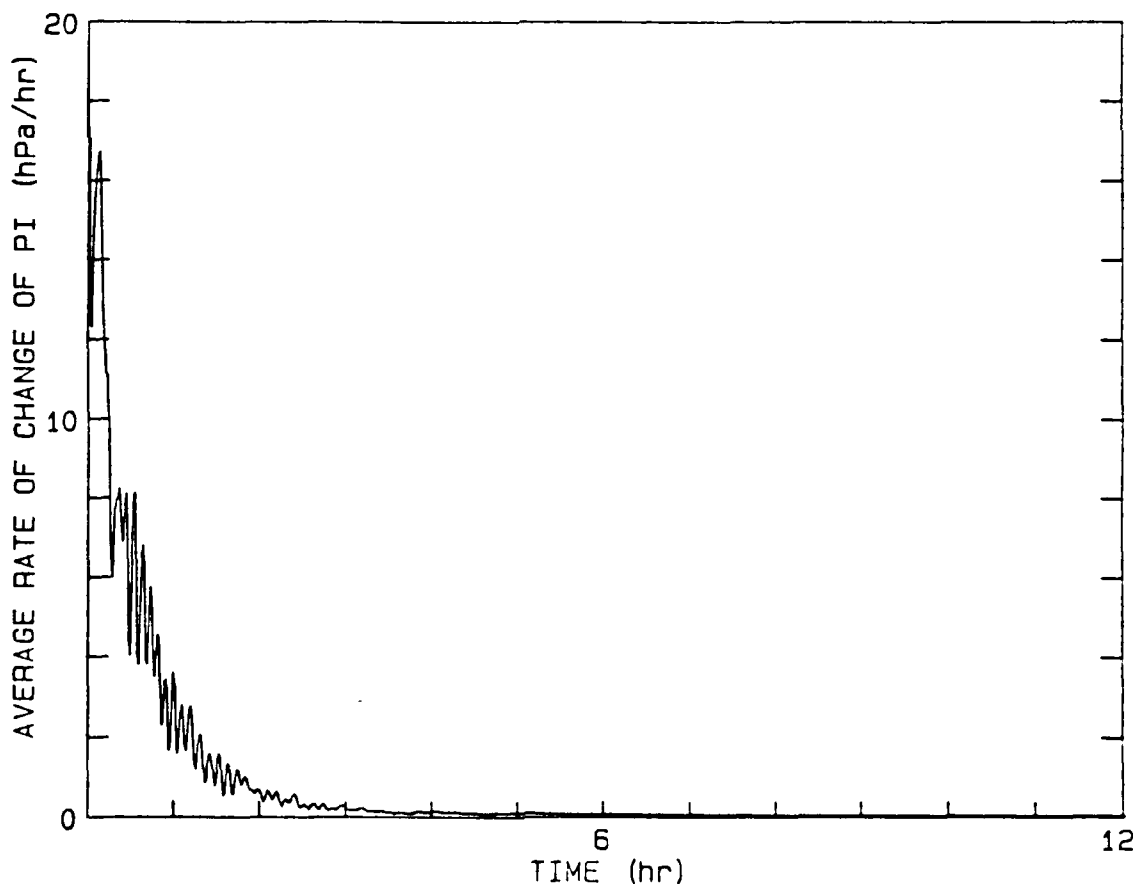


Fig. 6. Average rate of change of π versus time for FGM domain during the simulation shown in Figs. 4 and 5.

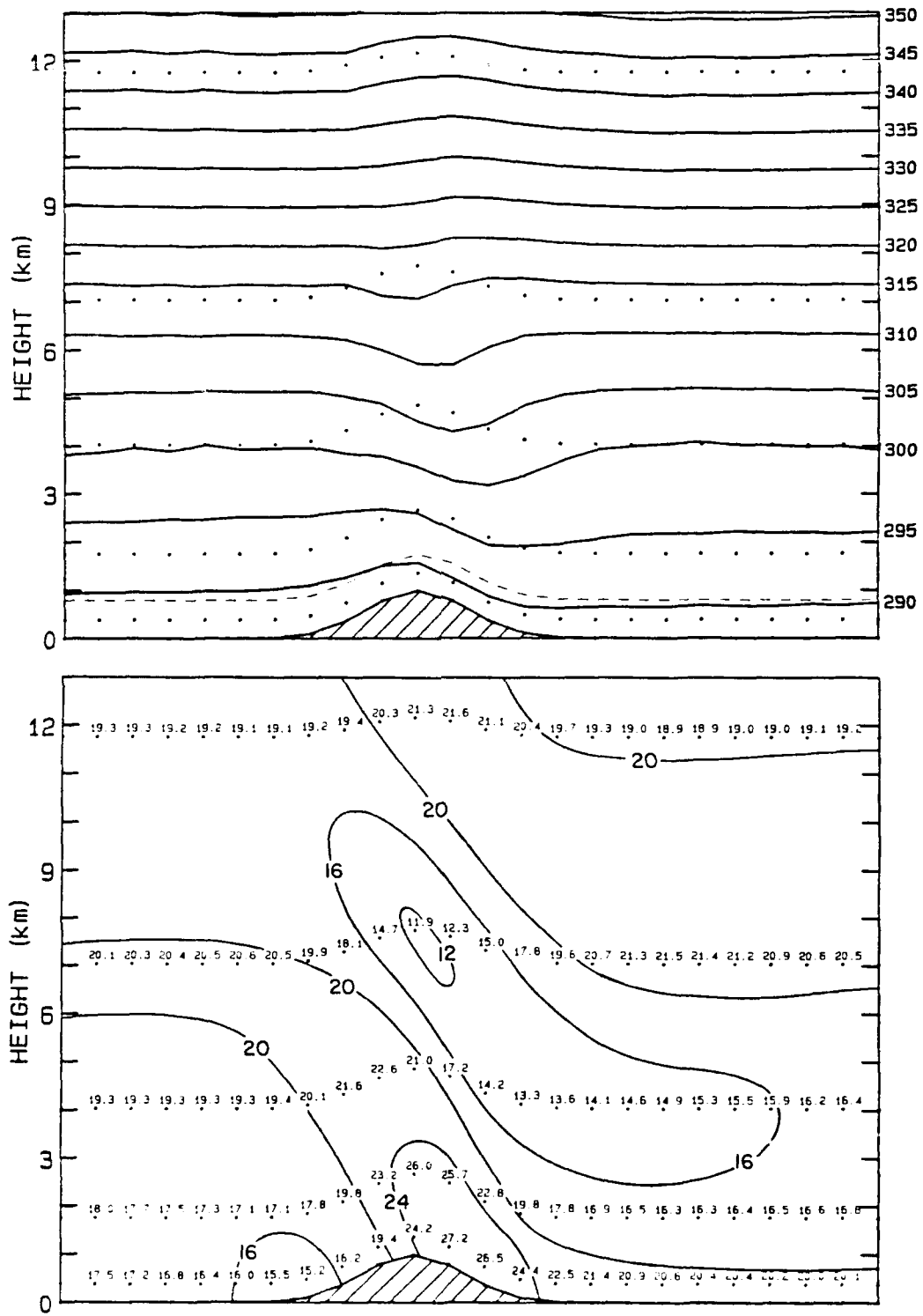


Fig. 7. As in Fig. 4, except that the Coriolis effect was included.

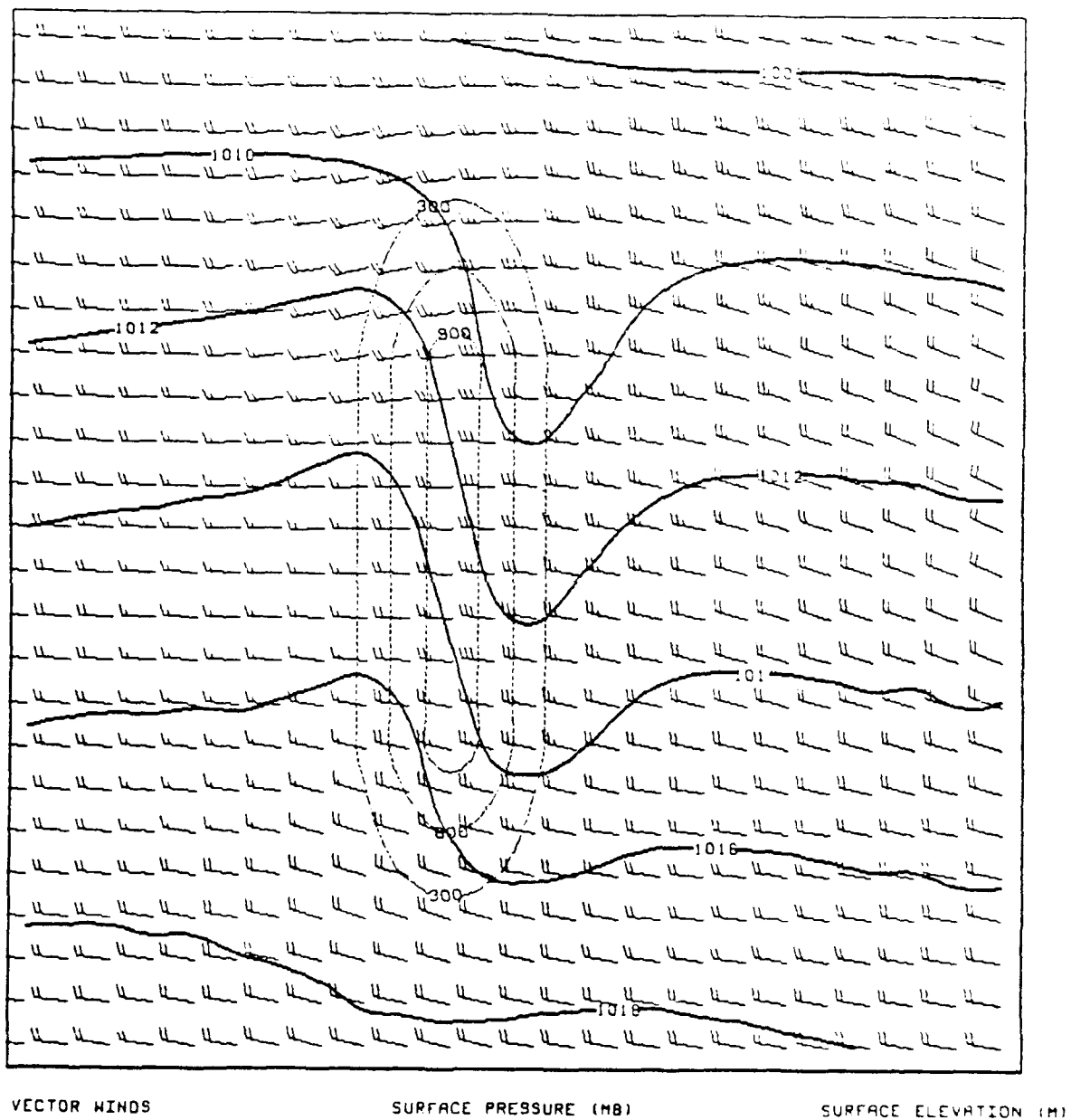


Fig. 8. As in Fig. 5, except that the Coriolis effect was included.

Figs. 4–6 are shown in Figs. 7–9. The cross section plots, Figs. 7a and 7b, are nearly identical to those produced with no Coriolis effect, except that the wave has a slightly smaller amplitude. The horizontal plot, however, looks considerably different since the large scale pressure field is now in near-geostrophic balance with the winds. A southward turning of the winds is evident due to a slight imbalance of the initially specified pressure field and the wind field after its rapid adjustment to the mountain barrier. The small amplitude noise that develops late in the simulation is apparent in the isobars in Fig. 8. Despite this low level of noise, Fig. 9 indicates that the solution is quite steady after the initial adjustment period, and this is confirmed in Fig. 10 which shows the superimposed sea-level pressure fields for 8 h, 10 h, and 12 h. For completeness, Fig. 11 shows a cross section of potential temperature for the CGM domain. The solution shown in the central region

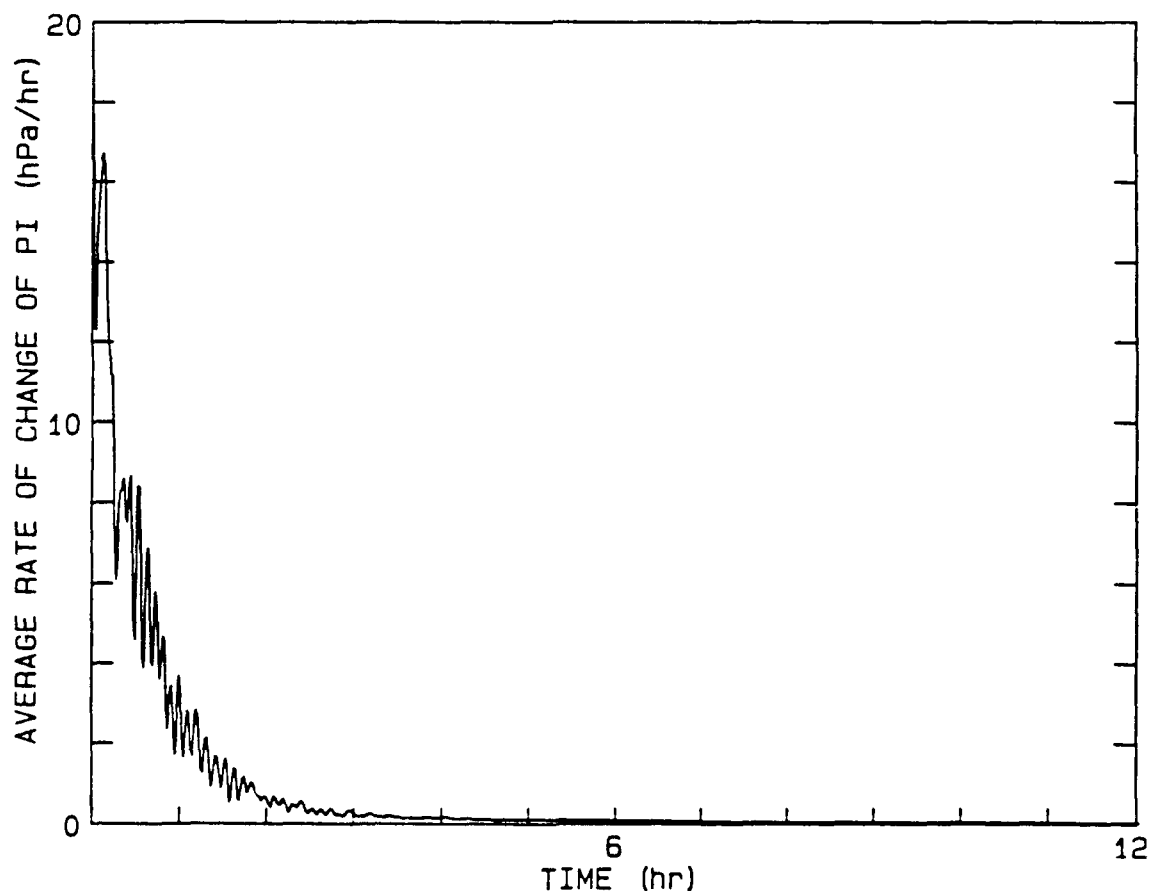


Fig. 9. Average rate of change of π versus time for FGM domain during the simulation shown in Figs. 7 and 8.



Fig. 10. Sea-level pressure fields at 8 h, 10 h, and 12 h, for the simulation shown in Figs. 7-9. Solid contours give sea-level pressure (in mb), thin dashed contours are for surface topography (in m) of the mountain ridge.

(between the vertical dashed lines) is actually the FGM solution averaged to CGM grid points. Note the smoothness of this solution, even at the FGM/CGM interface.

Figure 12 shows a potential temperature cross section for a 12 hour simulation in which the boundary layer was specified to be fairly thin. For this simulation $\sigma_h = 0.96$, which leads to a boundary layer thickness of about 36 mb (or about 308 m). In all other respects this simulation was identical to that shown in Fig. 7. The change in boundary layer depth affects the locations of all levels in the model, so the vertical resolution aloft is even coarser than before. The qualitative features of the solution are quite similar to the other simulations, but some differences are worth noting. Keeping the lowest layer much thinner increases the influence of the mountain on the boundary layer wind field, as can be seen by comparing Fig. 13 with Fig. 8. For the thin boundary layer case (Fig. 13), the upwind deceleration of the winds is more pronounced, resulting in a sharper

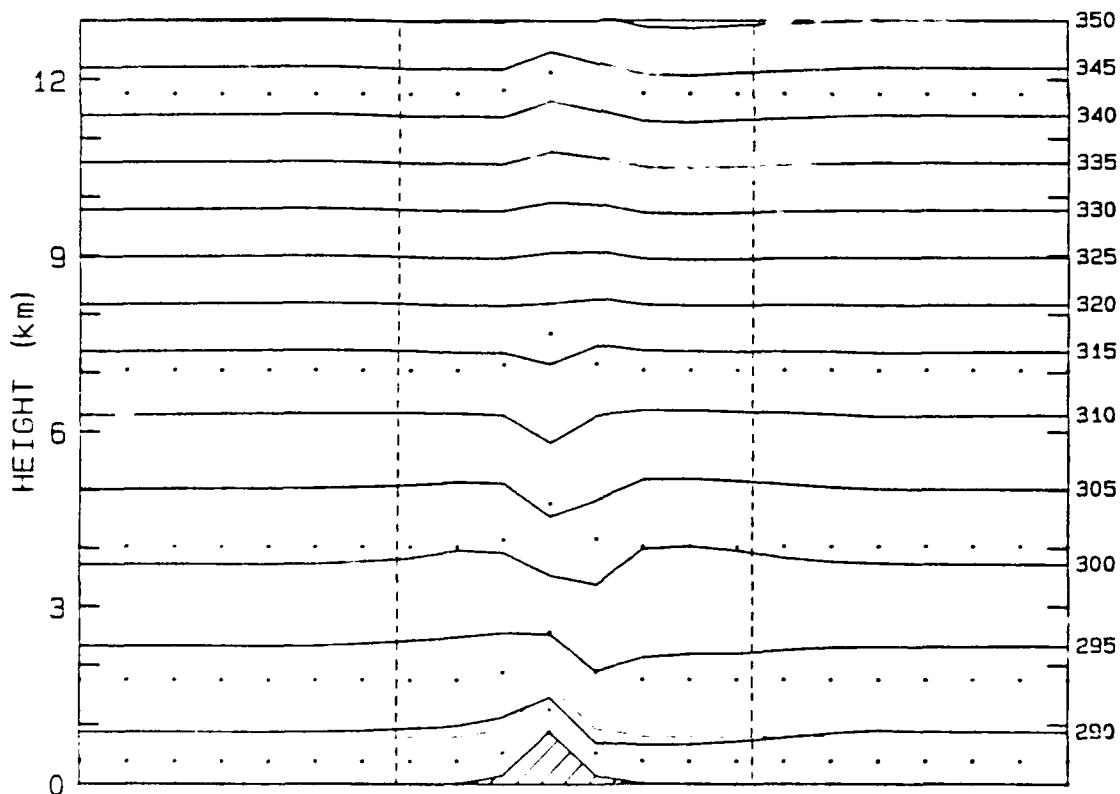


Fig. 11. Vertical cross section of potential temperature through CGM domain at 12 h for simulation shown in Figs. 7-9. The vertical dashed lines represent the FGM/CGM interface location.

upwind ridge, and there is more lateral deflection of the winds around the mountain ridge.

Figures 14 and 15 show the opposite situation, where the boundary layer height was set to be thicker than in previous runs. Here, $\sigma_h = 0.80$, which results in a boundary layer thickness of about 181 mb (about 1645 m). For this value of σ_h , the model's five layers are equally spaced in σ . The discussion of the previous paragraph holds in reverse now, as the mountain has less influence on the boundary layer winds since the boundary layer top is now well above the top of the ridge. It is interesting to note that the $2\Delta x$ noise is somewhat greater for the thick boundary layer than it is for the thin one.

Since there is no imposed (or implied) capping inversion of the boundary layers in these simulations, the differences in the solutions for the different σ_h values are purely an artifact of the lack of sufficient vertical resolution. Given

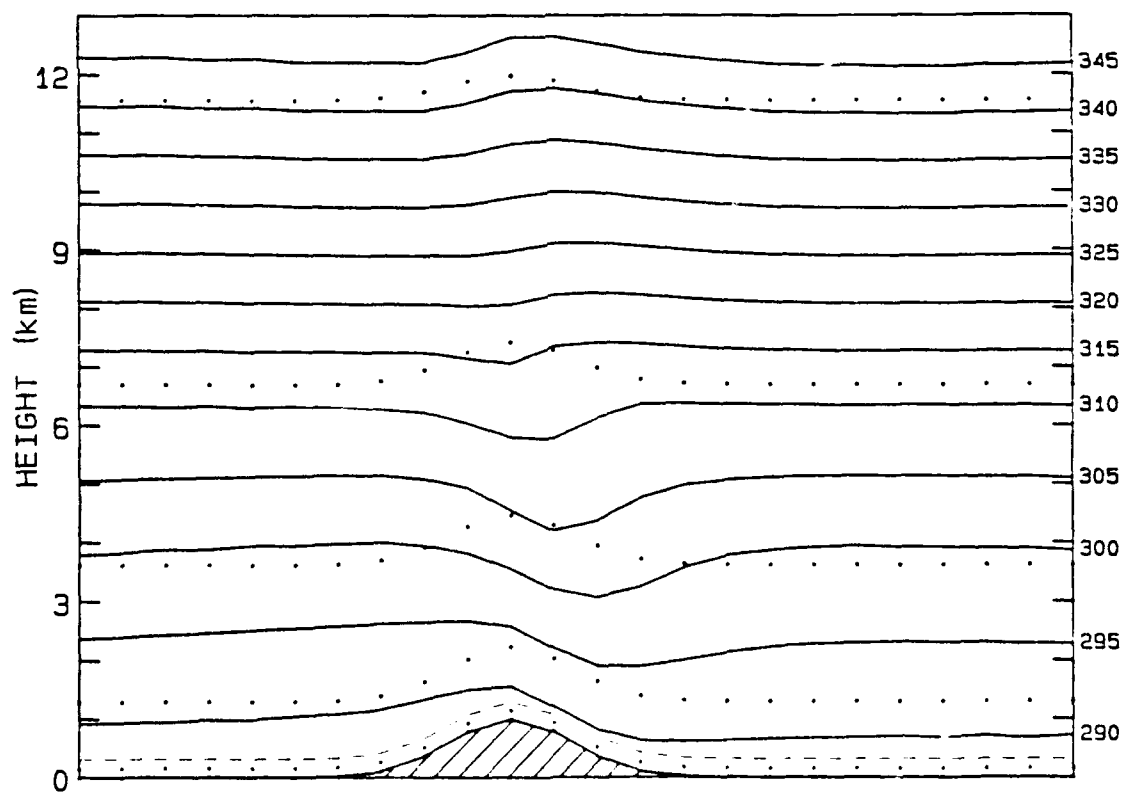


Fig. 12. Vertical cross section of potential temperature through FGM domain at 12 h showing potential temperature for thin boundary layer simulation ($\sigma_h = 0.96$).

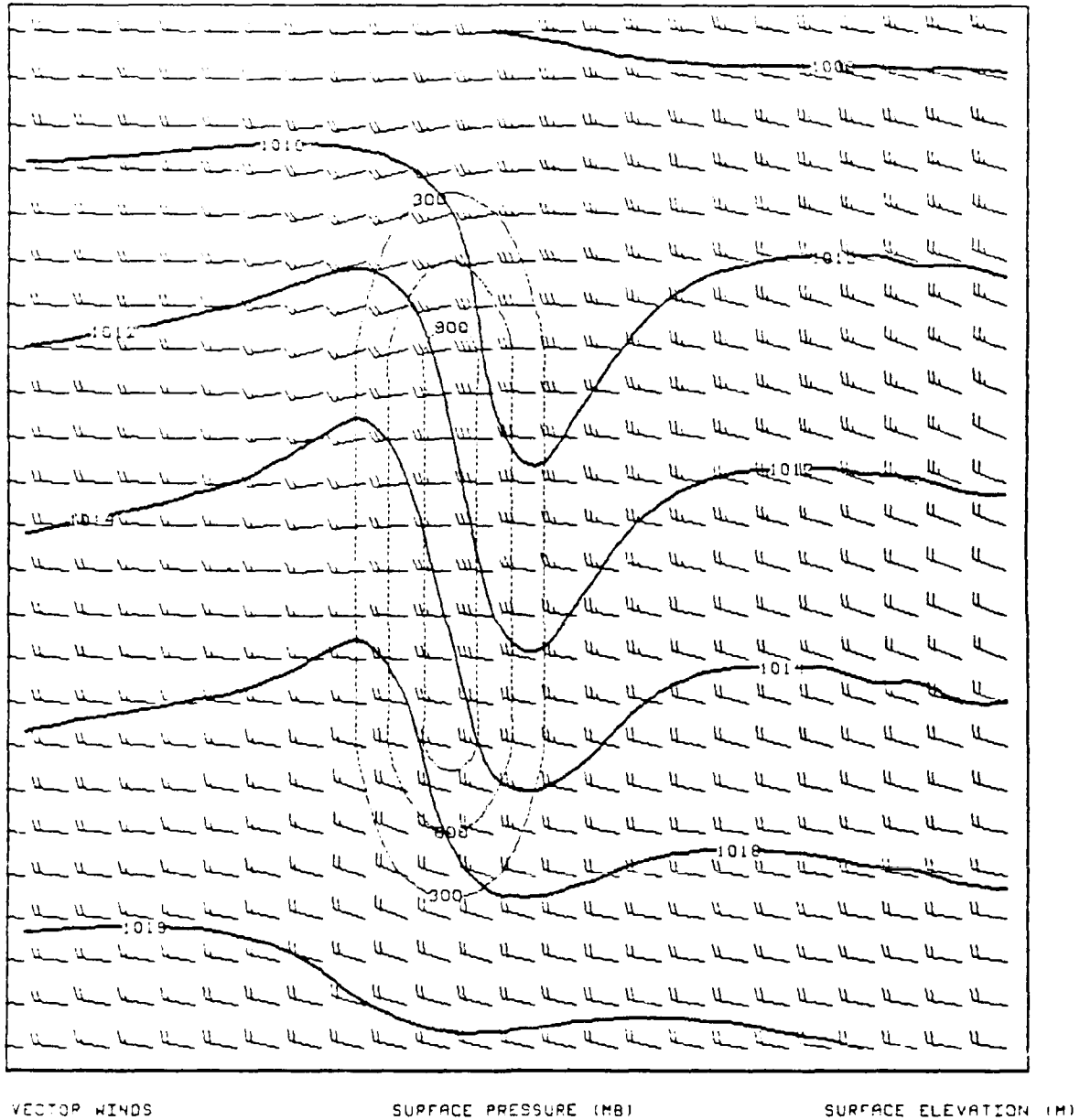


Fig. 13. Horizontal plot of FGM domain at 12 h for thin boundary layer simulation ($\sigma_b = 0.96$). Solid contours give sea-level pressure (in mb), thin dashed contours are for surface topography (in m) of the mountain ridge, and boundary layer winds (one full barb represents 10 m s^{-1}) are plotted at each grid point.

many layers, the model would resolve more flow around the mountain in the lowest layers and somewhat less in the layers just above the surface. The current model must be viewed as providing a sense of the average flow over the layer defined here as the boundary layer. Since each solution represents a different approximation of this type, each solution will present slightly different fields of winds, pressure and temperatures. The fact that the solutions are very similar over a wide range of boundary layer depths lends support to the ability of the η -coordinate system to represent the real atmosphere.

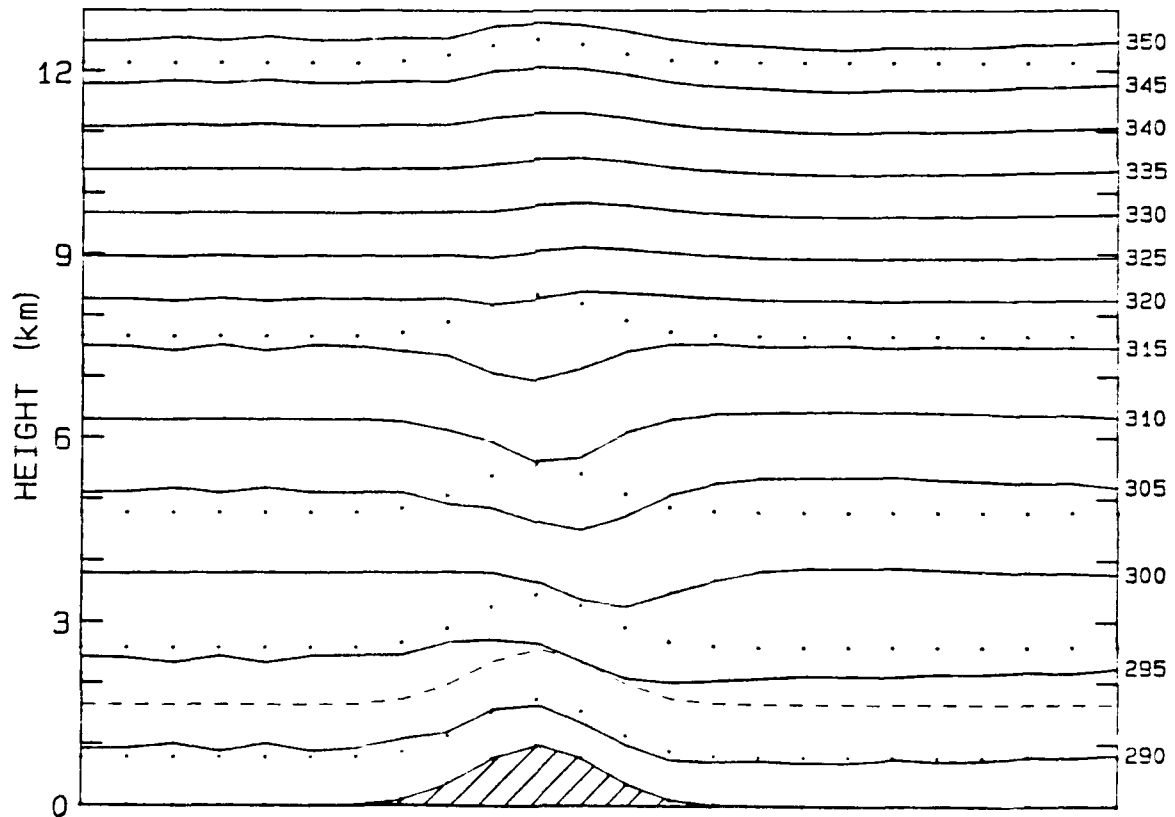


Fig. 14. Vertical cross section through FGM domain at 12 h showing potential temperature for thick boundary layer simulation ($\sigma_h = 0.80$).

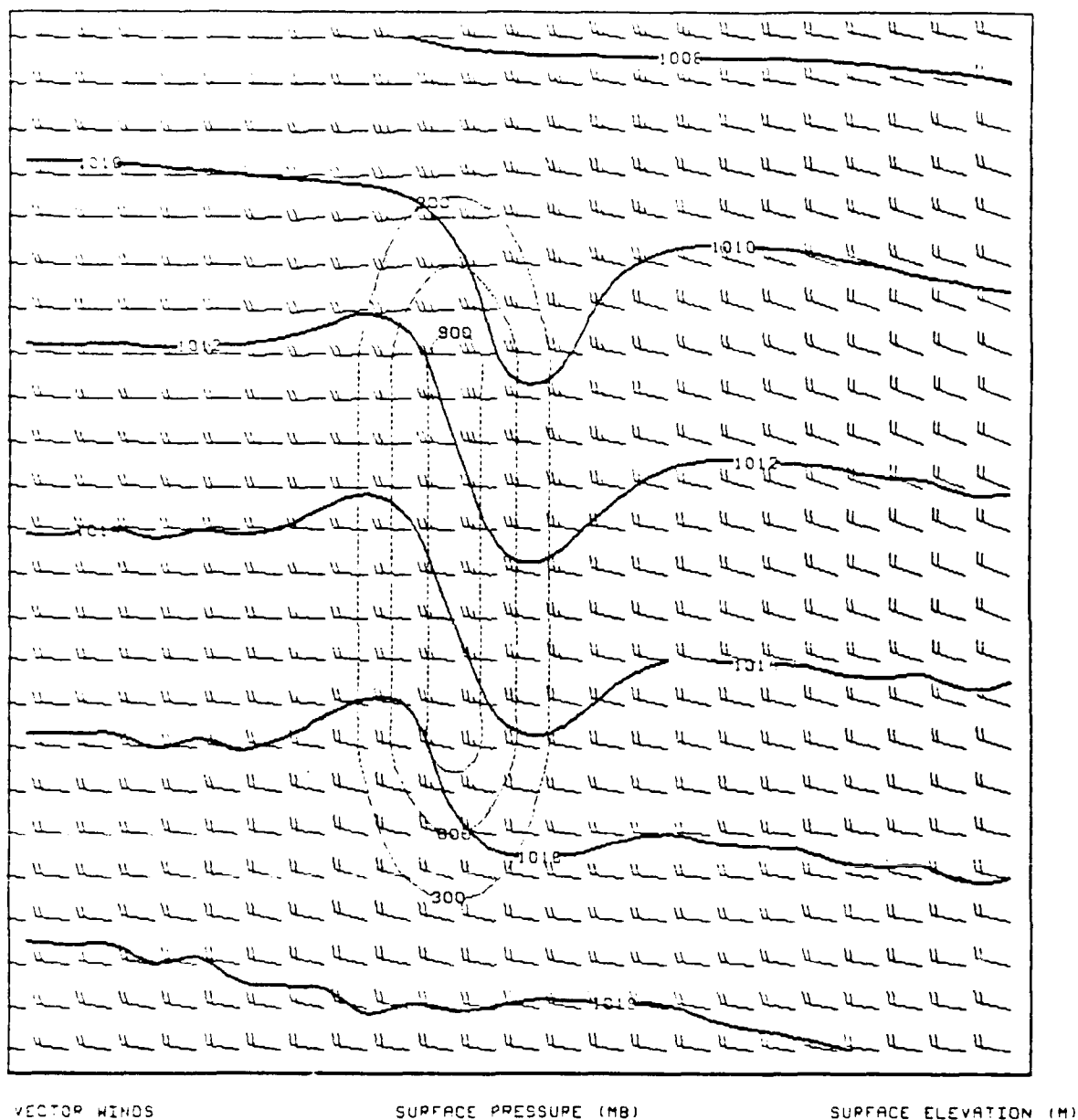


Fig. 15. Horizontal plot of FGM domain at 12 h for thick boundary layer simulation ($\sigma_s = 0.80$). Solid contours give sea-level pressure (in mb), thin dashed contours are for surface topography (in m) of the mountain ridge, and boundary layer winds (one full barb represents 10 m s^{-1}) are plotted at each grid point.

b. Experiments with a changing boundary-layer height

The simulations presented in the previous section all treated the boundary layer height, σ_h , as a constant for the entire period of the integration. Inspection of the equation set shows that if $d\sigma_h/dt = 0$, the model reduces to a σ -coordinate model. It is therefore important to test the ability of the model to maintain the proper atmospheric structure even when the boundary layer height is changing. A simple example of this is shown in Figs. 16a and 16b. These show the results of two separate integrations after 4 h simulated time, with flat terrain and a u -component velocity of 20 m s^{-1} at all levels. Figure 16a has a constant boundary layer height at $\sigma_h = 0.96$, and shows essentially no change during the integration. For Fig. 16b, however, the model was initialized with $\sigma_h = 0.96$ throughout the domain, but the boundary layer height was artificially forced upward in the central region of the FGM by specifying dh/dt as a Gaussian forcing function whose central value was 400 m h^{-1} . As can be seen in Fig. 16b, this resulted in the dynamic adjustment of the model layers to the changing boundary layer thickness, but the isentropic surfaces remained nearly horizontal — as they should. An interesting aspect of the η -coordinate model is that even though the flow is horizontal in physical space, because of the upward bulge of the η surfaces there is a significant flow through the surfaces that represents a vertical velocity in the η system. Figure 17 shows the geostrophic adjustment for both simulations in terms of the rate of change of surface pressure (note the scales are expanded compared to previous figures of this type). As can be seen, the movement of the σ_h surface has no effect on the adjustment process in the model.

A somewhat different experiment was carried out by forcing a rising boundary layer during a lee-wave simulation. In this case, the simulation started with $\sigma_h = 0.96$ throughout the domain and these conditions were held for 6 h simulated time. Then, the boundary layer was forced to rise by specifying $dh/dt = 400 \text{ m s}^{-1}$ at all grid points. This rate of rise was held until $\sigma_h = 0.80$ when the rate of rise was set back to zero (at about 9.3 h). Figure 18 shows a cross section for this simulation at 12 h. Comparison with Fig. 14 shows that the growth of the boundary layer did little to affect the final solution, despite the large change in physical elevation of the model surfaces and the implied vertical velocities that went along with the rising surfaces. Because the flow relaxation boundary condition applied on the lateral boundaries of the CGM holds the

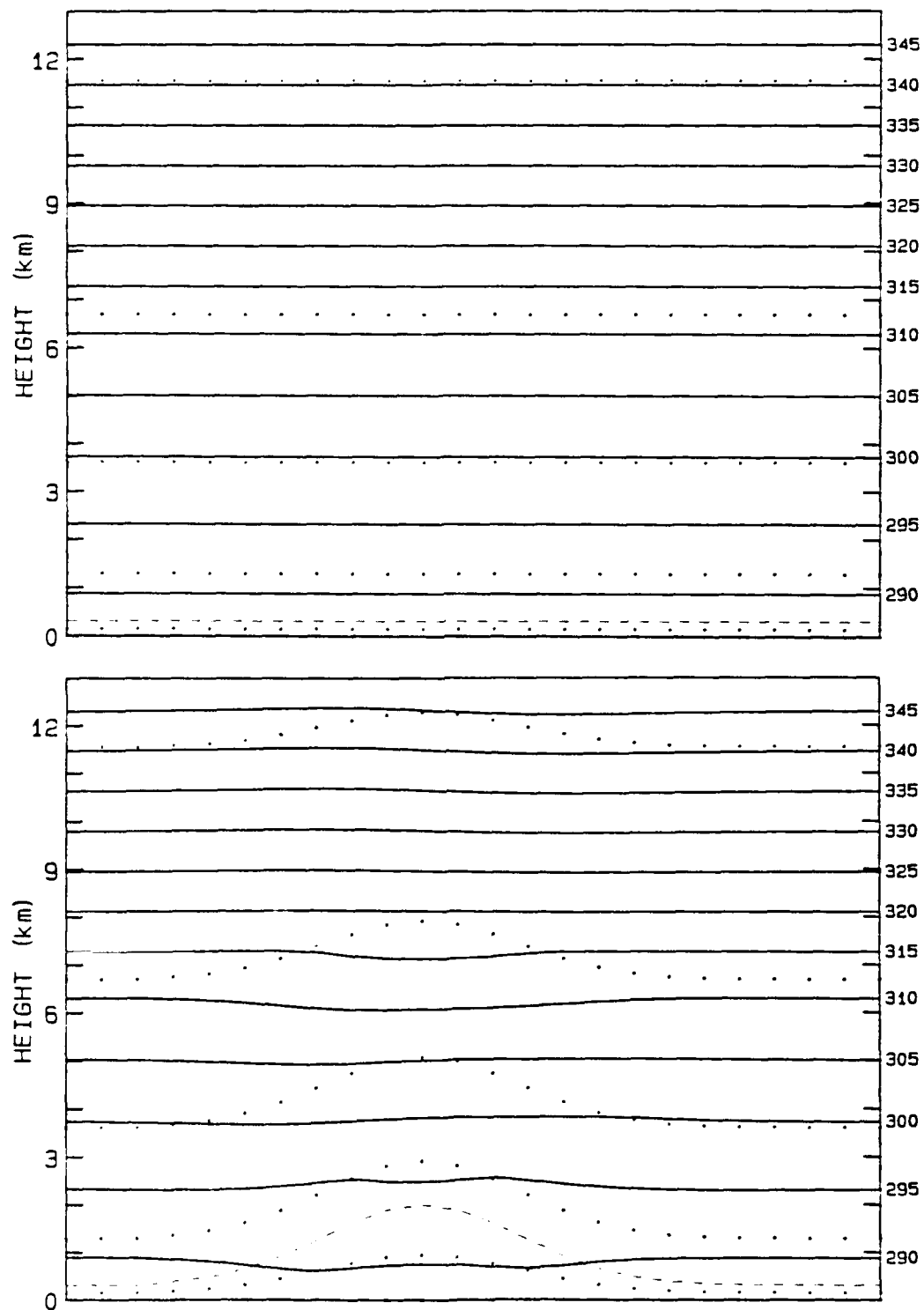


Fig. 16. Vertical cross section through FGM domain at 4 h showing potential temperature for flat terrain simulations with (a) constant boundary layer height and (b) boundary with artificial forced growth.

boundary values fixed, these boundary points retained a boundary layer height of $\sigma_h = 0.96$ throughout the simulation — requiring an additional adjustment process to take place in the CGM collar surrounding the FGM domain. A cross section through the CGM which shows this is shown in Fig. 19. There is some noise in and just above the boundary layer inside the relaxation region near the outer lateral boundaries, but the solution is really quite well-behaved. Figures 20, 21, and 22 show horizontal plots of the FGM sea-level pressure field at 6 h, 8 h, and 12 h, respectively. Figures 20 and 22 look almost identical to Figs. 13 and 15, as they should since they represent lee-wave solutions for the same vertical structure of the model. Figure 21 shows the solution while the boundary layer is growing, and although it is a little noisier, the solution is again quite well-behaved. In addition to the plots shown above, the lack of impact on the model's ability to simulate

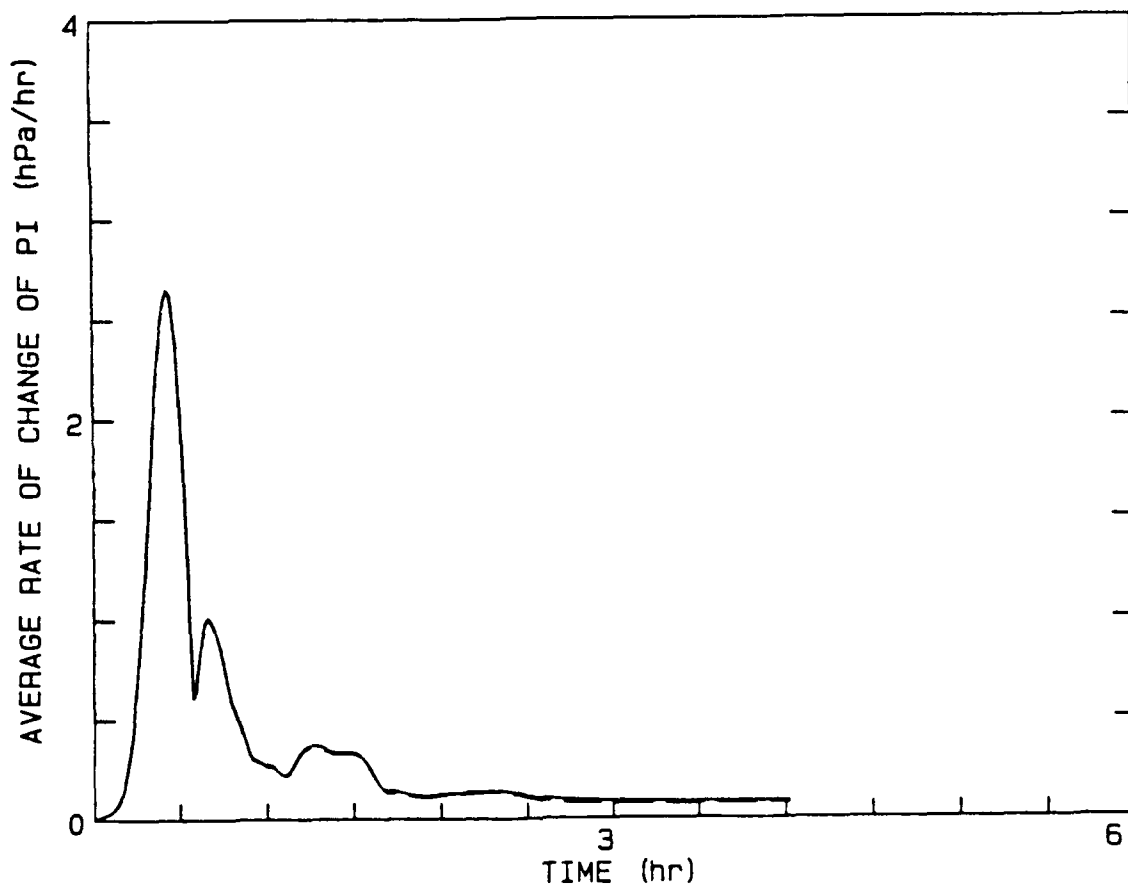


Fig. 17. Average rate of change of π versus time for FGM domain during the simulations shown in Figs. 16a (solid) and 16b (dashed). Note that dashed line only deviates from solid line at the end of the simulation.

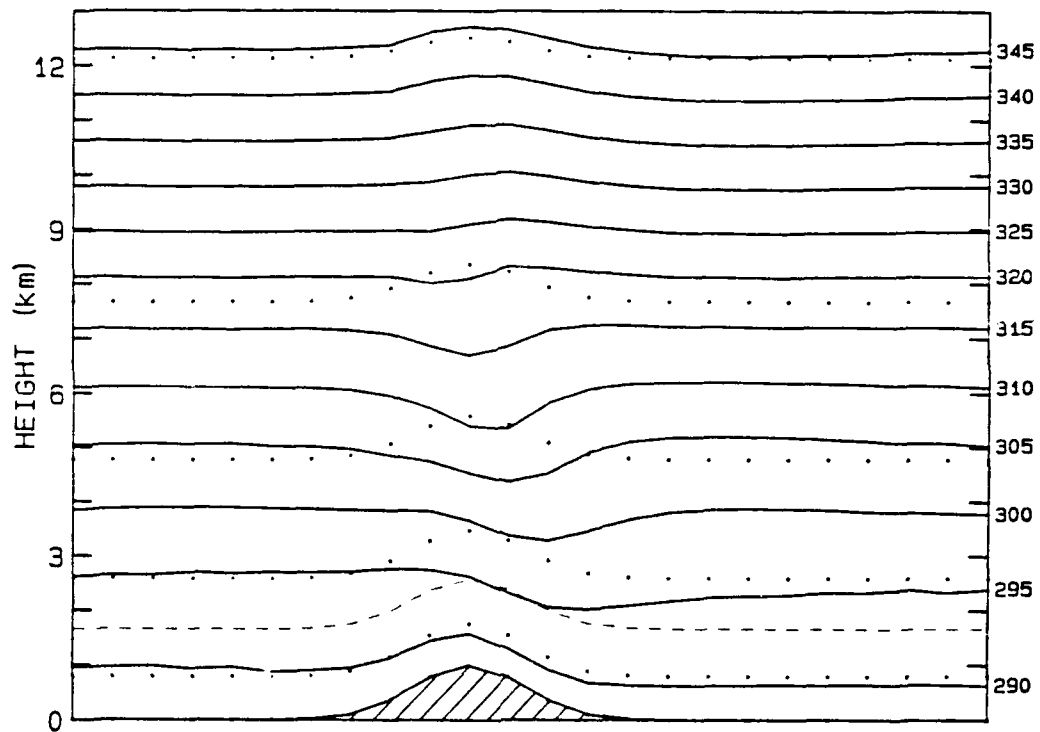


Fig. 18. Vertical cross section through FGM domain at 12 h showing potential temperature for rising boundary layer simulation.

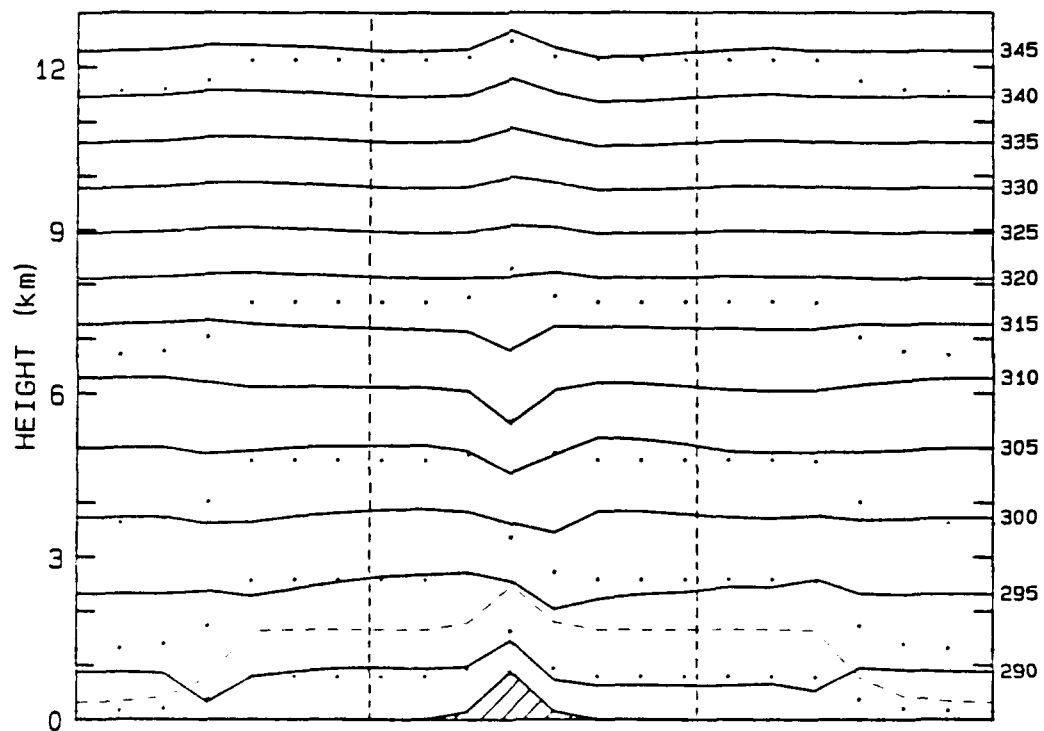


Fig. 19. Vertical cross section through CGM domain at 12 h showing potential temperature for rising boundary layer simulation.

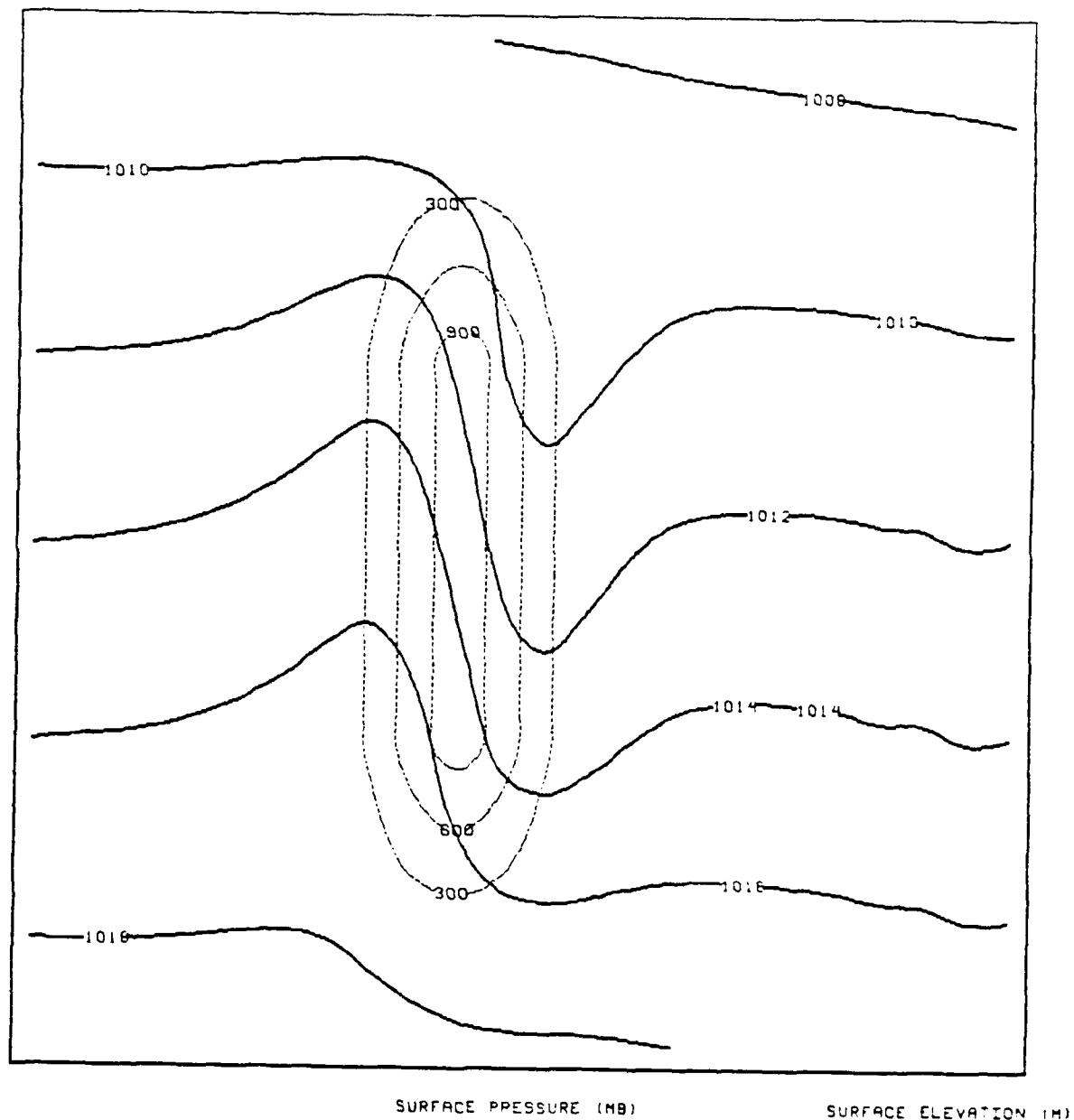


Fig. 20. Horizontal plot of FGM domain at 6 h for growing boundary layer simulation ($\sigma_h = 0.96$ at this time). Solid contours give sea-level pressure (in mb), thin dashed contours are for surface topography (in m) of the mountain ridge.

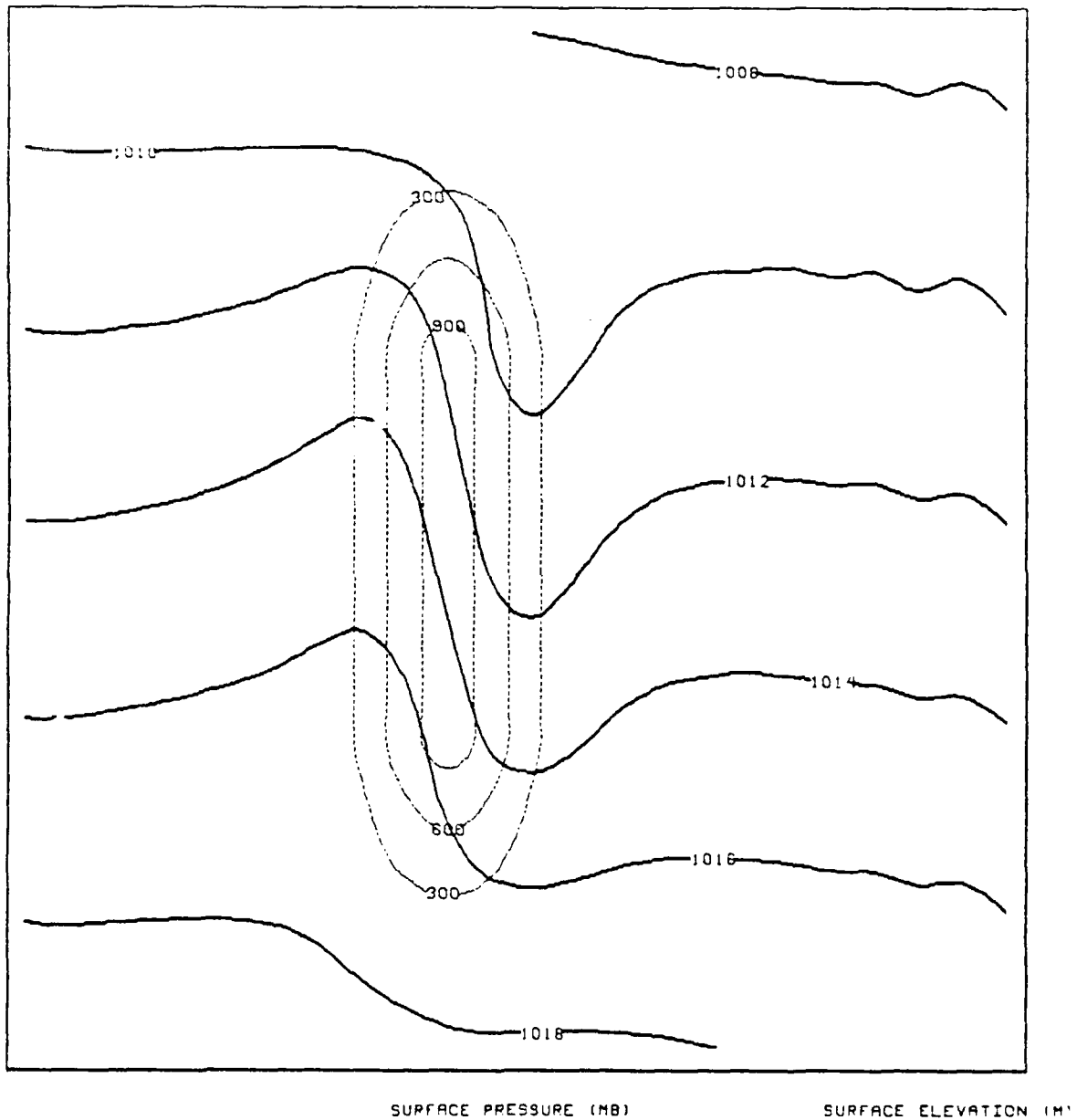


Fig. 21. Horizontal plot of FGM domain at 8 h for growing boundary layer simulation ($\sigma_n \approx 0.86$ at this time and is rising at 400 m s^{-1}). Solid contours give sea-level pressure (in mb), thin dashed contours are for surface topography (in m).

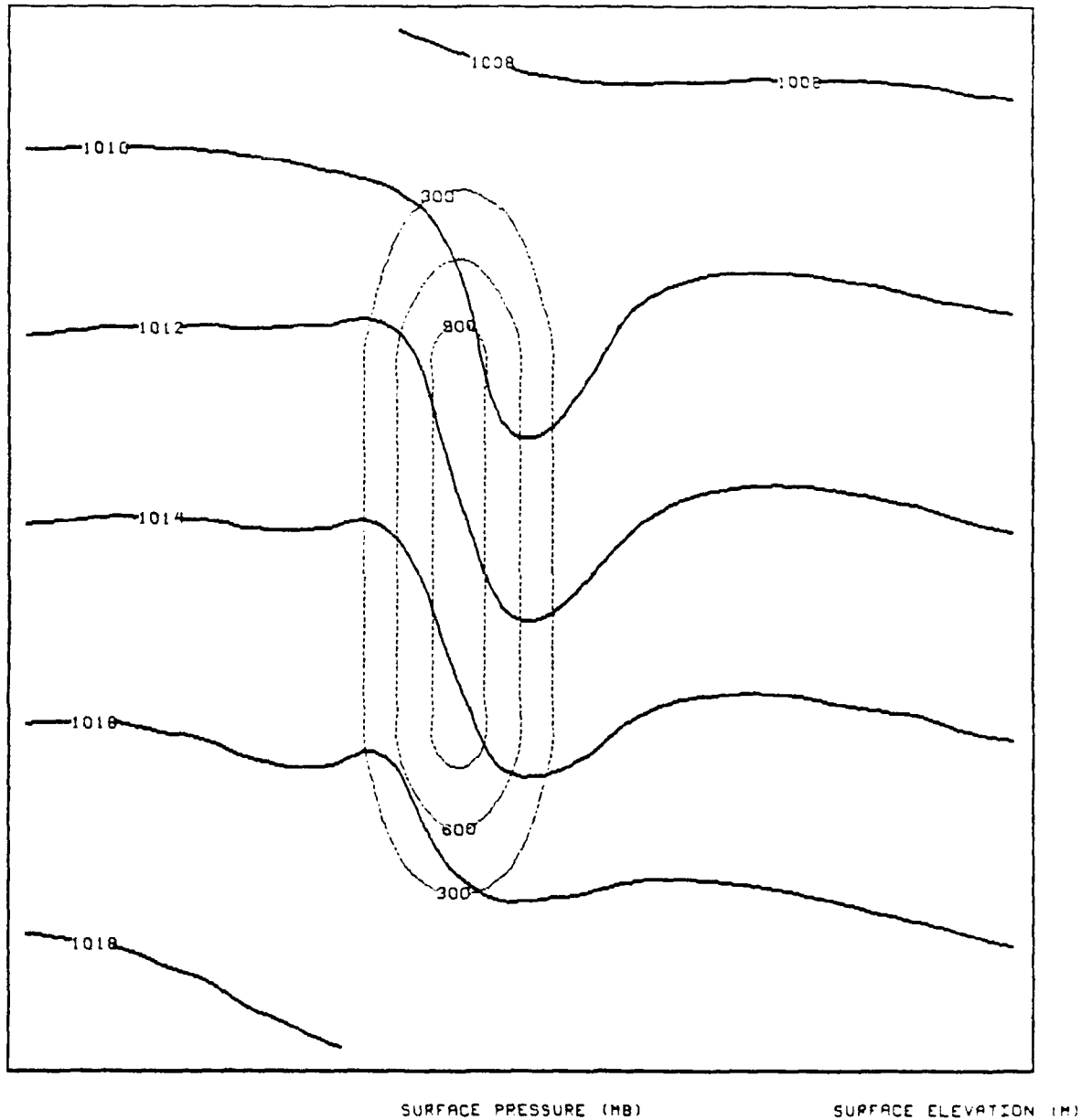


Fig. 22. Horizontal plot of FGM domain at 12 h for growing boundary layer simulation ($\sigma_h = 0.80$ at this time). Solid contours give sea-level pressure (in mb), thin dashed contours are for surface topography (in m).

the lee-wave phenomenon despite a drastic change in boundary layer height is shown in Fig. 23. Here the average rate of change of π is plotted for the simulation discussed here. While a very small adjustment in the model is apparent between 6 h and 12 h while the boundary layer is rising, it is clear that the model equations allow the boundary layer change to occur without disturbing the geostrophic balance within the model.

Several other simulations, which are not shown here, have been carried out in which the boundary layer was artificially raised or lowered to test the robustness of the η -formulation. In all cases, the model performed well. This includes an extreme case in which the Gaussian forcing function was imposed on a mountain lee-wave simulation for the full 12 h so that the boundary layer directly over the ridge grew to almost 9 km in depth. Even in this case the model solution remained stable, although the solution was not a very good simulation of lee-waves

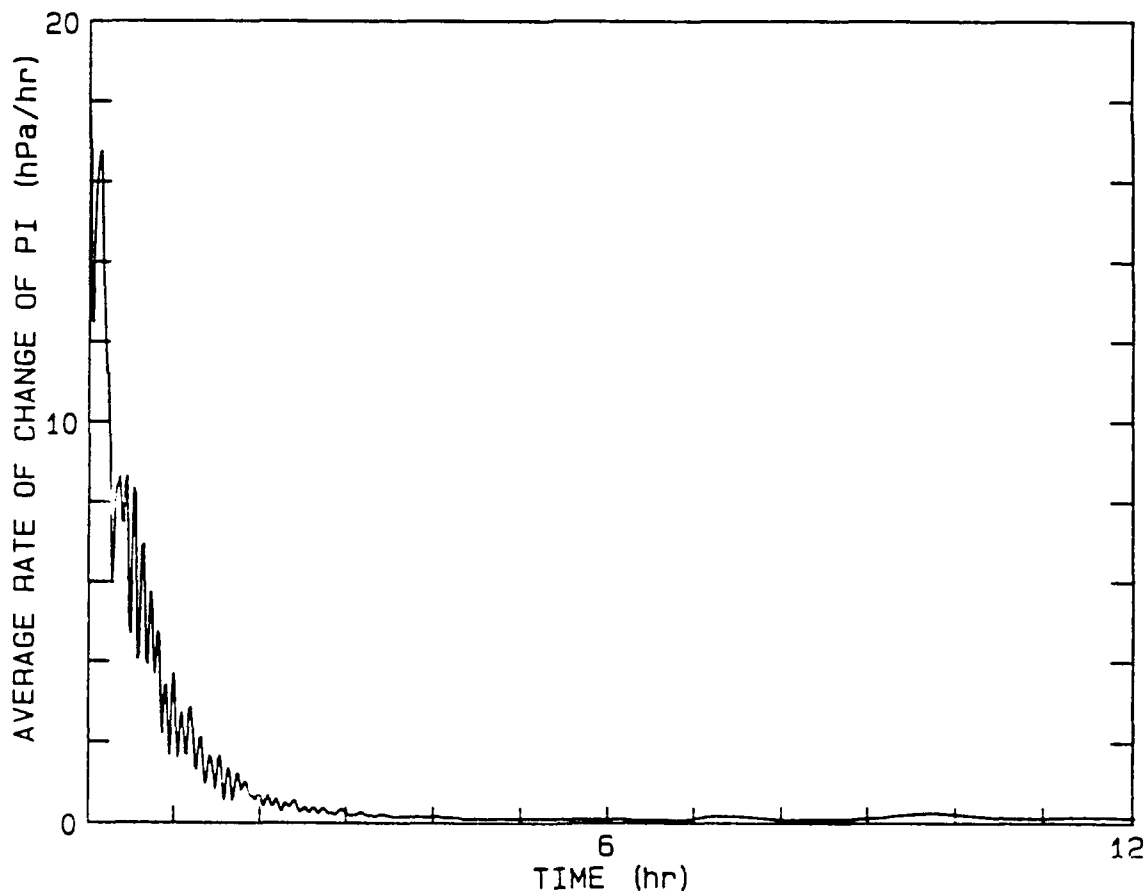


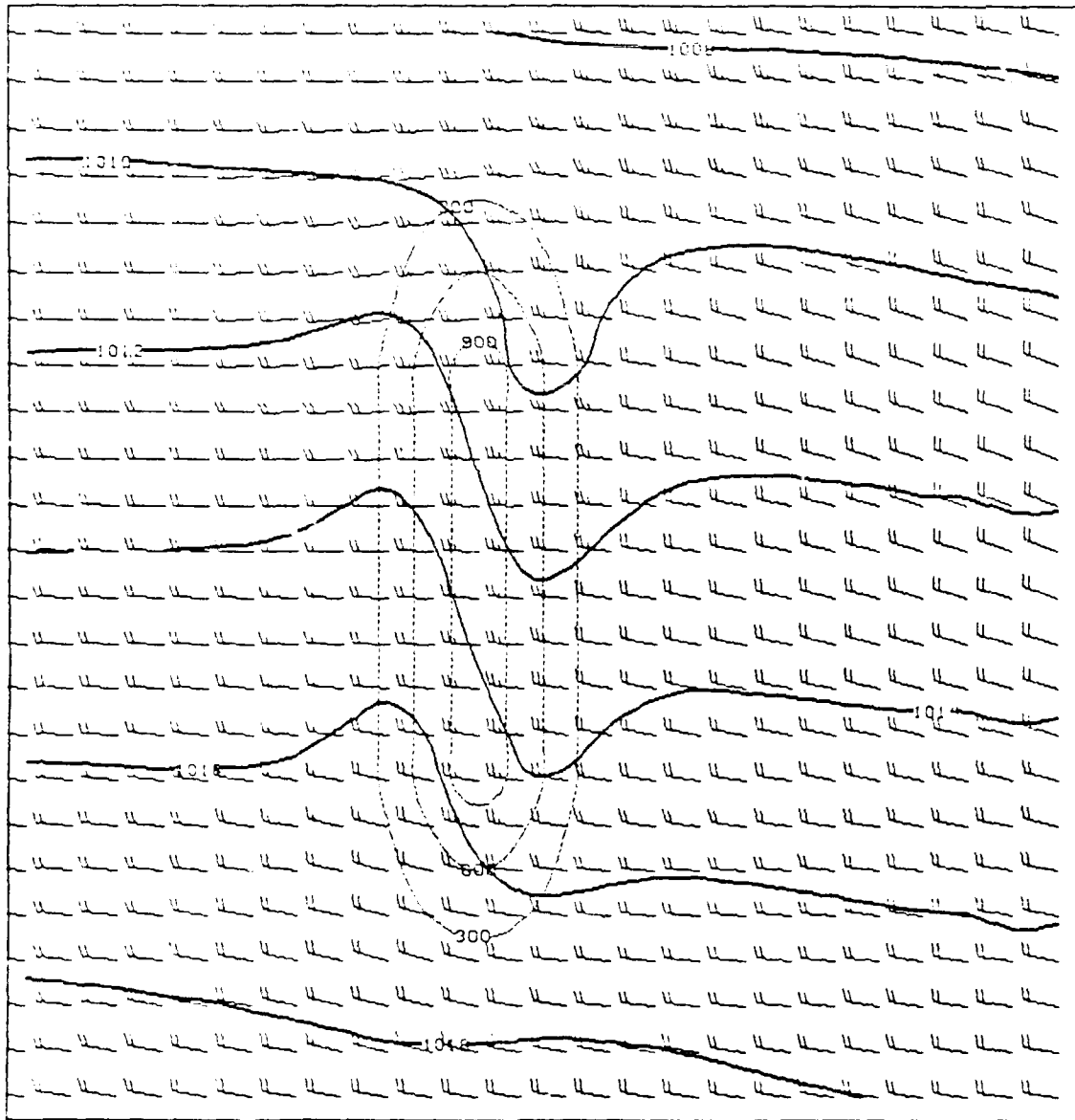
Fig. 23. Average rate of change of π versus time for FGM domain during the growing boundary layer simulation shown in Figs. 18–22.

since the lee-wave could not be resolved by the single very thick layer just above the mountain.

c. Eddy diffusion sensitivity tests

All of the simulations shown in this section were carried out with no diffusion on temperature and no additional smoothing operators on any variables near the FGM/CGM interface. This was desirable in early testing so that even small incompatibilities between CGM and FGM solutions, errors in coding, or accumulating errors due to a nonconstant boundary layer depth would be readily apparent. It is clear from inspection of Fig. 8, for example, that some noise is present in the model that should be removed by smoothing. Figure 10 shows that there are actually two types of noise present. On the eastern boundary is a steady $2\Delta x$ noise that is related to the overspecification of pressure on the outflow FGM/CGM interface and its impact on the velocities. We will call this the "outflow noise." The western half of the domain, upwind of the mountain ridge also has some $2\Delta x$ noise which appears more transient. This appears to be simply the noise that is typical in primitive equation models when the nonlinear advective terms are present, and is related to the lack of any smoothing on temperature. This noise is easily removed by adding even a very small amount of diffusion to the temperature. Figure 24 shows a horizontal plot of a lee-wave simulation with $\sigma_h = 0.80$ in which an eddy diffusion coefficient of $K = 1 \times 10^4 \text{ m}^2 \text{ s}^{-1}$ was specified for temperature. This value is only 0.05 times that used for the momentum terms. We chose to use $\sigma_h = 0.80$ for this simulation because the noise is somewhat more apparent in the thick boundary layer simulations (see Figs. 14 and 15). Note that while the extra diffusion on temperature removed the regular noise in the western portion of the domain, it did not affect the "outflow noise" on the eastern boundary.

Zhang et al. (1986) used both the Newtonian damping scheme discussed in section 2 and a larger eddy diffusion coefficient near the FGM/CGM interface to control the noise produced by the overspecification of pressure on outflow boundaries. Figure 25 shows a simulation (again with $\sigma_h = 0.80$) in which there is no diffusion on temperature but the Newtonian damping scheme is used on the momentum terms (with $\tau_d = 20\Delta t$). While this reduces the outflow noise, it does not eliminate it. Additional tests (not shown) indicated that additional eddy diffusion was required near the boundary to remove this noise. As discussed in



VECTOR WINDS

SURFACE PRESSURE (MB)

SURFACE ELEVATION (M)

Fig. 24. Horizontal plot of FGM domain at 12 h for simulation with weak diffusion on temperature ($\sigma_s = 0.80$). Solid contours give sea-level pressure (in mb), thin dashed contours are for surface topography (in m) of the mountain ridge, and boundary layer winds (one full barb represents 10 m s^{-1}) are plotted at each grid point.

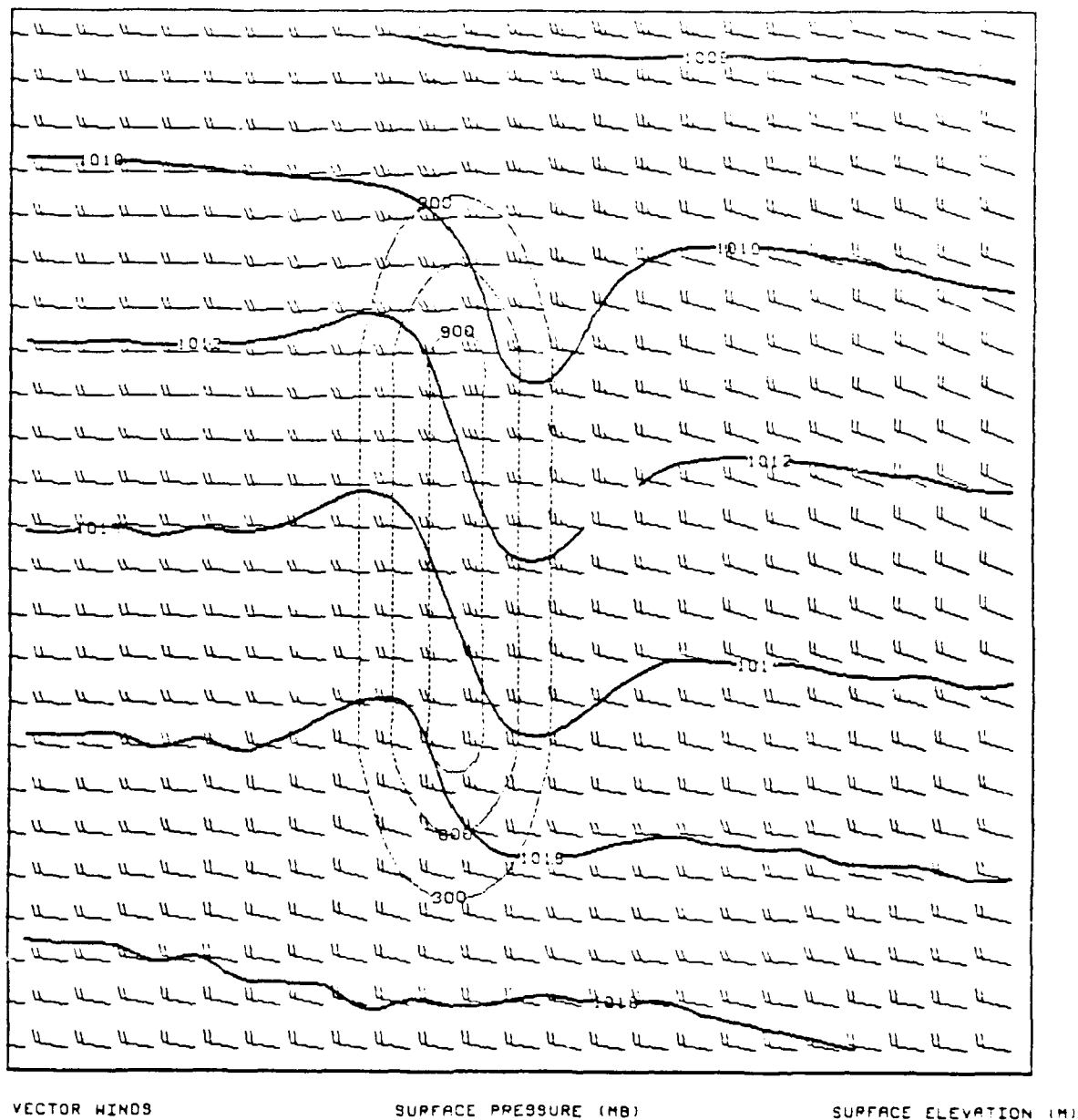


Fig. 25. Horizontal plot of FGM domain at 12 h for simulation with Newtonian damping on momentum terms at the CGM/FGM interface ($\sigma_h = 0.80$). Solid contours give sea-level pressure (in mb), thin dashed contours are for surface topography (in m) of the mountain ridge, and boundary layer winds (one full barb represents 10 m s^{-1}) are plotted at each grid point.

section 2, the Newtonian damping scheme, as applied here, reduces to a simple filter and is nearly identical to increased diffusion. We therefore decided to simply control this noise by increasing the diffusion near the boundary.

The combination of these two noise control techniques results in simulations such as that shown in Fig. 26. For this simulation, the eddy diffusion on temperature is included (as in Fig. 24), and the diffusion on all terms is modified near the FGM/CGM interface to be twice the interior value 2 grid intervals away from the interface and three times the interior value 1 grid interval from the interface. This modest additional smoothing affects the simulation in only minor ways and greatly reduces the noise. Some of the modification of the isobar pattern near the mountain is a result of the small accumulating error discussed by SC which occurs whenever diffusion is applied to temperature on σ or η surfaces in complex terrain. The very small value of the diffusion parameter makes this error small enough to provide acceptable results even in this very steady flow, and it should be unnoticeable in a more transient flow.

Figures 27 and 28 provide the results for a simulation of the model with the added smoothing for $\sigma_h = 0.90$. These may be compared directly with Figs. 7 and 8. While there are some subtle differences, the simulation with the extra diffusion is a qualitatively good solution for mountain lee-waves and has very little noise. We feel that Figs. 27 and 28 represent the model as it will be run from now on.

4. Domain for Prototype Testing

An important aspect of this study is the testing of a prototype model using real data in clear weather and stratiform precipitation situations. Such testing requires a specific geographic location. Ideally, this location should experience a wide variety of weather phenomena such as sea-breeze circulations, synoptic scale stratiform precipitations events, orographic enhancement of precipitation, and other mesoscale patterns for which the model is intended to provide guidance. Southern New England represents one of several locations that could be considered, and given our obvious desire for operational guidance in our own area, we have chosen this geographic region for testing of the prototype model.

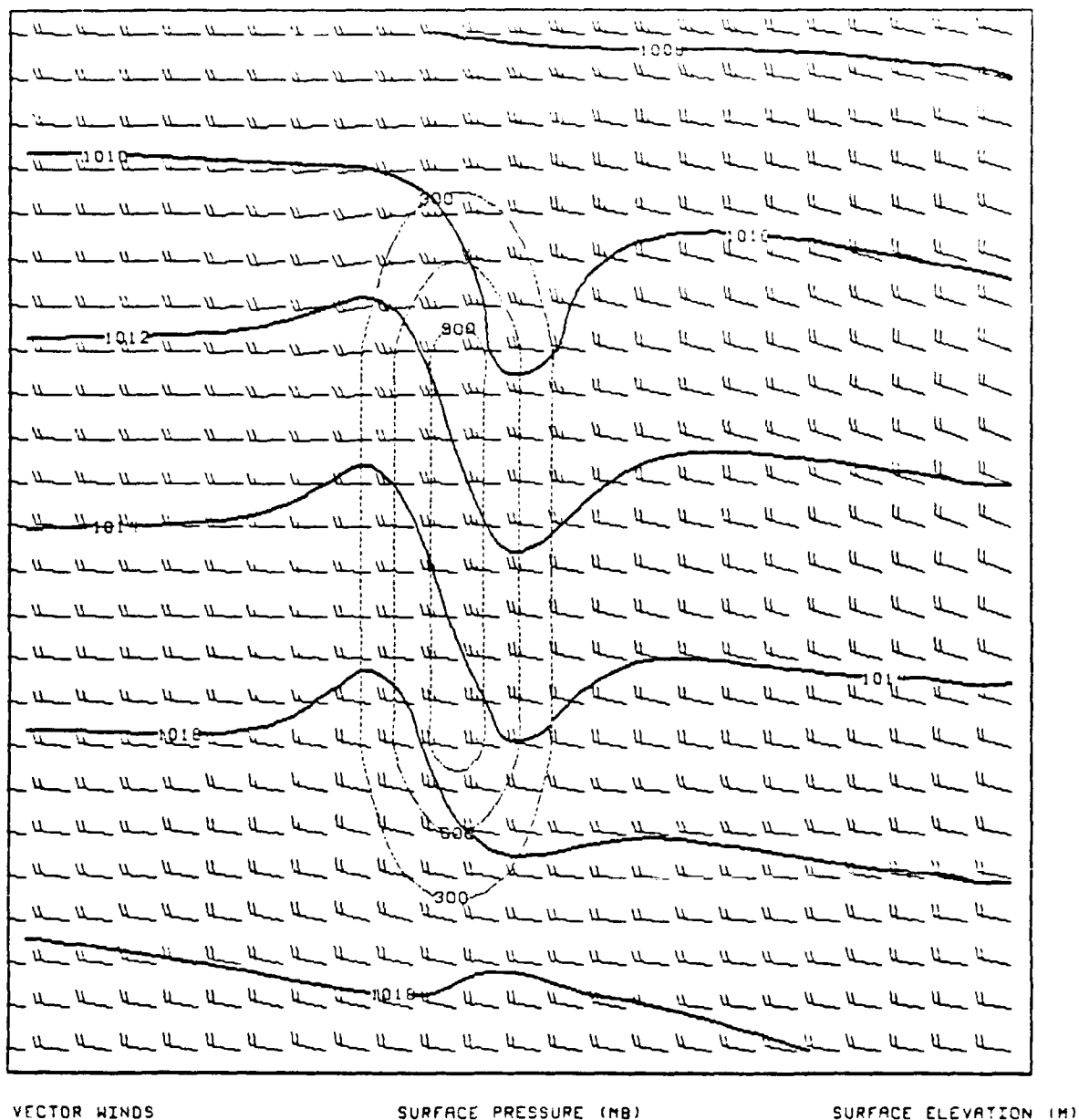


Fig. 26. Horizontal plot of FGM domain at 12 h for simulation with weak diffusion on temperature and extra diffusion near FGM/CGM interface ($\sigma_h = 0.80$). Solid contours give sea-level pressure (in mb), thin dashed contours are for surface topography (in m) of the mountain ridge, and boundary layer winds (one full barb represents 10 m s^{-1}) are plotted at each grid point.

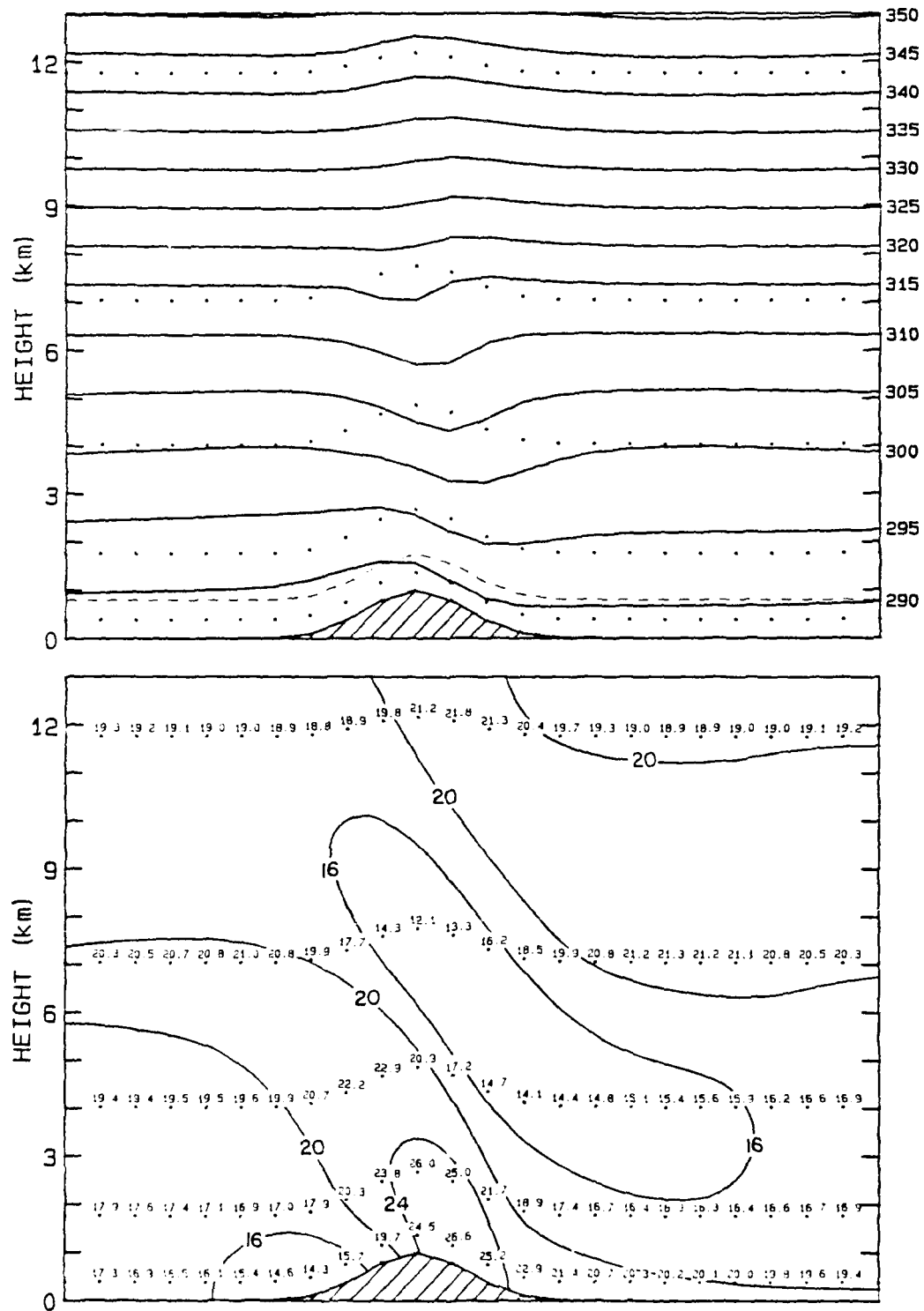


Fig. 27. As in Fig. 7, except for the added weak diffusion on temperature and extra diffusion near the boundaries.

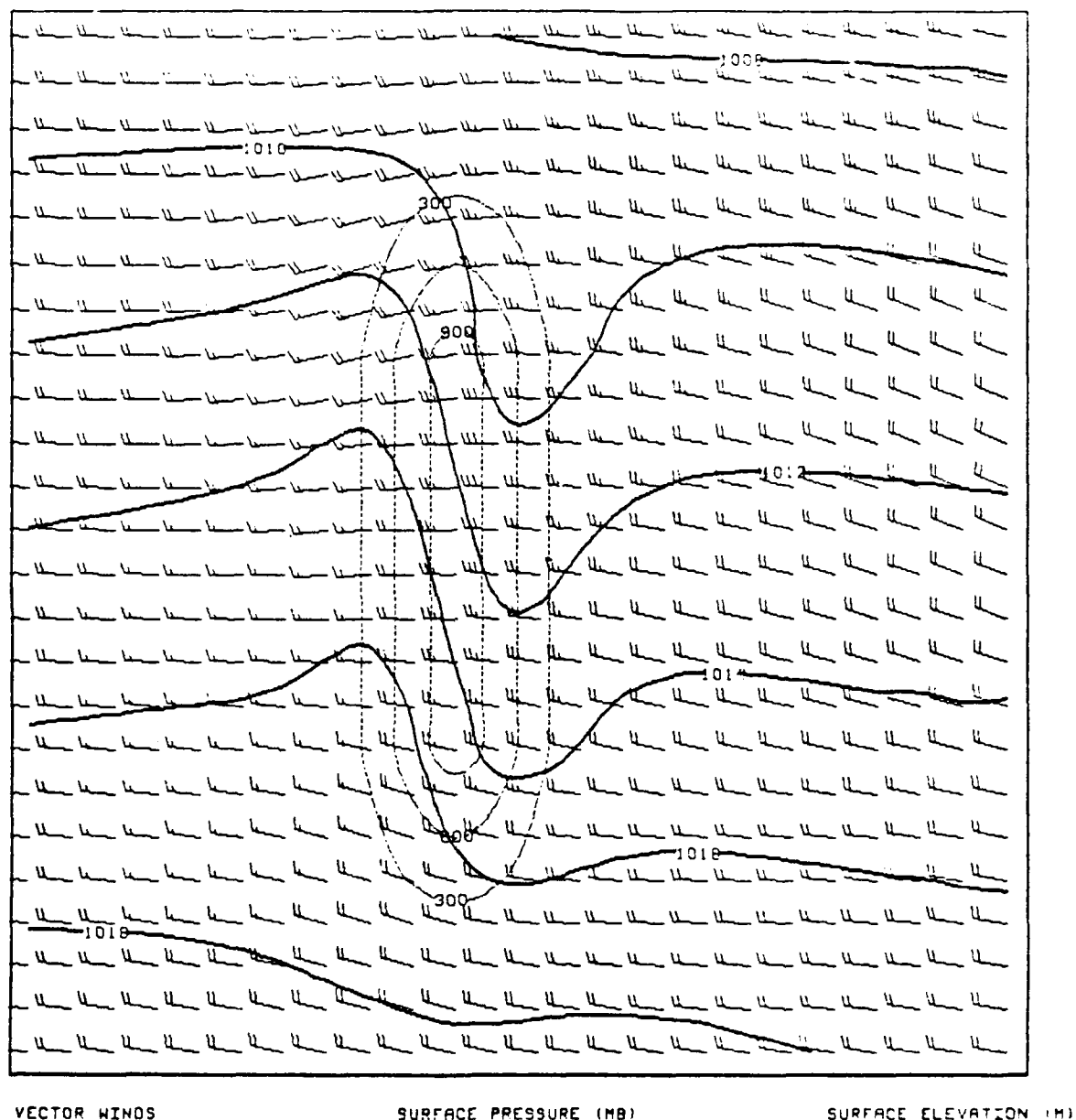
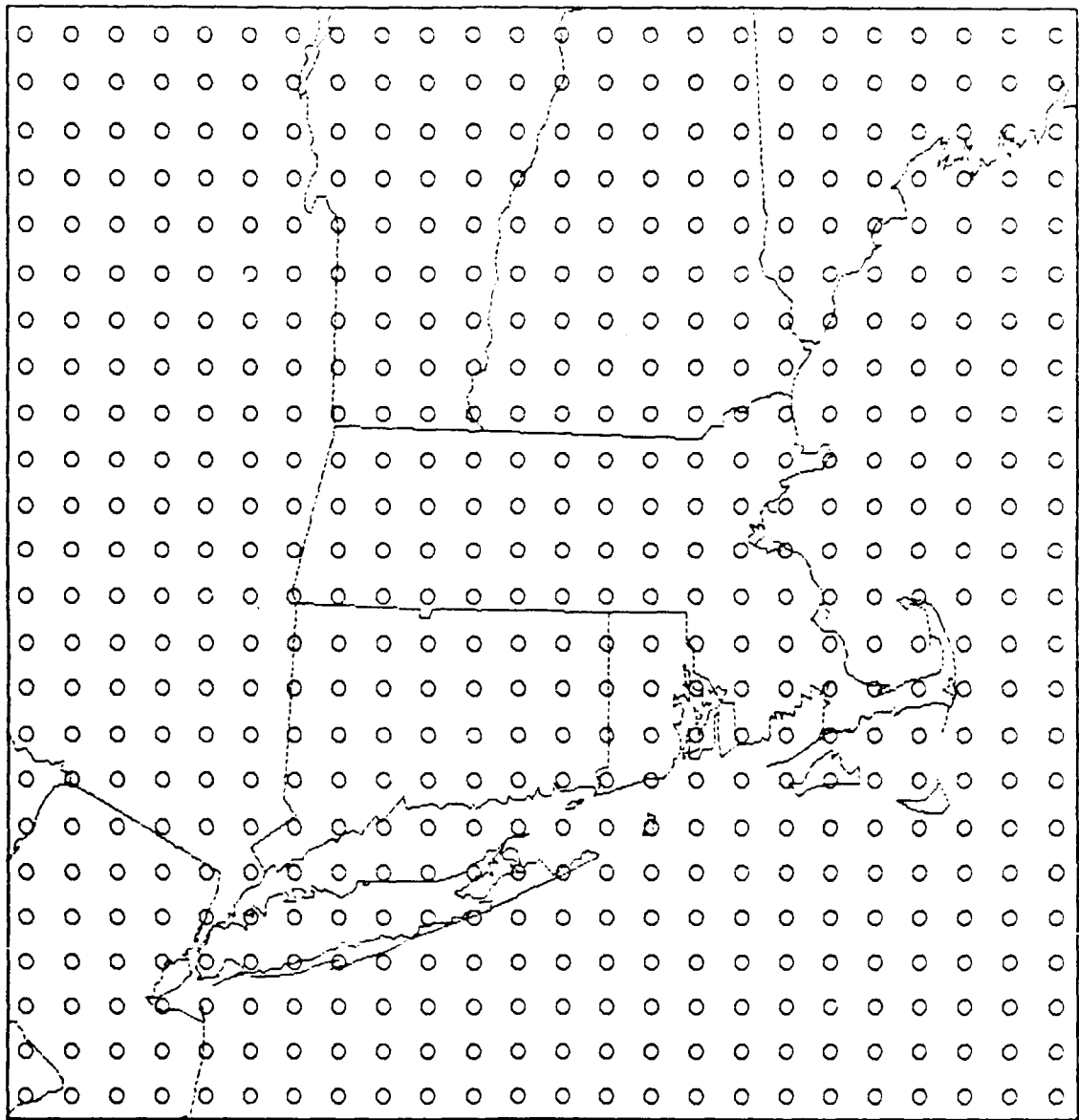


Fig. 28. As in Fig. 8, except for the added weak diffusion on temperature and extra diffusion near the boundaries.

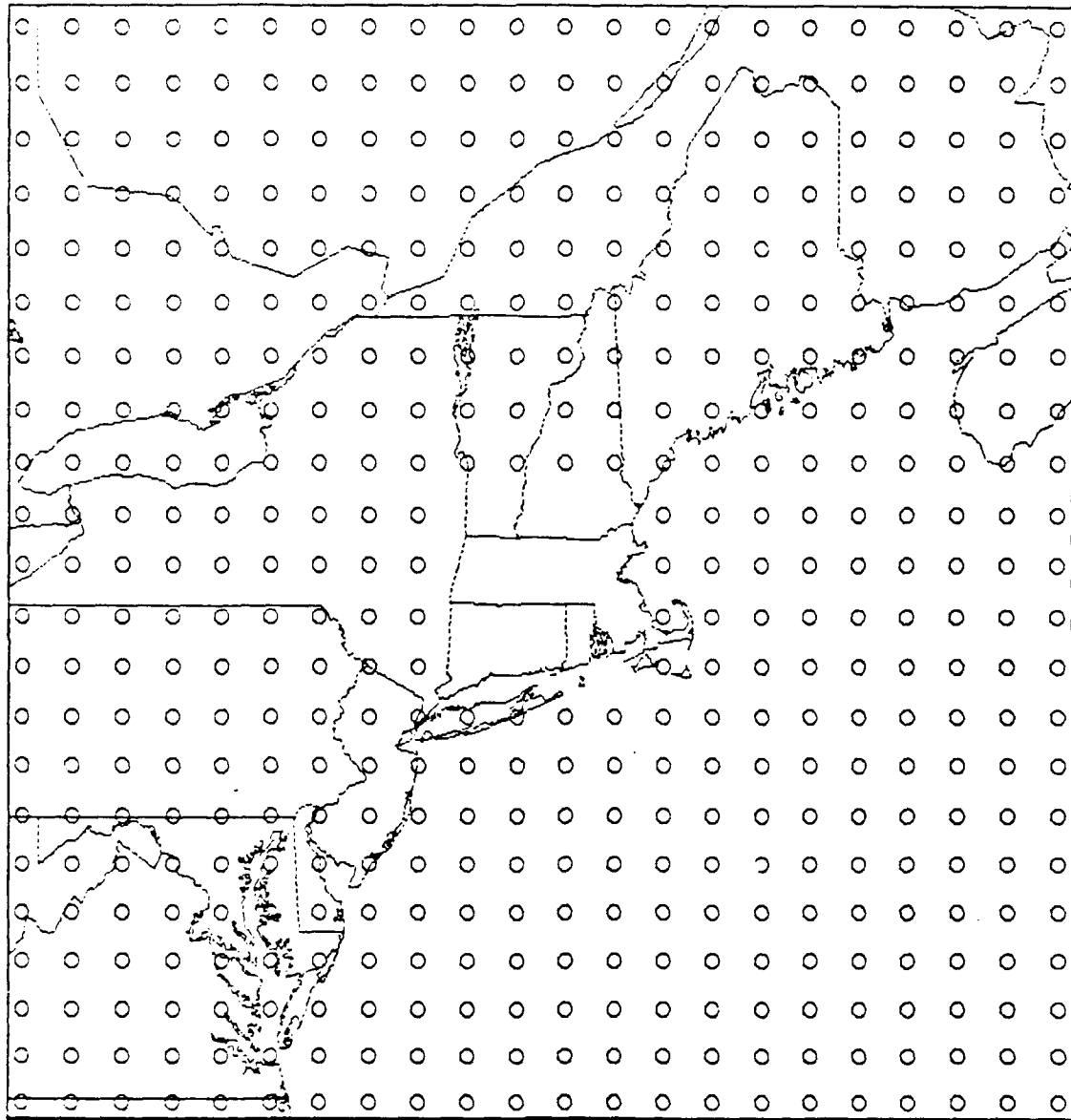
The domain for the fine grid mesh is shown in Fig. 29 (only the locations of "thermodynamic" grid points are shown). The coarse grid mesh which surrounds the FGM domain is shown in Fig. 30. In addition to being a coastal location, this area has complex terrain which is rich in detail on meso- β scales. This is quite evident in the contour plot of the topography shown in Fig. 31. This plot was constructed by reading the heights of FGM points directly from U.S. Geologic Survey topographic maps. The field is quite noisy at this 20 km resolution, so it is clear some processing is required. We anticipate that some form of "envelope" orography will provide the best overall representation of the effects of topography on the flow (Wallace et al. 1983). In order to compute an envelope field, the terrain heights were recorded for nine equally spaced points within each grid box. A full envelope is considered to be the mean of these nine points plus 2.0 times the standard deviation of them (we will refer to this multiplicative factor as the "envelope parameter"). A full envelope, with the envelope parameter equal to 2.0, results in some grid point elevations being considerably higher than any of the raw grid point heights. Therefore, we anticipate using a "partial envelope" in which the envelope parameter is set to 1.0. As shown in Fig. 32, this partial envelope provides a desirable smoothing of the terrain without overemphasizing any particular feature. Several mesoscale orographic features thought to be important to weather in the New England area are obvious in the smoothed fields of Fig. 32. These include the Adirondack mountains, the Hudson River Valley, the Green Mountains, the Berkshires, the Connecticut River Valley, the White Mountains, and the Worcester Plateau (see Fig. 33 for a map showing the locations of these features). A potential problem is that Mt. Washington falls almost directly on a grid point at the northern edge of the FGM domain and therefore tends to dominate the terrain field in northern New Hampshire. This particular point may need to be reduced in height in order to avoid numerical problems near the FGM boundary. Further processing of the terrain data includes an adjustment to the fields in the region where the CGM and FGM overlap so that coincident FGM and CGM grid points have the same elevation as described by Zhang, et al. (1986). Further, an additional smoother will be applied to the terrain field to remove any large amplitude $2\Delta x$ component which may tend to excite noise in the model.

As discussed in section 2, the model's boundary layer parameterization scheme allows for a grid box to be composed of a mixture of land and water. This



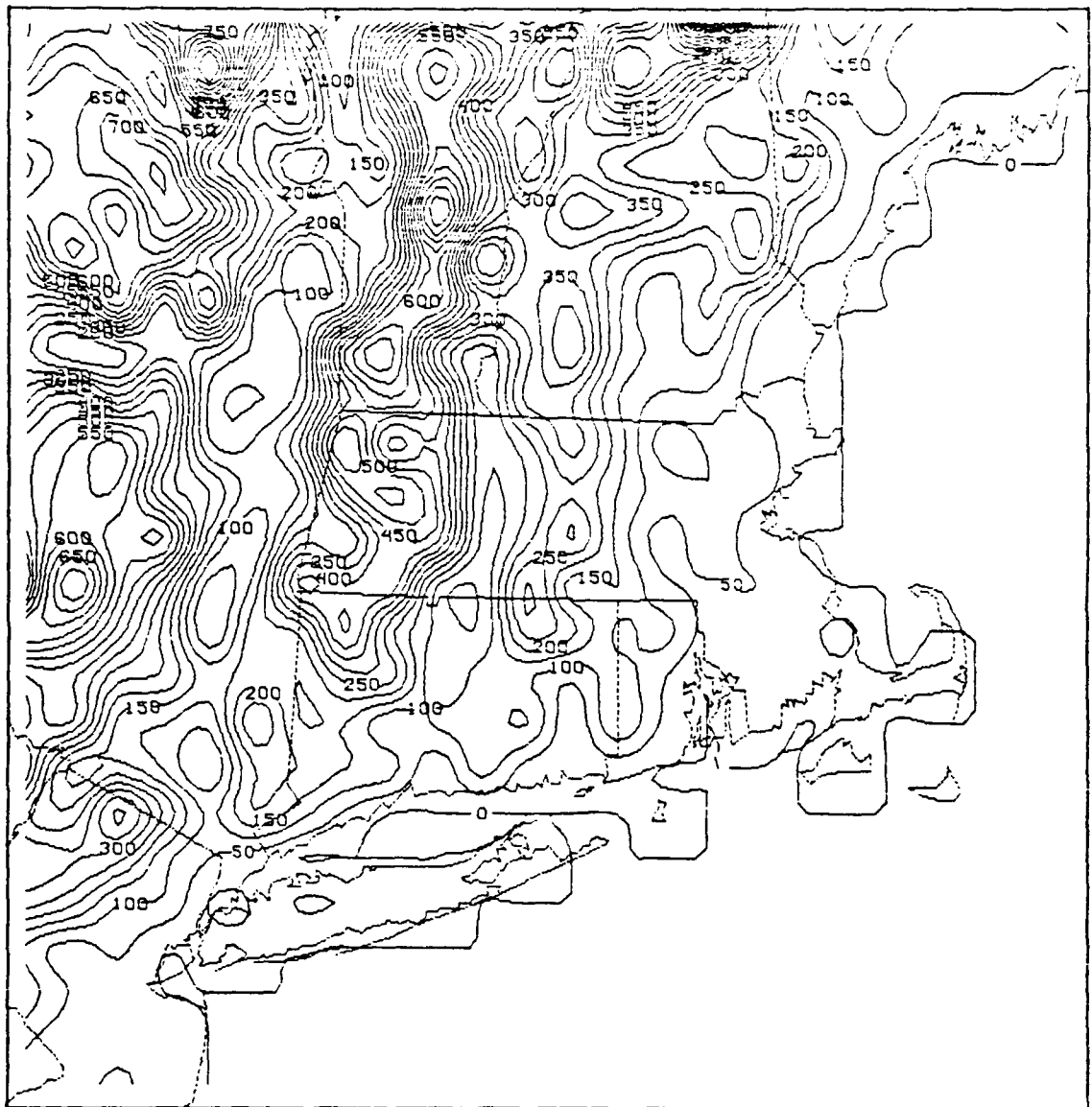
FINE GRID MESH DOMAIN

Fig. 29. FGM domain showing location of "thermodynamic" grid points.



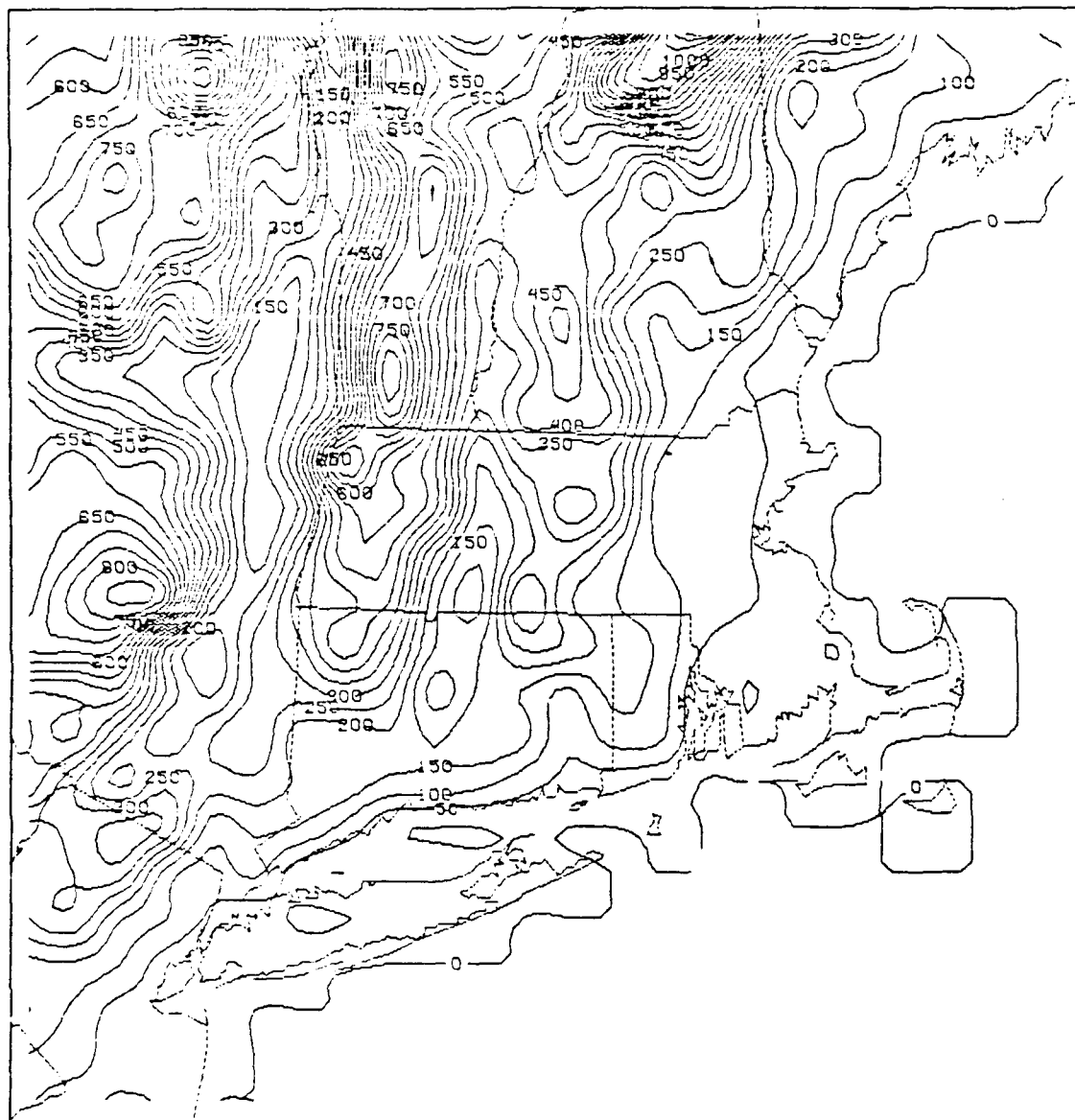
COARSE GRID MESH DOMAIN

Fig. 30. CGM domain showing location of "thermodynamic" grid points.



SURFACE ELEVATION (UNSMOOTHED) IN METERS

Fig. 31. Unsmoothed model topography for FGM domain (contour interval is 50 m).



SURFACE ELEVATION (ENVELOPE PARAMETER = 1.0) IN METERS

Fig. 32. FGM topography for a partial envelope (envelope parameter is 1.0, contour interval is 50 m).

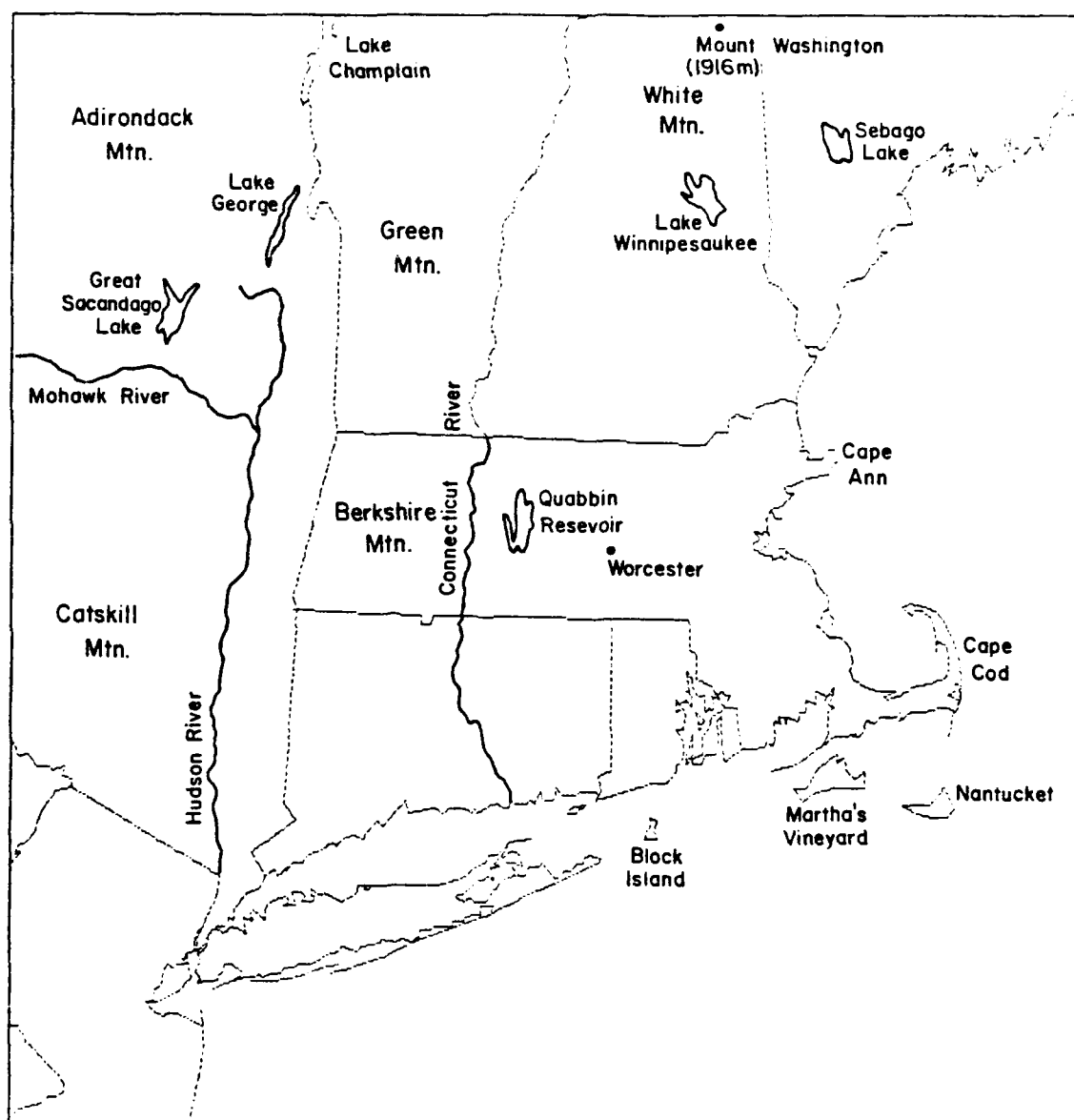


Fig. 33. Map of FGM domain showing major geographical features.

means the coastline need not be considered a "blocky" approximation to the actual coastline shown in Fig. 29, and it also means that the influence of inland bodies of water can be included in the model-derived fluxes. The U.S. Geologic Survey maps were again used to make a careful subjective estimate of the percent of water coverage for each grid box, centered on the thermodynamic grid points shown in Fig. 29. A contour plot of percent water coverage for the FGM domain is shown in Fig. 34. Notice how well even subtle variations in the coastline are captured in the contouring, and the influence of some important inland bodies of water, such as the Hudson River, the Quabbin Reservoir, and Lake Winnepesaukee (see Fig. 33). The island of Nantucket presented a problem in this analysis. Review of Fig. 29 shows that Nantucket lies nearly in the middle of a square formed by four grid points. This means that its land is almost equally divided between the four grid boxes represented by those four grid points. Rather than have the model perceive a 40×40 km area of partial land coverage, the decision was made to "move" Nantucket approximately 10 km northwest so that its land mass fell entirely within one grid box. This move is obvious in Fig. 34, in which the partial land contour representing Nantucket is displaced northwestward of the geographic location of the island.

5. Comparison of the boundary-layer parameterizations with the O'Neill dataset

A series of comparison runs have been made with the parameterizations being run in a one-dimensional form. For this report, we shall show comparisons with data taken during the O'Neill boundary layer experiment in Kansas (Lettau and Davidson 1957).

Figure 35 shows the comparison graphs for the various fluxes. In the top panel, the net radiation (NR) and soil heat flux (GS) are shown. The current model results are represented by the small circles connected with solid lines. The squares connected with dashed lines are model results from Colby (1983), which are shown for comparison because the current model was adapted from these previous parameterizations. The data from the O'Neill experiment appears as crosses with no lines connecting them. The results for NR compare very well with both the previous modeling results and the observations. The current model underforecasts

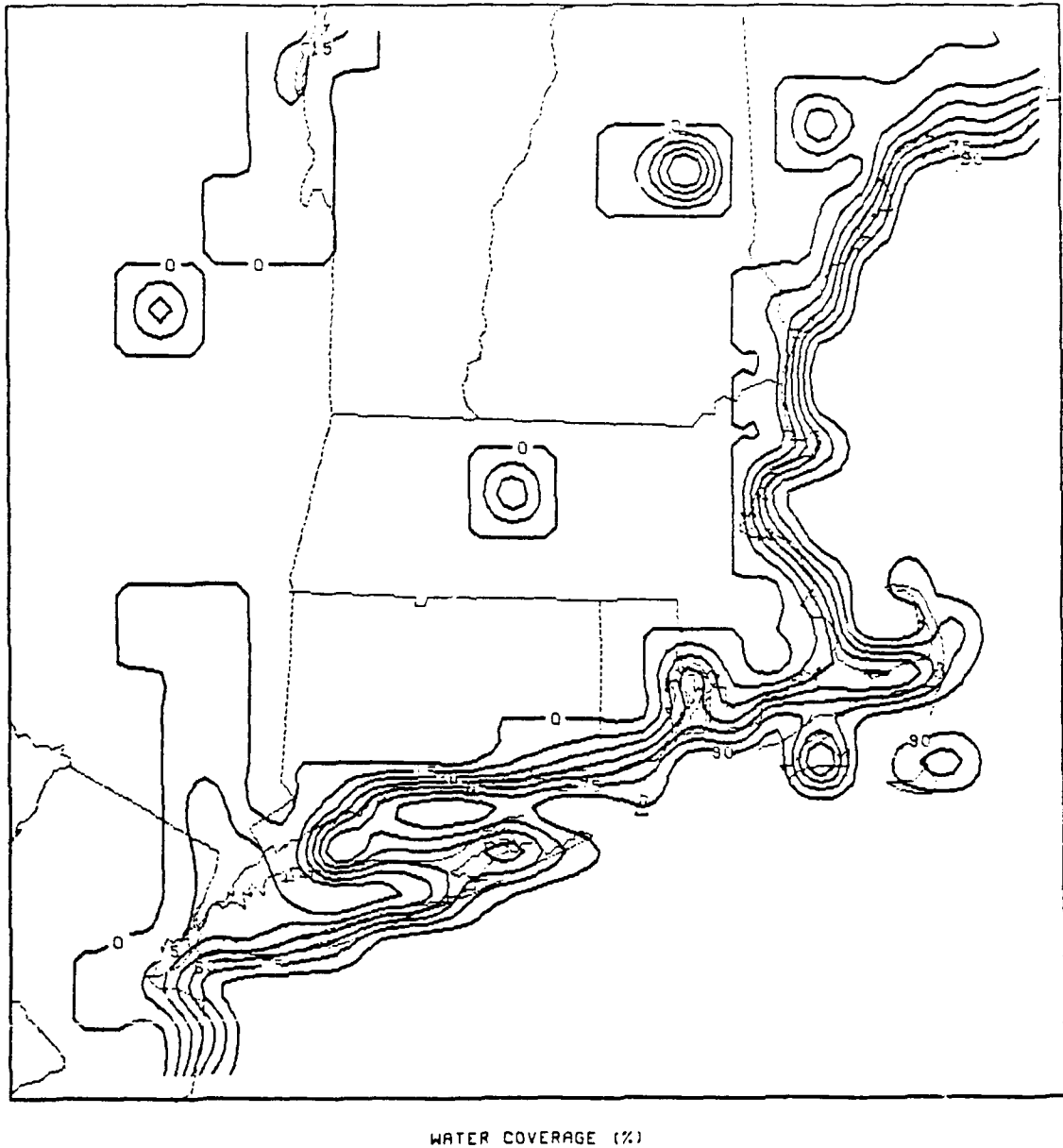
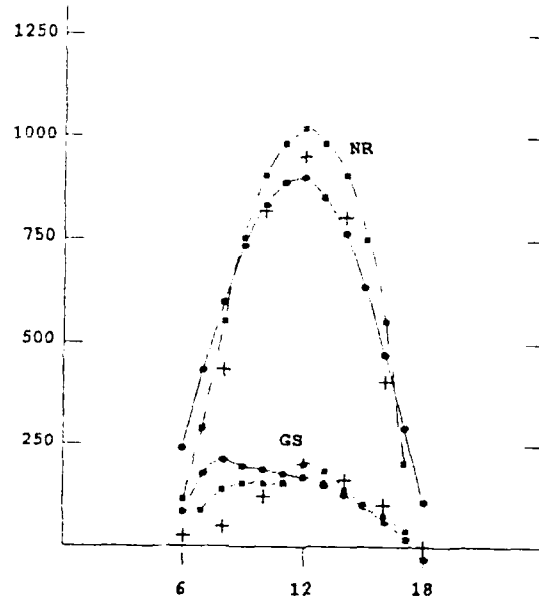


Fig. 34. Contour plot of FGM domain showing the percentage of water in each grid box (contour interval is 15%)

NET RADIATION (NR) AND
SOIL HEAT FLUX (GS)

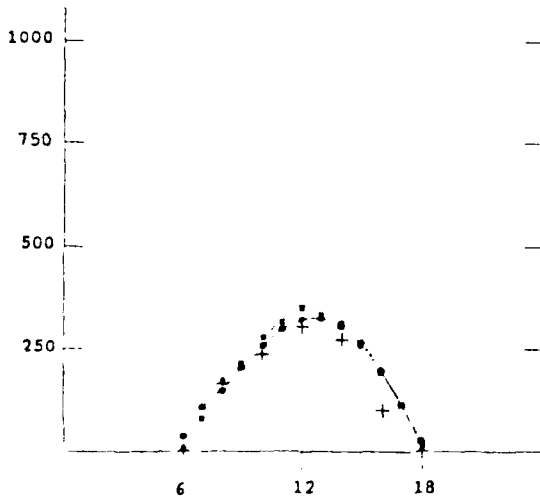
FLUX
MCAL/MIN/SQCM



TIME (LST)

SENSIBLE HEAT FLUX

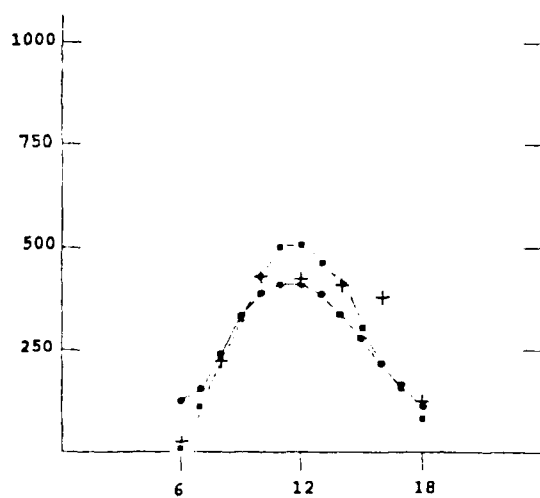
FLUX
MCAL/MIN/SQCM



TIME (LST)

LATENT HEAT FLUX

FLUX
MCAL/MIN/SQCM



TIME (LST)

Fig. 35. Various fluxes for O'Neill case data from the one-dimensional version of the boundary-layer parameterization (solid line connecting dots), previous model (dashed line connecting squares), and observations (crosses).

the peak NR by about 5%, compared to an apparent overforecast of about 10% by the previous model formulation.

The sensible and latent heat fluxes (SH, LH) are also shown in Fig. 35. It is obvious that the flux parameterization is successful in reproducing the observed values within 10% of the actual measurements. Although there appears to be a large difference between model and observations for the latent heat flux, the observations are subject to large measurement errors. The magnitude of these errors is $\pm 50 \text{ mcal min}^{-1}$; clearly both models reproduce the observations within the expected error.

The soil heat flux (GS) is not forecast well by either model in the early morning, with the current model overforecasting more than the previous model. Both models rapidly converge with the measurements, however, between 0900 and 1000 LST. After this, both models coincide with the measurements. The early morning overforecast of GS is probably responsible for the subsequent forecast errors in ground temperature (TG) evident in Fig. 36. It is apparent in this figure that the ground temperature is predicted to be too high by about 1 K during the early morning. Later, this error reverses sign when the measured ground temperature exceeds the forecasts of both models. The current model is especially low, by about 3.5 K near 1200 LST. The exact reason for this model discrepancy, particularly the difference between models, is not known. We plan to investigate this further.

Figure 36 illustrates the rise of the inversion during the day, showing the height of the top of the boundary layer in meters. The current model seems to force a too-rapid growth of the boundary layer, being at times almost 250 m higher than observed. This graph clearly demonstrates the limitation imposed by the limited vertical resolution of the model. In the real atmosphere, as well as the previous model, the initial boundary layer growth was suppressed by a very strong stable layer. Once this layer was eroded, the atmosphere above was only marginally stable, allowing rapid growth — as shown by the previous model results between 1400 and 1700 LST. In the current model, this two-layer stability is averaged into one stable layer, allowing too-rapid growth in the morning and too-slow growth in the afternoon. After 1700 LST, the distinction between the boundary layer and the layer immediately above disappeared. In the real atmosphere, the boundary layer

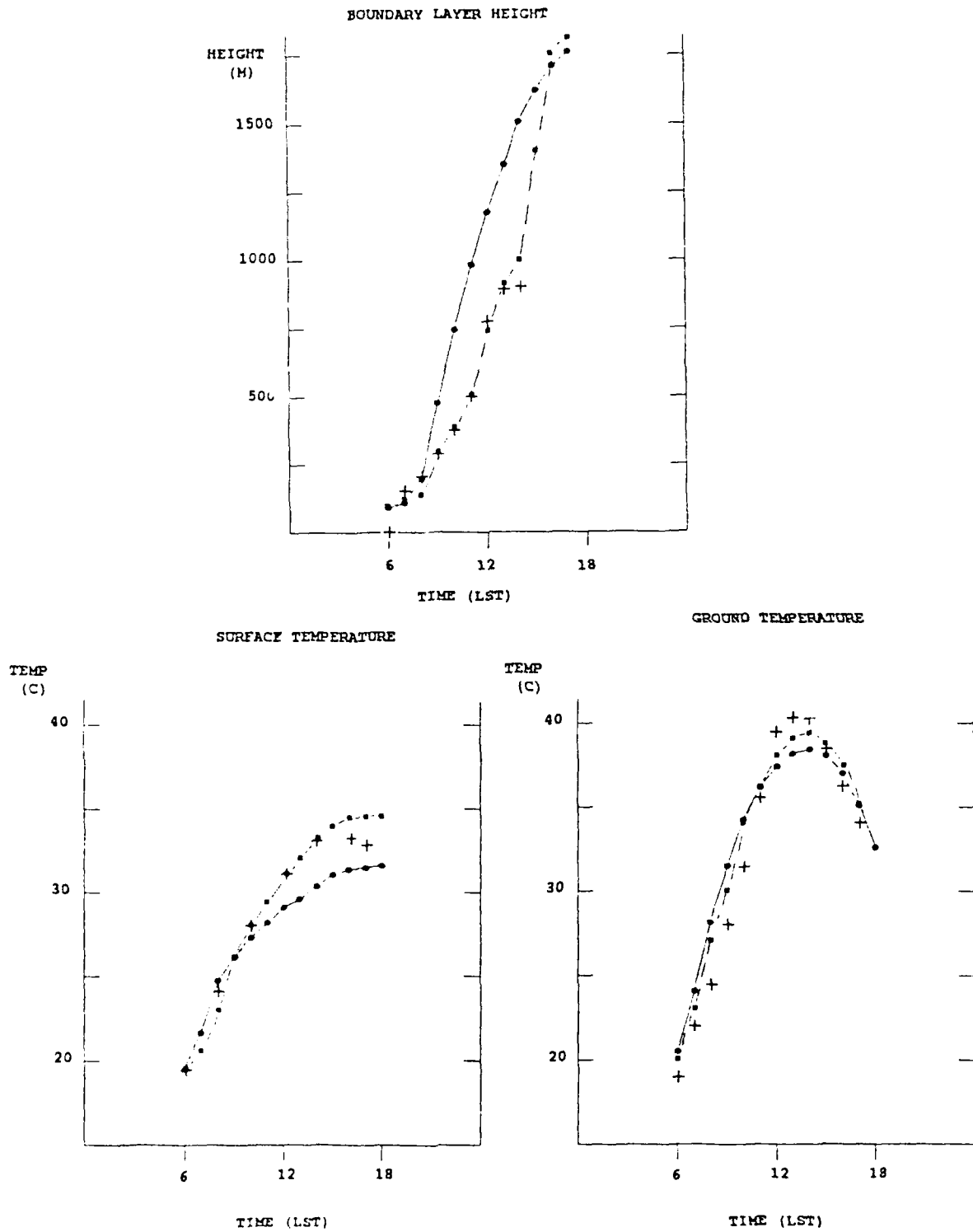


Fig. 36. As in Fig. 35, except for height of inversion, ground temperature, and "surface" temperature.

grew rapidly into the layer above, which is what both the previous and the current models demonstrate.

We believe that the growth problem and the ground temperature problem come together in the forecast of the surface temperature (TS) shown in Fig. 36. The error between the current model and the observations is nearly 4 K at its worst. We plan further comparison runs to determine whether this magnitude of error will be a common occurrence.

6. Conclusions and future work

The work outlined here demonstrates that the η -coordinate model we have developed is robust and can model the real atmosphere reasonably well despite having a very limited vertical resolution. In addition, the boundary-layer parameterizations work quickly and well, forecasting the gross characteristics of both stable and unstable boundary layers with good accuracy.

The next tasks which will be undertaken are (1) the inclusion of the boundary-layer parameterizations into the η -coordinate model, and (2) the testing of the model in both idealized and real-world situations. Inclusion of the boundary-layer code is somewhat tricky since some of the calculations must be performed in separated subroutines for consistency. Many of the calculations done in the one-dimensional form of the boundary-layer parameterizations will be removed (for example, the budget calculation used to find the boundary layer mixing ratio), and the output of results must be reworked to provide the correct variables to the main model.

When we are sure that the boundary-layer parameterizations are working correctly in the full model, we plan to run several tests of the model. One of the first tests will be a simple idealized sea-breeze circulation. Other tests will involve diurnal variations of flow over simplified terrain, similar to the ridge used in the lee-wave simulations. These tests will be followed by simulations involving the New England domain discussed in section 4. Concurrent with this testing phase we will be developing the moisture parameterizations allowing the production of stratiform precipitation in the model.

In an operational setting, the model would receive boundary conditions for the CGM domain from one of the National Weather Service operational models (preferably the NGM). These are easily implemented in the current formulation since the flow relaxation boundary condition used in the CGM allows direct insertion of externally specified boundary values. For the initial real data testing, we will probably use objectively analyzed observations taken during the "forecast" period to create the boundary conditions. This should allow the capabilities of the model to be demonstrated without any bias due to incorrect boundary condition forecast.

APPENDIX

Derivation and Energy Conservation of the Eta-Coordinate System

a. Derivation of the equations in η -coordinates

The most common form of terrain following coordinate is the σ -system where

$$\sigma = \frac{(p - p_t)}{\pi} \quad (\text{A.1})$$

where $\pi = (p_s - p_t)$, and p_s and p_t are the pressures at the surface and the top of the model domain, respectively. The equation set in this coordinate system may be written (Haltiner and Williams 1980)

$$\frac{d\mathbf{V}}{dt} + \nabla\phi + \sigma\alpha\nabla\pi + f\mathbf{k} \times \mathbf{V} = \mathbf{F} \quad (\text{A.2})$$

$$\frac{\partial\phi}{\partial\sigma} = -\pi\alpha \quad (\text{A.3})$$

$$\frac{\partial\pi}{\partial t} + \nabla \cdot \pi\mathbf{V} + \pi\frac{\partial\sigma}{\partial\sigma} = 0 \quad (\text{A.4})$$

$$c_p \frac{dT}{dt} - \alpha\omega = Q \quad (\text{A.5})$$

where

$$\omega = \frac{dp}{dt} = \pi\dot{\sigma} + \sigma(\partial\pi/\partial t + \mathbf{V} \cdot \nabla\pi)$$

and

$$\mathbf{V} = u\mathbf{i} + v\mathbf{j} ,$$

$$\nabla = \mathbf{i}\partial/\partial x + \mathbf{j}\partial/\partial y ,$$

$$\phi = \text{geopotential},$$

$$\alpha = \text{specific volume},$$

$$f = \text{Coriolis parameter},$$

$$\mathbf{F} = \text{friction term},$$

$$c_p = \text{specific heat of dry air at constant pressure},$$

and

$$Q = \text{heating term}.$$

In order to preserve conservative properties in the finite difference equations, we write the total derivatives in flux form, which can be obtained with the aid of the continuity equation (A.4). Equations (A.2) and (A.5) can then be written

$$\frac{\partial \pi V}{\partial t} + \frac{\partial u \pi V}{\partial x} + \frac{\partial v \pi V}{\partial y} + \frac{\partial \pi V \dot{\sigma}}{\partial \sigma} = -\pi \nabla \phi - \pi \alpha \sigma \nabla \pi - f \mathbf{k} \times \pi \mathbf{V} + \pi F \quad (\text{A.6})$$

$$\frac{\partial \pi T}{\partial t} + \frac{\partial u \pi T}{\partial x} + \frac{\partial v \pi T}{\partial y} + \frac{\partial \pi T \dot{\sigma}}{\partial \sigma} = \frac{\pi \alpha}{c_p} \omega + \frac{\pi Q}{c_p} \quad (\text{A.7})$$

The transformation to η -coordinates is carried out formally by using the definition of η

$$\eta = \frac{\sigma - \sigma_h}{H} \quad H = \begin{cases} \sigma_h & \sigma < \sigma_h \\ 1 - \sigma_h & \sigma > \sigma_h \end{cases} \quad (\text{A.8})$$

so that

$$\sigma = \eta H + \sigma_h \quad (\text{A.9})$$

and for some dependent variable A

$$\left(\frac{\partial A}{\partial \sigma} \right)_{\sigma} = \frac{1}{H} \frac{\partial A}{\partial \eta}$$

$$\left(\frac{\partial A}{\partial s} \right)_{\sigma} = \left(\frac{\partial A}{\partial s} \right)_{\eta} - \frac{1}{H} \frac{\partial A}{\partial \eta} \left(\frac{\partial \sigma}{\partial s} \right)_{\eta}$$

where $s = x, y$, or t . Then the η -coordinate set equivalent to (A.6), (A.3), (A.4), and (A.7) is

$$\frac{\partial \pi H V}{\partial t} + \frac{\partial u \pi H V}{\partial x} + \frac{\partial v \pi H V}{\partial y} + \frac{\partial \pi V H \dot{\eta}}{\partial \eta} = \quad (\text{A.10})$$

$$- \pi H \nabla \phi - \pi H \alpha \nabla \sigma \pi - f \mathbf{k} \times \pi H \mathbf{V} + \pi H F$$

$$\frac{\partial \phi}{\partial \eta} = -\pi H \alpha \quad (\text{A.11})$$

$$\frac{\partial \pi H}{\partial t} + \nabla \cdot \pi H \mathbf{V} + \pi \frac{\partial H \dot{\eta}}{\partial \eta} = 0 \quad (\text{A.12})$$

$$\frac{\partial \pi H T}{\partial t} + \frac{\partial u \pi H T}{\partial x} + \frac{\partial v \pi H T}{\partial y} + \frac{\partial \pi T H \dot{\eta}}{\partial \eta} = \frac{\pi H \alpha}{c_p} \omega + \frac{\pi H Q}{c_p} \quad (\text{A.13})$$

where now

$$\omega = \frac{dp}{dt} = \pi H \dot{\eta} + \partial(\sigma \pi) / \partial t + \mathbf{V} \cdot \nabla \sigma \pi \quad (\text{A.14})$$

Note that σ is now a dependent variable which is a function of x , y , η and t , and is given by (A.9). As can be seen by comparing (A.10)–(A.13) with (A.6), (A.3), (A.4), and (A.7), the transformation leads to the prognostic variables being weighted by πH in the η system instead of the π -weighting present in the σ system. Note also that terms that had been σ times derivatives of π become derivatives of the quantity $(\sigma \pi)$ in the η system.

b. Energy conservation in the η -system

In order to determine the correct finite differencing form that will preserve energy conservation in the finite difference equations, the energy conservation constraints of the continuous equations must first be derived. The analysis presented here closely follows that carried out by Haltiner and Williams (1980) for the σ -coordinate equations.

We begin with the η -coordinate momentum equation [equivalent to (A.2)]

$$\frac{d\mathbf{V}}{dt} + \nabla \phi + \alpha \nabla \sigma \pi + f \mathbf{k} \times \mathbf{V} = \mathbf{F} \quad (\text{A.15})$$

This is dotted with $\pi H \mathbf{V}$, and rewritten in the flux form with the aid of the continuity equation (A.12), to yield

$$\begin{aligned} \frac{\partial}{\partial t} \left(\frac{1}{2} \pi H V^2 \right) + \nabla \cdot \left(\frac{1}{2} \pi H \mathbf{V} V^2 \right) + \frac{\partial}{\partial \eta} \left(\frac{1}{2} \pi H \dot{\eta} V^2 \right) = \\ - \pi H \mathbf{V} \cdot (\pi H \nabla \phi + \alpha \nabla \sigma \pi) + \pi H \mathbf{V} \cdot \mathbf{F} \end{aligned} \quad (\text{A.16})$$

The first term on the right hand side represents the kinetic energy production by the pressure force. We expand this term as follows

$$-\pi H \mathbf{V} \cdot (\nabla \phi + \alpha \nabla \sigma \pi) = -\nabla \cdot (\pi H \mathbf{V} \phi) + \phi \nabla \cdot (\pi H \mathbf{V}) - \alpha \pi H \mathbf{V} \cdot \nabla \sigma \pi$$

The continuity equation (A.12) allows this to be rewritten

$$\begin{aligned} &= -\nabla \cdot (\pi H \mathbf{V} \phi) - \phi \left(\frac{\partial \pi H}{\partial t} + \pi \frac{\partial H \dot{\eta}}{\partial \eta} \right) - \alpha \pi H \mathbf{V} \cdot \nabla \sigma \pi \\ &= -\nabla \cdot (\pi H \mathbf{V} \phi) - \phi \frac{\partial \pi H}{\partial t} - \frac{\partial \phi \pi H \dot{\eta}}{\partial \eta} + \pi H \dot{\eta} \frac{\partial \phi}{\partial \eta} - \alpha \pi H \mathbf{V} \cdot \nabla \sigma \pi \end{aligned}$$

Use of the hydrostatic equation (A.11) leads to

$$= -\nabla \cdot (\pi H \mathbf{V} \phi) - \phi \frac{\partial \pi H}{\partial t} - \frac{\partial \phi \pi H \dot{\eta}}{\partial \eta} + \pi H \dot{\eta} (-H \pi \alpha) - \alpha \pi H \mathbf{V} \cdot \nabla \sigma \pi$$

Adding and subtracting $\pi H \alpha (\partial \sigma \pi / \partial t)$, and rearranging yields

$$\begin{aligned} -\pi H \mathbf{V} \cdot (\nabla \phi + \alpha \nabla \sigma \pi) &= -\nabla \cdot (\pi H \mathbf{V} \phi) - \phi \frac{\partial \pi H}{\partial t} - \frac{\partial \phi \pi H \dot{\eta}}{\partial \eta} + \pi H \alpha \frac{\partial \sigma \pi}{\partial t} \\ &\quad - H \pi \alpha \left(\frac{\partial \sigma \pi}{\partial t} + \mathbf{V} \cdot \nabla \sigma \pi + \pi H \dot{\eta} \right) \end{aligned}$$

Then using the definition of ω , (A.14), and expanding the time derivatives of the products leads to

$$\begin{aligned} &= -\nabla \cdot (\pi H \mathbf{V} \phi) - \frac{\partial \phi \pi H \dot{\eta}}{\partial \eta} - (H \phi - H \pi \alpha \sigma) \frac{\partial \pi}{\partial t} - \phi \pi \frac{\partial H}{\partial t} + \pi^2 H \alpha \frac{\partial \sigma}{\partial t} \\ &\quad - \pi H \alpha \omega \end{aligned}$$

Now, (A.11) can be rewritten as $\partial(\phi \sigma) / \partial \eta = -H(\pi \sigma \alpha - \phi)$, and this along with use of (A.11) directly leads to

$$= -\nabla \cdot (\pi H \mathbf{V} \phi) - \frac{\partial \phi \pi H \dot{\eta}}{\partial \eta} - \frac{\partial \phi \sigma}{\partial \eta} \frac{\partial \pi}{\partial t} - \phi \pi \frac{\partial H}{\partial t} - \pi \frac{\partial \phi}{\partial \eta} \frac{\partial \sigma}{\partial t} - \pi H \alpha \omega$$

Noting that π is not a function of η and that $\partial(\partial \sigma / \partial t) / \partial \eta = \partial H / \partial t$ leads to the result that

$$\begin{aligned}
 -\pi H \mathbf{V} \cdot (\nabla \phi + \alpha \nabla \sigma \pi) &= -\nabla \cdot (\pi H \mathbf{V} \phi) - \frac{\partial}{\partial \eta} \left(\phi \pi H \dot{\eta} + \phi \sigma \frac{\partial \pi}{\partial t} \right) \\
 &\quad - \frac{\partial}{\partial \eta} \left(\phi \pi \frac{\partial \sigma}{\partial t} \right) - \pi H \alpha \omega
 \end{aligned} \tag{A.17}$$

We form the total energy equation by using (A.16) with the substitution given by (A.17), and adding it to the thermodynamic equation (A.13) which can be written in the form

$$\frac{\partial}{\partial t} (\pi H c_p T) + \nabla \cdot (\pi H \mathbf{V} c_p T) + \frac{\partial}{\partial \eta} (\pi H c_p T H \dot{\eta}) = \pi H (\alpha \omega + Q) \tag{A.18}$$

to yield

$$\begin{aligned}
 &\frac{\partial}{\partial t} \left[\frac{1}{2} \pi H V^2 + \pi H c_p T \right] + \nabla \cdot \mathbf{V} \left[\frac{1}{2} \pi H V^2 + \pi H c_p T + \pi H \phi \right] \\
 &\quad + \frac{\partial}{\partial \eta} \left[\frac{1}{2} \pi V^2 H \dot{\eta} + \pi c_p T H \dot{\eta} + \pi \phi H \dot{\eta} \right] + \frac{\partial}{\partial \eta} \left(\phi \sigma \frac{\partial \pi}{\partial t} \right) + \frac{\partial}{\partial \eta} \left(\phi \pi \frac{\partial \sigma}{\partial t} \right) \\
 &= \pi H (Q + \mathbf{V} \cdot \mathbf{F})
 \end{aligned} \tag{A.19}$$

If (A.19) is integrated from $\eta = -1$ (where $\sigma = 0$) to $\eta = 1$ (where $\sigma = 1$), we obtain

$$\begin{aligned}
 &\frac{\partial}{\partial t} \left[\phi_s p_s + \int_{-1}^1 \pi H \left(\frac{1}{2} V^2 + c_p T \right) d\eta \right] + \nabla \cdot \int_{-1}^1 \pi H \mathbf{V} \left(\frac{1}{2} V^2 + c_p T + \phi \right) d\eta \\
 &= \int_{-1}^1 \pi H (Q + \mathbf{V} \cdot \mathbf{F}) d\eta
 \end{aligned} \tag{A.20}$$

where we have used $H \dot{\eta} = 0$ at $\eta = -1$ and 1 , $\partial \sigma / \partial t = 0$ at $\eta = -1$ and 1 , and $\phi (\partial \pi / \partial t) = \partial (\phi_s p_s) / \partial t$. This is precisely the same energy relation derived by Haltiner and Williams [1980, their Eq. (7-42)] for the σ -coordinate equations, if we note that $H d\eta = d\sigma$. It is desirable for this energy constraint on the continuous equations to also hold for the finite difference equations. As will be seen, this will determine the appropriate form for the finite difference equation set, and for the method of vertical finite differencing.

c. The energy-conserving finite difference equations

The finite difference form of (A.10) is

$$\begin{aligned} \frac{\partial}{\partial t}(\pi H V_k) + \frac{\partial}{\partial x}(u_k \pi H V_k) + \frac{\partial}{\partial y}(v_k \pi H V_k) + \\ \frac{\pi}{\Delta \eta} [(H \dot{\eta})_{k+1/2} \hat{V}_{k+1/2} - (H \dot{\eta})_{k-1/2} \hat{V}_{k-1/2}] = \\ - \pi H [\nabla \phi_k + \alpha_k \nabla \sigma_k \pi] - f \mathbf{k} \times \pi H \mathbf{V}_k + \pi H F_k \end{aligned} \quad (\text{A.21})$$

where H takes on the appropriate value as given by (A.8) depending on whether the layer k is above or below σ_n . The indices $(k-1/2)$ and $(k+1/2)$ refer to the layer interfaces bounding layer k above and below, respectively. The quantity \hat{V} is the interpolation of V from adjacent layers to the interface. Haltiner and Williams (1980) show that the advective terms will conserve both V and $(V \cdot V)/2$ if

$$\hat{V}_{k+1/2} = \frac{1}{2}(V_{k+1} + V_k) \quad (\text{A.22})$$

We wish to insure energy conservation of the rhs as well. The Coriolis terms do not contribute, and we will ignore the friction term and concentrate on the pressure gradient term. As with the continuous equations, we find the rate of working by the pressure gradient terms by taking $V_k \cdot$ of the first term on the rhs of (A.21) to obtain

$$\begin{aligned} -\pi H V_k \cdot [\nabla \phi_k + \alpha_k \nabla \sigma_k \pi] &= -\nabla \cdot (\pi H V_k \phi_k) + \phi_k \nabla \cdot (\pi H V_k) \\ &\quad - \alpha_k \pi H V_k \cdot \nabla \sigma_k \pi \end{aligned} \quad (\text{A.23})$$

The finite difference form of the continuity equation is

$$\frac{\partial \pi H}{\partial t} + \nabla \cdot \pi H \mathbf{V}_k + \frac{\pi}{\Delta \eta} [(H \dot{\eta})_{k+1/2} - (H \dot{\eta})_{k-1/2}] = 0 \quad (\text{A.24})$$

so, (A.23) can be rewritten

$$\begin{aligned} -\pi H \mathbf{V}_k \cdot [\nabla \phi_k + \alpha_k \nabla \sigma_k \pi] &= -\nabla \cdot (\pi H \mathbf{V}_k \phi_k) \\ &- \phi_k \left\{ \frac{\partial \pi H}{\partial t} + \frac{\pi}{\Delta \eta} [(H\dot{\eta})_{k+1/2} - (H\dot{\eta})_{k-1/2}] \right\} - \alpha_k \pi H \mathbf{V}_k \cdot \nabla \sigma_k \pi \end{aligned}$$

Adding and subtracting $\frac{\pi}{\Delta \eta} [(H\dot{\eta})_{k+1/2} \hat{\phi}_{k+1/2} - (H\dot{\eta})_{k-1/2} \hat{\phi}_{k-1/2}]$ yields

$$\begin{aligned} &= -\nabla \cdot (\pi H \mathbf{V}_k \phi_k) - \phi_k \frac{\partial \pi H}{\partial t} - \frac{\pi}{\Delta \eta} [(H\dot{\eta})_{k+1/2} \hat{\phi}_{k+1/2} - (H\dot{\eta})_{k-1/2} \hat{\phi}_{k-1/2}] \\ &+ \frac{\pi}{\Delta \eta} [(H\dot{\eta})_{k+1/2} (\hat{\phi}_{k+1/2} - \phi_k) - (H\dot{\eta})_{k-1/2} (\hat{\phi}_{k-1/2} - \phi_k)] \\ &- \alpha_k \pi H \mathbf{V}_k \cdot \nabla \sigma_k \pi \end{aligned}$$

Now, adding and subtracting $H\pi\alpha_k(\partial\sigma_k\pi/\partial t)$ leads to

$$\begin{aligned} -\pi H \mathbf{V}_k \cdot [\nabla \phi_k + \alpha_k \nabla \sigma_k \pi] &= -\nabla \cdot (\pi H \mathbf{V}_k \phi_k) \\ &- \frac{\pi}{\Delta \eta} [(H\dot{\eta})_{k+1/2} \hat{\phi}_{k+1/2} - (H\dot{\eta})_{k-1/2} \hat{\phi}_{k-1/2}] \\ &- (\phi_k H - H\pi\alpha_k\sigma_k) \frac{\partial \pi}{\partial t} - \phi_k \pi \frac{\partial H}{\partial t} + H\pi^2\alpha_k \frac{\partial \sigma_k}{\partial t} \\ &- \alpha_k \pi H \left[\frac{\partial \sigma_k \pi}{\partial t} + \mathbf{V}_k \cdot \nabla \sigma_k \pi \right] \\ &+ \frac{\pi}{\Delta \eta} [(H\dot{\eta})_{k+1/2} (\hat{\phi}_{k+1/2} - \phi_k) - (H\dot{\eta})_{k-1/2} (\hat{\phi}_{k-1/2} - \phi_k)] \end{aligned} \tag{A.25}$$

Now, it is easy to verify that

$$\frac{\partial \sigma_k}{\partial t} = \frac{\sigma_k}{H} \frac{\partial H}{\partial t} \tag{A.26}$$

So, (A.25) can be written

$$\begin{aligned}
 -\pi H \mathbf{V}_k \cdot [\nabla \phi_k + \alpha_k \nabla \sigma_k \pi] &= -\nabla \cdot (\pi H \mathbf{V}_k \phi_k) \\
 &= -\frac{\pi}{\Delta \eta} [(H\dot{\eta})_{k+1/2} \hat{\phi}_{k+1/2} - (H\dot{\eta})_{k-1/2} \hat{\phi}_{k-1/2}] \\
 &= -[\phi_k H - H \pi \alpha_k \sigma_k] \frac{\partial \pi}{\partial t} - \frac{\pi}{H} [\phi_k H - H \pi \alpha_k \sigma_k] \frac{\partial H}{\partial t} \\
 &= -\alpha_k \pi H \left[\frac{\partial \sigma_k \pi}{\partial t} + \mathbf{V}_k \cdot \nabla \sigma_k \pi \right] \\
 &+ \frac{\pi}{\Delta \eta} [(H\dot{\eta})_{k+1/2} (\hat{\phi}_{k+1/2} - \phi_k) - (H\dot{\eta})_{k-1/2} (\hat{\phi}_{k-1/2} - \phi_k)]
 \end{aligned} \tag{A.27}$$

But, using the finite difference form of $\partial(\phi\sigma)/\partial\eta = -H(\pi\sigma\alpha - \phi)$, and noting that $\partial\pi/\partial t$ and $\partial H/\partial t$ are not functions of η , we can write

$$\begin{aligned}
 -\pi H \mathbf{V}_k \cdot [\nabla \phi_k + \alpha_k \nabla \sigma_k \pi] &= -\nabla \cdot (\pi H \mathbf{V}_k \phi_k) \\
 &= -\frac{\pi}{\Delta \eta} [(H\dot{\eta})_{k+1/2} \hat{\phi}_{k+1/2} - (H\dot{\eta})_{k-1/2} \hat{\phi}_{k-1/2}] \\
 &= -\frac{1}{\Delta \eta} \left[\hat{\sigma}_{k+1/2} \hat{\phi}_{k+1/2} \frac{\partial \pi}{\partial t} - \hat{\sigma}_{k-1/2} \hat{\phi}_{k-1/2} \frac{\partial \pi}{\partial t} \right] \\
 &= -\frac{1}{\Delta \eta} \left[\hat{\phi}_{k+1/2} \pi \frac{\hat{\sigma}_{k+1/2} \partial H}{H \partial t} - \hat{\phi}_{k-1/2} \pi \frac{\hat{\sigma}_{k-1/2} \partial H}{H \partial t} \right] \\
 &= -\alpha_k \pi H \left[\frac{\partial \sigma_k \pi}{\partial t} + \mathbf{V}_k \cdot \nabla \sigma_k \pi \right] \\
 &+ \frac{\pi}{\Delta \eta} [(H\dot{\eta})_{k+1/2} (\hat{\phi}_{k+1/2} - \phi_k) - (H\dot{\eta})_{k-1/2} (\hat{\phi}_{k-1/2} - \phi_k)]
 \end{aligned} \tag{A.28}$$

Using (A.26) again leads to our final result

$$\begin{aligned}
 -\pi H \mathbf{V}_k \cdot [\nabla \phi_k - \alpha_k \nabla \sigma_k \pi] &= -\nabla \cdot (\pi H \mathbf{V}_k \phi_k) \\
 &- \frac{\pi}{\Delta \eta} [(H\dot{\eta})_{k+1/2} \hat{\phi}_{k+1/2} - (H\dot{\eta})_{k-1/2} \hat{\phi}_{k-1/2}] \\
 &- \frac{1}{\Delta \eta} \left[\hat{\sigma}_{k+1/2} \hat{\phi}_{k+1/2} \frac{\partial \pi}{\partial t} - \hat{\sigma}_{k-1/2} \hat{\phi}_{k-1/2} \frac{\partial \pi}{\partial t} \right] \\
 &- \frac{1}{\Delta \eta} \left[\hat{\phi}_{k+1/2} \pi \frac{\partial \hat{\sigma}_{k+1/2}}{\partial t} - \hat{\phi}_{k-1/2} \pi \frac{\partial \hat{\sigma}_{k-1/2}}{\partial t} \right] \\
 &- \alpha_k \pi H \left[\frac{\partial \sigma_k \pi}{\partial t} + \mathbf{V}_k \cdot \nabla \sigma_k \pi \right] \\
 &+ \frac{\pi}{\Delta \eta} [(H\dot{\eta})_{k+1/2} (\hat{\phi}_{k+1/2} - \phi_k) - (H\dot{\eta})_{k-1/2} (\hat{\phi}_{k-1/2} - \phi_k)]
 \end{aligned} \tag{A.29}$$

On term by term comparison with (A.17), it is clear that (A.29) will match the continuous equations, and conserve energy in the same way on summation over all layers, if we specify that ω is defined by

$$\begin{aligned}
 \pi H \alpha_k \omega_k &= \alpha_k \pi H \left[\frac{\partial \sigma_k \pi}{\partial t} + \mathbf{V}_k \cdot \nabla \sigma_k \pi \right] \\
 &+ \frac{\pi}{\Delta \eta} [(H\dot{\eta})_{k+1/2} (\hat{\phi}_{k+1/2} - \phi_k) - (H\dot{\eta})_{k-1/2} (\hat{\phi}_{k-1/2} - \phi_k)]
 \end{aligned} \tag{A.30}$$

This definition of ω is precisely what is needed to specify the finite difference form of the thermodynamic and hydrostatic equations, which we will derive next.

In order to show the constraints placed on the finite difference form of the thermodynamic equation, we need to first show two alternative finite difference forms of the total derivative. For a variable A at level k , we can write the total derivative in "flux form" as

$$\begin{aligned}
 \pi H \frac{dA_k}{dt} &= \frac{\partial \pi H A_k}{\partial t} + \mathbf{V}_k \cdot \nabla \pi H A_k \\
 &+ \frac{\pi}{\Delta \eta} [(H\dot{\eta})_{k+1/2} \hat{A}_{k+1/2} - (H\dot{\eta})_{k-1/2} \hat{A}_{k-1/2}]
 \end{aligned} \tag{A.31}$$

But use of the continuity equation (A.24) allows this to be rewritten in an "advective form" consistent with the flux form as

$$\pi H \frac{dA_k}{dt} = \pi H \left[\frac{\partial A_k}{\partial t} + \mathbf{V}_k \cdot \nabla A_k \right] + \frac{\pi}{\Delta \eta} \left[(H\dot{\eta})_{k+1/2} (\hat{A}_{k+1/2} - A_k) - (H\dot{\eta})_{k-1/2} (\hat{A}_{k-1/2} - A_k) \right] \quad (\text{A.32})$$

For frictionless, adiabatic motion, the potential temperature is conserved, so $d\theta/dt = 0$. The finite difference version of this in flux form is

$$\frac{\partial \pi H \theta_k}{\partial t} + \nabla \cdot \pi H \mathbf{V}_k \theta_k + \frac{\pi}{\Delta \eta} \left[(H\dot{\eta})_{k+1/2} \hat{\theta}_{k+1/2} - (H\dot{\eta})_{k-1/2} \hat{\theta}_{k-1/2} \right] = 0 \quad (\text{A.33})$$

In order to have θ and θ^2 conserved (Haltiner and Williams, 1980), we define

$$\hat{\theta}_{k+1/2} = \frac{1}{2}(\theta_k + \theta_{k+1}) \quad (\text{A.34})$$

We take the potential temperature to be defined by

$$\theta_k \equiv T_k / P_k \quad (\text{A.35})$$

and

$$P_k = \left[\frac{1}{2}(p_{k-1/2} + p_{k+1/2})^{1/2} / 1000 \right] \kappa \quad (\text{A.36})$$

The conservation of θ can be written in advective form, (A.32), as

$$\pi H \left[\frac{\partial \theta_k}{\partial t} + \mathbf{V}_k \cdot \nabla \theta_k \right] + \frac{\pi}{\Delta \eta} \left[(H\dot{\eta})_{k+1/2} (\hat{\theta}_{k+1/2} - \theta_k) + (H\dot{\eta})_{k-1/2} (\theta_k - \hat{\theta}_{k-1/2}) \right] = 0$$

Substituting the definition of θ_k , (A.35), this may be rewritten

$$\pi H \left[\frac{\partial}{\partial t} + \mathbf{V}_k \cdot \nabla \right] T_k + \pi H \frac{T_k}{P_k} \frac{\partial P_k}{\partial \sigma_k \pi} \left[\frac{\partial}{\partial t} + \mathbf{V}_k \cdot \nabla \right] \sigma_k \pi + \frac{\pi}{\Delta \eta} \left[(H\dot{\eta})_{k+1/2} (P_k \hat{\theta}_{k+1/2} - T_k) + (H\dot{\eta})_{k-1/2} (T_k - P_k \hat{\theta}_{k-1/2}) \right] = 0 \quad (\text{A.37})$$

where we have made use of the fact that P_k can be considered a function of σ and π . We now add T_k times the continuity equation, (A.24), so that the first term can be rewritten in flux form, add the finite difference form of $\pi \partial T / \partial \eta$ to both sides,

and multiply the whole equation by c_p to obtain

$$\begin{aligned} & \frac{\partial}{\partial t}(c_p \pi H T_k) + \nabla \cdot (c_p \pi H T_k \mathbf{V}_k) + \frac{c_p \pi}{\Delta \eta} [(H \dot{\eta})_{k+1/2} \hat{T}_{k+1/2} + (H \dot{\eta})_{k-1/2} \hat{T}_{k-1/2}] \\ & = \pi H \frac{c_p T_k}{P_k} \frac{\partial P_k}{\partial \sigma_k \pi} \left[\frac{\partial}{\partial t} + \mathbf{V}_k \cdot \nabla \right] \sigma_k \pi \\ & + \frac{c_p \pi}{\Delta \eta} [(H \dot{\eta})_{k+1/2} (\hat{T}_{k+1/2} - P_k \hat{\theta}_{k+1/2}) + (H \dot{\eta})_{k-1/2} (P_k \hat{\theta}_{k-1/2} - \hat{T}_{k-1/2})] \end{aligned} \quad (\text{A.38})$$

The lhs of (A.38) is the finite difference form of the lhs of (A.18), and therefore, the rhs should be equal to $\pi H \alpha \omega$ (since we are assuming $Q = 0$ here). Comparison with (A.37) shows that the first terms will be equal if

$$\alpha_k = \frac{c_p T_k}{P_k} \frac{\partial P_k}{\partial \sigma_k \pi} \quad (\text{A.39})$$

Equating the other terms leads to the following relations

$$\begin{aligned} c_p (\hat{T}_{k+1} - P_k \hat{\theta}_{k+1}) &= \phi_k - \hat{\phi}_{k+1} \\ c_p (P_k \hat{\theta}_{k-1} - \hat{T}_{k-1}) &= \hat{\phi}_{k-1} - \phi_k \end{aligned} \quad (\text{A.40})$$

When (A.35) is used in these, they can be rewritten

$$\begin{aligned} (c_p \hat{T}_{k+1/2} + \hat{\phi}_{k+1/2}) - (c_p T_k + \phi_k) &= P_k c_p (\hat{\theta}_{k+1/2} - \theta_k) \\ (c_p T_k + \phi_k) - (c_p \hat{T}_{k-1/2} + \hat{\phi}_{k-1/2}) &= P_k c_p (\theta_k - \hat{\theta}_{k+1/2}) \end{aligned} \quad (\text{A.41})$$

We can replace k by $k+1$ in the second of (A.41), add it to the first, and again use (A.35) to obtain

$$\phi_{k+1} - \phi_k = -c_p (P_{k+1} - P_k) \hat{\theta}_{k+1/2} \quad (\text{A.42})$$

This represents a finite difference form of the hydrostatic equation that is consistent with the other equations, and provides a means of calculating the geopotentials at all layers once the geopotential is known at the lowest layer (where

$k = k_{bm}$). Haltiner and Williams (1980) show that it is possible to derive an integral constraint from the energy conservation which yields the geopotential of the lowest layer in terms of the geopotential differences of all the other layers. It is pointed out, however, that this accumulates the errors of the layer calculations and leads to large errors in the geopotential of the lowest layer. Experimentation with the model verified this result. We choose a simpler method of obtaining the lowest layer geopotential which, though not strictly consistent with energy conservation, yields accurate values. Since the boundary layer parameterization provides an "surface" temperature, we use this temperature to form a "half-layer" average potential temperature

$$\hat{\theta}_{k+1/2} = \frac{1}{2}(\theta_{k_{bm}} + \theta_{surf})$$

Then an equation of the form of (A.42) can be used to find $\phi_{k_{bm}}$ in terms of the geopotential at the surface.

The thermodynamic equation can now be written in the form used in the model by noting that (A.38) reduces to

$$\begin{aligned} \frac{\partial \pi H T_k}{\partial t} + \nabla \cdot \pi H \mathbf{V}_k T_k + \frac{\pi}{\Delta \eta} [(H\dot{\eta})_{k+1/2} P_k \hat{\theta}_{k+1/2} - (H\dot{\eta})_{k-1/2} P_k \hat{\theta}_{k-1/2}] \\ = \frac{\pi H \alpha_k}{c_p} \left[\frac{\partial}{\partial t} + \mathbf{V}_k \cdot \nabla \right] \sigma_k \pi + \frac{\pi}{c_p} Q_k \end{aligned} \quad (\text{A.43})$$

(where we have added the diabatic heating term). Thus, the equations (A.21), (A.42), and (A.43) form a consistent finite difference set for momentum, geopotential, and temperature which conserve total energy in the same manner as the continuous equations.

d. The complete finite difference equation set

We restate here the finite difference equations derived above and add those not yet discussed to form the complete set used in the model. The only advective quantity in the model whose finite difference form is not discussed above is the one that governs specific humidity, q . In the absence of condensation or evaporation, however, specific humidity represents a conserved quantity that satisfies $dq/dt = 0$. We write this total derivative in the flux form given by (A.31).

The complete set of finite difference equations for momentum, ϕ , T , and q is then

$$\begin{aligned} \frac{\partial}{\partial t}(\pi H V_k) + \frac{\partial}{\partial x}(u_k \pi H V_k) + \frac{\partial}{\partial y}(v_k \pi H V_k) + \\ \frac{\pi}{\Delta \eta} [(H\dot{\eta})_{k+1/2} \hat{V}_{k+1/2} - (H\dot{\eta})_{k-1/2} \hat{V}_{k-1/2}] = \\ - \pi H [\nabla \phi_k + \alpha_k \nabla \sigma_k \pi] - f \mathbf{k} \times \pi H \mathbf{V}_k + \pi H F_k \end{aligned} \quad (\text{A.21})$$

$$\phi_{k+1} - \phi_k = -c_p (P_{k+1} - P_k) \hat{\theta}_{k+1/2} \quad (\text{A.42})$$

$$\begin{aligned} \frac{\partial \pi H T_k}{\partial t} + \nabla \cdot \pi H \mathbf{V}_k T_k + \frac{\pi}{\Delta \eta} [(H\dot{\eta})_{k+1/2} P_k \hat{\theta}_{k+1/2} - (H\dot{\eta})_{k-1/2} P_k \hat{\theta}_{k-1/2}] \\ = \frac{\pi H \alpha_k}{c_p} \left[\frac{\partial}{\partial t} + \mathbf{V}_k \cdot \nabla \right] \sigma_k \pi + \frac{\pi}{c_p} Q_k + \pi H F_k \end{aligned} \quad (\text{A.43}')$$

and

$$\frac{\partial \pi H q_k}{\partial t} + \nabla \cdot \pi H \mathbf{V}_k q_k + \frac{\pi}{\Delta \eta} [(H\dot{\eta})_{k+1/2} \hat{q}_{k+1/2} - (H\dot{\eta})_{k-1/2} \hat{q}_{k-1/2}] = F_k \quad (\text{A.44})$$

where

$$\theta_k \equiv T_k / P_k \quad (\text{A.35})$$

and

$$P_k = \left[\frac{1}{2} (p_{k-1/2} + p_{k+1/2})^{1/2} / 1000 \right]^\kappa \quad (\text{A.36})$$

Note that an eddy diffusion term, F_k , is added to the rhs of (A.43') and (A.44) as described in section 2 to help control noise. The finite difference form of (2.7), which calculates the rate of change of π is written

$$\frac{\partial \pi}{\partial t} = - \sum_{k=1}^{kbm} \left[\frac{\partial}{\partial x} (H \pi u_k) + \frac{\partial}{\partial y} (H \pi v_k) \right] \quad (\text{A.45})$$

where H takes on the correct values above and below the boundary layer top as

given by (A.8). Similarly, the finite difference form of (2.8) allows calculation of $(H\dot{\eta})$ at each interface as

$$\begin{aligned} (H\dot{\eta})_{k+1/2} = & -(\eta_{k+1/2} + 1) \left[\pi \frac{\partial \sigma_h}{\partial t} + \frac{H}{\pi} \frac{\partial \pi}{\partial t} \right] \\ & - \sum_{k=1}^k \left[\frac{\partial}{\partial x} (H \pi u_k) + \frac{\partial}{\partial y} (H \pi v_k) \right] \end{aligned} \quad (\text{A.46})$$

which can be applied after (A.45) has been solved to provide $\partial \pi / \partial t$ and after the boundary layer parameterization has provided $\partial h / \partial t$ which can be converted to $\partial \sigma_h / \partial t$. The above finite difference equations are applied on the staggered grid using the averaging and differencing schemes presented by Anthes and Warner (1978).

References

- Anthes, R.A., and T.T. Warner, 1978: Development of hydrodynamic models suitable for air pollution and other mesometeorological studies. *Mon. Wea. Rev.*, 106, 1045-1078.
- Colby, F.P., Jr., 1980: The role of convective instability in an Oklahoma squall line. *J. Atmos. Sci.*, 37, 2113-2119.
- Davies, H.C., 1976: A lateral boundary condition for multi-level prediction models. *Quart. J. Roy. Meteor. Soc.*, 102, 405-418.
- Haltiner, G.J., and R.T. Williams, 1980: *Numerical Weather Prediction and Dynamic Meteorology*. J. Wiley & Sons, 477 pp.
- Kurihara, Y. and M.A. Bender, 1980: Use of a movable nested-mesh model for tracking a small vortex. *Mon. Wea. Rev.*, 99, 1792-1809.
- Lavoie, R.L., 1972: A mesoscale numerical model of lake-effect storms. *J. Atmos. Sci.*, 29, 1025-1040.
- Lettau, H., and Davidson, 1957: *Explaining the Atmosphere's First Mile*, Pergamon Press, New York, Vol. I, II.
- Nickerson, E.C., 1979: On the simulation of airflow and clouds over mountainous terrain. *Beit. Atmos. Phys.*, 52, 161-177.
- Nickerson, E.C., E. Richard, R. Rosset, and D.R. Smith, 1986: The numerical simulation of clouds, rain, and airflow over the Vosges and Black Forest mountains: A meso- β model with parameterized microphysics. *Mon. Wea. Rev.*, 114, 398-414.
- Pielke, R.A., 1984: *Mesoscale Meteorological Modeling*, Academic Press, 612 pp.
- Perkey D. J., and C.W. Kreitzberg, 1976: A time-dependent lateral boundary scheme for limited-area primitive equation models. *Mon. Wea. Rev.*, 104, 744-755.
- Seitter, K.L., 1987: The specification of lateral boundary conditions in three-dimensional mesoscale numerical models. Final Report. *AFGL-TR-87-0015*, 129 pp. ADA179185.
- Seitter, K.L., and F.P. Colby, Jr., 1989: Super-Micro Computer Weather Prediction Model. Scientific Report No. 1. *AFGL-TR-89-0239*, 37 pp. ADA216329
- Shapiro, R., 1970: Smoothing, filtering and boundary effects. *Rev. Geophys. Space Phys.*, 8, 359-387.

- Wallace, J.M., S. Tibaldi and A.J. Simmons, 1983: Reduction of systematic forecast errors in the ECMWF model through the introduction of an envelope orography. *Quart. J. Roy. Meteor. Soc.*, **109**, 683-717.
- Wetzel, P.J., 1978: A detailed parameterization of the atmospheric boundary layer. *Atmos. Sci. Paper* 302, Colorado State University.
- Zhang, D.-L., H.-R. Chang, N.L. Seaman, T.T. Warner, and J.M. Fritsch, 1986: A two-way interactive nesting procedure with variable terrain resolution. *Mon Wea. Rev.*, **114**, 1330-1339.